

Die approbierte Originalversion dieser Dissertation ist an der Hauptbibliothek der Technischen Universität Wien aufgestellt (<http://www.ub.tuwien.ac.at>).

The approved original version of this thesis is available at the main library of the Vienna University of Technology (<http://www.ub.tuwien.ac.at/englweb/>).



Diese Dissertation haben begutachtet

Prof. Dr. Ulrich Schubert

Prof. Dr. Herbert Ipser

DISSERTATION

Metal Nitride and Metal Oxide Nanocomposite Materials

ausgeführt zum Zwecke der Erlangung des akademischen Grades eines

Doktors der Naturwissenschaften unter der Leitung von

O.Univ.Prof. Dipl.-Ing. Dr.rer.nat. Ulrich Schubert

E165

Institut für Materialchemie

eingereicht an der Technischen Universität Wien

Fakultät für Technische Chemie

von

Rupali Ganpat Deshmukh

Mat. Nr. 0926130

Dirmhirngasse 27/614, 1230 Wien

Wien, am 25. Juli 2012

Acknowledgements

After three and half years of doctorate study and training, it is finally time to finish my thesis and have the chance to acknowledge and thank the people who have helped me in all kinds of ways.

First and foremost, I wish to express my heartfelt gratitude to my advisor Prof. Dr. Ulrich Schubert for his guidance and support in academia. I am very grateful to his patience and invaluable advices that inspired me to see things positively and felt honoured with his confidence and trust on my ability.

I thank Prof. Dr. Herbert Ipser for his willingness to serve as the second examiner of my thesis.

I thank Asso. Prof. Dr. Erich Halwax for numerous powder XRD measurements and analysis, Elisabeth Eitenberger for the SEM analysis, Dr. Michael Puchberger for NMR measurements, and Prof. Johannes Bernardi for his help with the TEM analysis. Thanks to Matthias Ikeda for physical measurements of samples, Prof. Peter Rogl and Dr. Andriy Grytsiv for hot pressing the samples.

I thank to Kleintl Rupert for regular mechanical repairs, Stephan Reiter for providing chemicals and materials, Schauer Harald for his help with computers, Melita Kirl and Anita Demaj for their help with administrative work.

I would like to acknowledge and thank my present and past colleagues; Christine Artner, Dr. Sven Barth (for your company on weekends and helpful suggestions), Dr. Stefan Baumann (for introducing me to Schlenk line technique), Dr. Maria Bendova, Matthias Czakler, Felix Biegger, Aparna Date, Dr. Van An Du, Stefan Edinger, Elisabeth Felbermair, Dr. Jasmin Geserick (for your help on BET measurements and analysis), Johannes Kreutzer, Martin Kronstein, Dr. Marco Litschauer (helping hands always with software's and instruments), Dr. Christoph Lomoschitz, Dr. Marina Lomoschitz, Dr. Robert Lichtenberger, Dr. Hongshi Liu, Christian Maurer (you helped me a lot in many ways.....thanks), Sarah Meyer, Dr. Marie-alexandra Neouze, Dr. Robert Potzmann, , Dr. Mohsin Raza and Dr. Jingxia Yang. Thank you all for making a pleasant working atmosphere and for helping hands all the time.

I am forever grateful to Dr. Venkat Ravi for his support and encouragement to pursue Ph.D. abroad. I thank to Dr. Sagar Beldar for supporting me at every failure and success. You always gave me new visions to think differently and to look at life very positively.

Lastly, and most importantly, I wish to thank my parents, Asha Deshmukh and Ganpat Deshmukh. They raised me, supported me, taught me, and loved me. To them I dedicate this thesis.

Zusammenfassung

In dieser Arbeit sollen unterschiedliche Routen zur Synthese von Metallnitrid-Nanopartikeln in beziehungsweise auf einer Siliziumdioxid-Matrix untersucht werden.

Im ersten Teil der Arbeit wurde die Synthese von Metallnitrid@SiO₂ und Kupfersulfid@SiO₂ - Nanokomposite über den Sol-Gel-Prozess von entsprechenden Komplexen untersucht. Bei dieser Methode wurde die Synthese der organometallischen Verbindung mit der Darstellung der Silica-Matrix über die Sol-Gel Route verbunden. Ein wichtiger Punkt dabei war die Verwendung des Liganden vom Typ (RO)₃Si-(CH₂)₃-X mit X = -NH-CH₂-CH₂-NH₂ als koordinative Gruppe. Die Gruppe X erlaubte weiters die Koordination von Metallionen zum Silica-Netzwerk während dem Sol-Gel-Prozess, sodass es zur intermediären Bildung von Komplexen des Typs (RO)₃Si(CH₂)₃-X-M gekommen ist. Dadurch konnte ein Zweikomponentensystem in einen Single-Source-Precursor transferriert werden, weshalb es zu einer guten Verteilung des Metall-Precursors während des Sol-Gel-Prozesses kommt. Die kontrollierte thermische Behandlung des getrockneten Gels führte zur Pyrolyse der organischen Komponenten bei gleichzeitiger Ausbildung von Metalloxid-Nanopartikeln in einer Silica-Matrix. Die anschließende Reaktion der Metalloxid@SiO₂ - Nanokomposite mit gasförmigem Ammoniak bei erhöhter Temperatur erlaubte die Bildung von extrem gut dispergierten Metallnitrid-Nanopartikeln in einer Silica-Matrix. Cu₃N@SiO₂, GaN@SiO₂, CrN@SiO₂, Co₂N@SiO₂ und VN@SiO₂- Nanokomposite wurden über diese Methode hergestellt. Weiters konnten CuS@SiO₂ - Nanokomposite durch die Reaktion von CuO@SiO₂ mit wässrigem Ammoniumsulfat bei Raumtemperatur hergestellt werden.

Im zweiten Teil dieser Arbeit wurden Cu₃N - Nanopartikel in mesoporösen Silica-Hohlkugeln mit Hilfe von Templaten aus Kohlenstoffkugeln hergestellt. Die Kohlenstoffkugeln sind bekannt für ihre gleichmässige Oberfläche funktionaler Schichten, welche durch Koordination beziehungsweise elektrostatischer Aufladung Metallionen binden können. Die hierbei verwendete Methode basierte auf der Adsorption von Kupferionen [Cu²⁺ und Cu(NH₃)₄(H₂O)₂²⁺] aus der Lösung an der funktionalen Oberflächen der Kohlenstoff-Kugelpackungen. Diese wurden anschliessend mit Hilfe des Sol-Gel-Prozesses von Tetraethylorthosilikat in Gegenwart von strukturdivergierender Substanzen mit einer Silica-Hülle beschichtet. Die darauffolgende Kalzinierung und Oxidation führte zu Kupferoxid-Nanopartikel in einer hohlen mesoporösen Silica-Hülle. Die Nitrierung der CuO-Nanopartikel

erlaubte die Synthese von Cu_3N -Nanopartikel in einer mesoporösen Silica-Hülle ohne dabei die Struktur der Silica-Hülle zu zerstören.

Im dritten Teil der Arbeit wurden hierarchisch strukturierte $\text{CuO}@/\text{SiO}_2$ und $\text{Cu}_3\text{N}@/\text{SiO}_2$ Hohlkugeln (HHS) aus CuSiO_3 HHSs synthetisiert. Die CuO -Nanopartikel auf SiO_2 /HHSs wurden durch thermische Behandlung von CuSiO_3 -HSSs an Luft erhalten, während die Cu_3N -Nanopartikel auf SiO_2 -HHSs durch Nitrierung hergestellt werden konnten. Diese Umwandlung von CuSiO_3 HSSs in $\text{CuO}@/\text{SiO}_2$ und $\text{Cu}_3\text{N}@/\text{SiO}_2$ HSSs ist ein vollkommen neuer Zugang.

Im letzten Teil dieser Arbeit wurden nanostrukturierte, polykristalline $(\text{SrTiO}_3)_{1-x}(\text{SrCO}_3)_x$ ($x = 0, 0.20, 0.32, 0.44$) Komposite hergestellt und auf ihre physikalischen Eigenschaften hin untersucht. Im Vergleich zu SrTiO_3 - Einkristallen wurde eine signifikant reduzierte thermische Leitfähigkeit gemessen. Der Austausch mit SrCO_3 wurde zur Verringerung des thermischen Diffusionsvermögen eingesetzt, dabei konnte jedoch keine systematische Abhängigkeit des Diffusionsvermögen vom SrCO_3 -Gehalt beobachtet werden.

Abstract

In this work different synthesis routes for the formation of metal nitride nanoparticles in/on silica are mainly investigated.

In the first part of the work the synthesis of metal nitride@SiO₂ and copper sulphide@SiO₂ nanocomposites through sol-gel processing of tethered metal complexes was investigated. In this method an organometallic approach for the synthesis of metal complexes and a sol-gel method for the formation of the silica matrix were combined. The key point of this work was the use of (RO)₃Si-(CH₂)₃-X, where X = -NH-CH₂-CH₂-NH₂ a coordinating group. The groups X allow tethering of metal ions to the silicate network during sol-gel processing due to the intermediate formation of complexes (RO)₃Si(CH₂)₃-X-M, where M is a metal ion. A two component system is transformed into a single-source precursor, resulting in a high dispersion of the metal precursor during sol-gel processing. Controlled thermal treatment to the dry gel containing tethered metal complexes leads to the degradation of the organic components and simultaneous formation of metal oxide nanoparticles in silica matrix. Subsequent reaction of the metal oxide@SiO₂ nanocomposites with gaseous ammonia at elevated temperature allowed formation of highly dispersed metal nitride nanoparticles in a SiO₂ matrix. Cu₃N@SiO₂, GaN@SiO₂, CrN@SiO₂, Co₂N@SiO₂ and VN@SiO₂ nanocomposites were synthesized by this method. Additionally the CuS@SiO₂ nanocomposite was obtained by reaction of CuO@SiO₂ with aqueous ammonium sulphide at room temperature.

In the second part, Cu₃N nanoparticles within hollow mesoporous silica spheres were synthesized by using a carbon sphere template. The carbon spheres are known to have uniform surface functional layers capable of binding metal ions through coordination or electrostatic interactions. The method involved the initial adsorption of copper ions (Cu²⁺ or [Cu(NH₃)₄(H₂O)₂]²⁺) from solution onto the functional surface layer of the carbon spheres. These are then coated by a silica shell by sol-gel processing of tetraethylorthosilicate in the presence of a surfactant. Subsequent calcination and oxidation procedures lead to copper oxide nanoparticles in hollow mesoporous silica shells. The nitridation of the CuO nanoparticles allowed preparing Cu₃N nanoparticles within the hollow mesoporous silica spheres without changing the silica shell structure.

In the next part of the work hierarchical hollow spheres (HHSs) of CuO@SiO₂ and Cu₃N@SiO₂ were synthesized from CuSiO₃ HHSs. CuO nanoparticles bestrewed on SiO₂ HHSs were obtained by heat treatment of the CuSiO₃ HHSs in air. Moreover, Cu₃N

nanoparticles attached to the SiO₂ HHSs were obtained by nitridation of CuSiO₃ HHSs. The conversion of CuSiO₃ HHSs to CuO@SiO₂ and Cu₃N@SiO₂ HHSs is a novel approach.

In the last part of the work, nanostructured polycrystalline (SrTiO₃)_{1-x}(SrCO₃)_x (x = 0, 0.20, 0.32, 0.44) composites were synthesized and measured for physical properties. In comparison to single crystalline SrTiO₃, the thermal conductivity of all composites was found to be reduced significantly. The substitution with SrCO₃ was done to lower the thermal diffusivity. A systematic dependence of the diffusivity on the SrCO₃ content could not be observed.

Parts of this work have been published

“Metal nitride@SiO₂ nanocomposites by sol-gel processing starting from tethered metal complexes”; Rupali Deshmukh and Ulrich Schubert; *Journal of Materials Chemistry*, **2011**, 21, 18534-18536.

Abbreviations

°	Degree
2θ	Diffraction angle
λ	Wavelength
a. u.	Arbitrary units
AEAPTS	N-[3-trimethoxysilyl]propyl]ethylenediamine
BET	Brunauer, Emmett and Teller
BJH	Barrett, Joyner and Halenda
CNT	Carbon nanotubes
CTAB	Cetyl trimethylammonium bromide
CVD	Chemical vapor deposition
EDX	Energy dispersive X-ray spectroscopy
K	Kelvin
MPa	Megapascal
NP	Nanoparticle
P/P ₀	Relative pressure
PVD	Physical vapor deposition
P123	Triblock copolymer Pluronic P123, HO(CH ₂ CH ₂ O) ₂₀ (CH ₂ CH(CH ₃)O) ₇₀ (CH ₂ CH ₂ O) ₂₀ H
SAED	Selected area electron diffraction
SEM	Scanning electron microscopy
TEM	Transmission electron microscopy
TEOS	Tetraethylorthosilicate
TGA	Thermogravimetric analysis
UV-Vis	Ultraviolet-visible
wt %	Weight percent
XRD	X-ray diffraction

Table of Contents

Chapter 1	1
Introduction	1
1.1 Sol-Gel Process	2
1.2 Mesoporous Silica	3
1.3 Metal Nitride Nanoparticles	4
1.4 Goal of Work.....	5
1.5 References	7
Chapter 2	10
Metal Nitride@SiO ₂ and CuS@SiO ₂ Nanocomposites by Sol-Gel Processing Starting from Tethered Metal Complexes.....	10
2.1 Metal Nitrides.....	11
2.2 Synthesis of Metal Nitrides	12
2.3 Copper Sulphide (CuS)	13
2.4 Synthesis of Metal Sulphides	14
2.5 Metal Oxide@SiO ₂ and Metal@SiO ₂ Nanocomposites.....	14
2.6 Results and Discussion.....	16
2.6.1 Cu ₃ N@SiO ₂ Nanocomposite	16
2.6.2 GaN@SiO ₂ Nanocomposite	21
2.6.3 CrN@SiO ₂ Nanocomposite.....	23
2.6.4 VN@SiO ₂ Nanocomposite	24
2.6.5 Co ₂ N@SiO ₂ Nanocomposite	26
2.6.6 MN@SiO ₂ Nanocomposites - Result Summary.....	27
2.7 CuS@SiO ₂ Nanocomposites by Sol-gel Processing Starting from Tethered Copper Complexes	28
2.7 Conclusion.....	31
2.8 References	32
Chapter 3	38
Functional Nanoparticles (CuO and Cu ₃ N) within Hollow Mesoporous Silica Capsules.....	38
3.1 Results and Discussion.....	43
3.1.1 Route 1	43
3.1.2 Route 2	49
3.1.3 Route 3	56
3.2 Conclusion.....	60
3.3 References	62

Chapter 4	66
Synthesis of CuO@SiO ₂ and Cu ₃ N@SiO ₂ Hierarchical Hollow Spheres (HHSs) via CuSiO ₃ HHSs ..	66
4.1 Results and Discussion	69
4.2 Conclusion	75
4.3 References	76
Chapter 5	79
Synthesis and Physical Properties of Strontium Titanate and Strontium Titanate/Strontium Carbonate Composites	79
5.1 Results and Discussion	82
5.1.1 SrTiO ₃ and SrTiO ₃ /SrCO ₃ Composites	82
5.1.2 SrTi _{0.8} Nb _{0.2} O ₃	87
5.1.3 Thermal Conductivity (κ) Measurements	88
5.2 Conclusion	89
5.3 References	91
Chapter 6	93
Experimental Part	93
6.1 Materials	93
6.2 Instrumentation	93
6.3 Experimental	95
6.3.1 Preparation of metal nitride@SiO ₂ and CuS@SiO ₂ nanocomposites by sol-gel processing starting from tethered metal complexes	95
6.3.1.1 Preparation of Cu ₃ N@SiO ₂	95
6.3.1.2 Preparation of GaN@SiO ₂	95
6.3.1.3 Preparation of CrN@SiO ₂	95
6.3.1.4 Preparation of VN@SiO ₂	96
6.3.1.5 Preparation of Co ₂ N@SiO ₂	96
6.3.1.6 Preparation of CuS@SiO ₂	96
6.3.2 Synthesis of functional nanoparticles (CuO and Cu ₃ N) within hollow mesoporous silica capsules – Route 1	97
6.3.2.1 Preparation of carbon spheres	97
6.3.2.2 Preparation of Cu ²⁺ ion-adsorbed carbon spheres (Cu ²⁺ /carbon sphere)	97
6.3.2.3 Preparation of CuO@H-mSiO ₂ sphere	97
6.3.2.4 Preparation of Cu ₃ N@H-mSiO ₂ spheres	98
6.3.3 Synthesis of functional nanoparticles (CuO and Cu ₃ N) within hollow mesoporous silica capsules – Route 2	98
6.3.3.1 Synthesis of colloidal carbon spheres	98
6.3.3.2 Synthesis of hollow mesoporous silica spheres (H-mSiO ₂ spheres)	98

6.3.3.3 Synthesis of CuO@H-mSiO ₂ -NC.....	98
6.3.3.4 Synthesis of Cu ₃ N@H-mSiO ₂ -NC	99
6.3.4 Synthesis of functional nanoparticles (CuO and Cu ₃ N) within hollow mesoporous silica capsules – Route 3.....	99
6.3.4.1 Preparation of carbon spheres	99
6.3.4.2 Preparation of Cu ²⁺ adsorbed carbon spheres (Cu ²⁺ /carbon sphere)	99
6.3.4.3 Preparation of CuO@H-mSiO ₂ sphere	99
6.3.4.4 Synthesis of Cu ₃ N@H-mSiO ₂ sphere.....	100
6.3.5 Synthesis of CuO@SiO ₂ and Cu ₃ N@SiO ₂ hierarchical hollow spheres (HHSs) via CuSiO ₃ HHSs	100
6.3.5.1 Synthesis of SiO ₂ spheres	100
6.3.5.2 Synthesis of CuSiO ₃ HHSs	100
6.3.5.3 Synthesis of CuO@SiO ₂ HHSs.....	101
6.3.5.4 Synthesis of Cu ₃ N@SiO ₂ HHSs	101
6.3.6 Synthesis of SrTiO ₃ , SrTiO ₃ /SrCO ₃ composites and SrTi _{0.8} Nb _{0.2} O ₃	101
6.3.6.1 Synthesis of SrTiO ₃ and SrTiO ₃ /SrCO ₃ composites	101
6.3.6.2 Synthesis of SrTi _{0.8} Nb _{0.2} O ₃	101
6.4 References	102
Chapter 7	103
Summary and Outlook.....	103

Chapter 1

Introduction

The scientific community has witnessed an explosion of interest and investment in the field of nanoscience and nanotechnology over the decades. The nanoscience revolution is one of the biggest things to happen since the beginning of modern science¹. A nanomaterial can be defined as a material that has a structure in which at least one of its phases has one or more dimensions in the nanometer size range (1–100 nm)². Nanomaterials have diverse tunable physical properties as a function of their size and shape due to strong quantum confinement effects and large surface to volume ratios. Such materials include polycrystalline materials with nanometer-sized crystallites, porous materials with particle sizes in the nanometer range or supported metal nanoparticles³⁻⁵. Metal nanoparticles have attracted much attention over the last decades owing to their relatively high chemical activity and specificity of interaction. One of the key driving forces for the rapidly developing field of nanoparticle synthesis is the distinctly differing physicochemical properties of metal nanoparticles as compared to their bulk counterparts⁶. Nanoparticles typically provide highly active centers, but they are not in a thermodynamically stable state. Structures at this size regime are indeed unstable as a result of their high surface energies and large surfaces^{7, 8}. A significant amount of research with the aim of inhibiting aggregation and producing highly active nanoparticles with homogeneous size dispersion has been published^{9, 10}. A mechanism to achieve this control is to utilise thermally stable and chemically inert supports that prevents the coalescence of metal nanoparticles. The unique properties of supported metal nanoparticles are directly related to the specific particle morphology (size and shape), metal dispersion and concentration of the metal within their host environment¹¹. Immobilisation and stabilisation of the nanoparticles allows exploitation of the special properties that occur at this size regime. In particular, nanometric metal, metal oxide and metal nitride particles embedded in inert matrices, present a variety of interesting magnetic, electric, catalytic properties and so on¹²⁻¹⁶. Depending on the chemical reactivity of the support, SiO₂ can be classified as an inert metal oxide¹⁷.

1.1 Sol-Gel Process

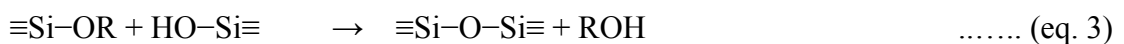
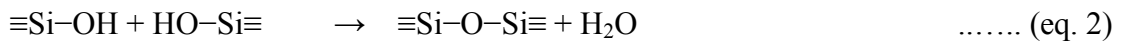
Sol-gel synthesis has been used for the production of metal, metal oxide and ceramic nanoparticles with high homogeneity as a result of homogeneous mixing of the precursor materials on the molecular level^{18, 19}. The sol-gel route offers some control of composition and structure at the molecular level. This process involves the evolution of inorganic networks through formation of a colloidal suspension (sol) and gelation of the sol to form a network in a continuous liquid phase (gel). In the process, reactive metal precursors such as metal alkoxide are initially hydrolyzed, followed by polycondensation reactions. The properties of a sol-gel inorganic network have been related to a number of critical process parameters such as pH, temperature and time of reaction, reagent concentrations, catalyst nature and concentration, H₂O/metal molar ratio, aging temperature and time, and drying.

The silica sol-gel process combines two main reactions: hydrolysis of an alkoxy silane to a silanol (eq. 1) and condensation of the silanol to a polysilicate framework (eq. 2 and eq. 3).

Hydrolysis



Condensation



Typically, tetraethoxysilane is hydrolysed by H₂O in acid or basic solution which acts as the hydrolysis catalyst to form the silanol molecules. Consequently, the condensation reaction occurs between the silanol moieties, and water or alcohol is released as the by product. The condensation reaction leads to formation of particles and/or networks. The colloidal particles condense to form a semisolid material, consisting of a three-dimensional solid “skeleton” enclosing the liquid phase²⁰.

A variety of solid materials with interesting properties can be made by the sol-gel technique, among them composites containing metal or metal oxide nanoparticles homogeneously dispersed in a silica matrix through sol-gel processing of tethered metal complexes²¹⁻²³. Extension of this synthesis methodology for the synthesis of new composites made up of metal nitride nanoparticles homogeneously distributed in a silica matrix would be a significant step towards functional nanocomposites.

1.2 Mesoporous Silica

Mesoporous materials are a class of 3D-nanostructures with well-defined mesoscale (2–50 nm diameter) pores, and surface areas up to $1000 \text{ m}^2/\text{g}$ ²⁴. Mesoporous materials are formed by a self-assembly process from combined solutions of sol-gel precursors (e.g. metal alkoxides) and structure-directing amphiphiles, usually block-copolymers or surfactants^{25, 26}. Mesoporous silica is defined as a nanoporous material with a polysilicate framework, with pore diameter between 2–50 nm. Mesoporous silica (MCM-41) synthesis is schematically displayed in Fig.1.1. It can be easily synthesized by the sol-gel method under acid or base conditions containing the silica precursor and the surfactant micelles as the template. The surfactant micelle is necessary to provide the mesopores inside silica matrix. Surfactant, e.g. cetyltrimethylammonium bromide, is used to form liquid crystalline micelles in water. The silica sol-gel precursor is added to this micellar solution to make, upon hydrolyses and condensation, a silica network around the micelles. One of the most popular of silica precursors is tetraethoxysilane (TEOS). Removal of the organic template by thermal treatment (calcination) or solvent extraction yields a mesoporous hexagonally ordered MCM-41 silica framework. The surfactant type, the surfactants combination, and the concentration of the surfactant strongly affect the mesopore morphology and size^{27, 28}.

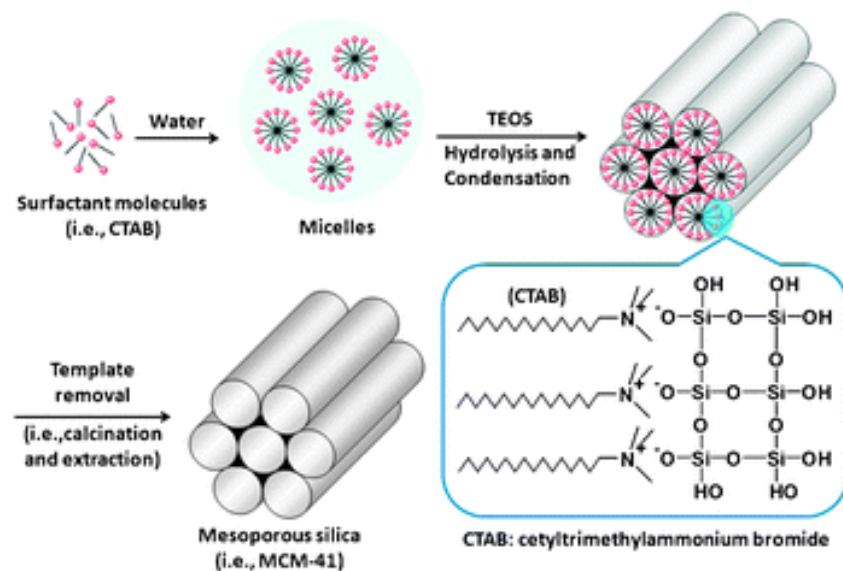


Figure 1.1 Schematic of the classical mesoporous silica (MCM-41) synthesis²⁹.

Mesoporous silicas have been widely investigated in a vast field of applications because of their many physiochemical properties such as high surface area, uniform pore size, low density, chemical inertness, and biocompatibility^{30, 31}. The synthesis of multifunctional core/shell nanocomposites, where transition metal and noble metal, metal oxide, metal nitride nanoparticles, and so on, have been encapsulated into the central spaces, while the mesoporous SiO₂ shells serve as controlled paths or gates to connect their enclosed interior materials to the outside space, offers great synthesis challenges³². Recent advances in the design and preparation of metal nanoparticles encapsulated in mesoporous hollow silica materials confirmed that there is plenty of room to synthesize a variety of nanoparticles through new preparation routes³³. The future generations of metal oxide and metal nitride nanoparticles cores with mesoporous silica shells will exhibit many new properties that will surely result in new applications with improved performance.

1.3 Metal Nitride Nanoparticles

Metal nitrides are a class of material, which have received growing attention during the past decade because of their technological importance. The transition metal nitrides are used because of their extremely high melting points, hardness, quasi metallic conduction properties, opto-electronic properties, as well as catalytic activity. For example, TiN melts at temperatures higher than 3000°C, is used for its hardness as super-hard coating in the manufacturing of cutting tools³⁴ and also its catalytic activity was reported^{35, 36}. VN is known for similar properties³⁷. Group III nitrides such as AlN and GaN are typical wide band-gap semiconductors and find a multitude of applications in high power, short-wavelength optoelectronic devices, in field-effect transistors, thermal radiation sensors and electric coatings³⁸.

Nanostructured metal nitride nanoparticles confined in a silica host matrix have interesting physical or chemical properties^{16, 39, 40}. The synthesis of different morphologies based on metal nitride nanoparticles-silica nanocomposites is the main focus of the present work. Such designer materials will have a significant impact in many areas including optics, catalysis and gas sensing.

1.4 Goal of Work

Nanoparticles possess high surface area and show changes in properties with respect to corresponding bulk material. This allows the production of new and interesting materials with well-defined and tuneable properties simply by controlling the nanoparticle size^{41, 42}. However, nanoparticles tend to agglomerate because of high surface energy. Immobilisation and stabilisation of the nanoparticles in/on inert support allows exploitation the unique properties occurring at the nanoscale regime.

Metal nitrides are fundamentally important materials that have a wide range of technological applications. Compared to oxides, they have some superior properties, such as high hardness, high melting point, excellent electronic characteristics, and good catalytic properties⁴³. However, the availability of metal nitride nanostructures is still very restricted and their synthesis is full of potential complications. Hence, further developments are necessary to get well defined metal nitride nanoparticles. Such nanoparticle may have applications in fields such as biomedicine, catalysis, electronics, semiconductor devices, and high performance mechanics.

The main aim of this work is to implement new synthetic ways for the preparation of nanocomposites mainly based on metal nitride nanoparticles in/on silica. The exploration of the technological potential of the prepared metal nitride nanoparticles in/on silica is not within the scope of this thesis.

Sol-gel processing allows the preparation of non-agglomerated metal oxide or metal nanoparticles within a silica matrix with narrow particle size distributions and adjustable metal loading, if the metal precursor is tethered to the gel network during sol-gel processing. The extension of this methodology to synthesize a variety of nanocomposites, in which metal nitride nanoparticles are homogeneously embedded in a silica matrix, was of particular interest.

The carbon sphere templating strategy offers the opportunity to synthesize hollow morphologies with functionalised inner cores. This method was used for the synthesis of metal nitride nanoparticles inside hollow mesoporous silica spheres. It was intended to adsorb copper ions onto the carbon spheres followed by sol-gel processing of a silica precursor, subsequent calcination and nitridation to form copper nitride nanoparticles in hollow mesoporous silica spheres.

The conversion of metal silicate nanostructures into new chemical structures by subsequent reactions generated the idea to explore metal silicates as source for the synthesis of metal

nitride-silica and metal oxide-silica. Therefore, synthesis procedures were planned for CuO@SiO_2 and $\text{Cu}_3\text{N@SiO}_2$ hierarchical hollow spheres (HHSs) starting from copper silicate HHSs by thermal disintegration in air or nitridation.

Crystalline SrTiO_3 is a promising thermoelectric material at higher temperatures. In order to improve thermoelectric efficiency of SrTiO_3 , reduction of the thermal conductivity without affecting the electrical conductivity was of crucial interest. Therefore, nanocomposites based on strontium titanate/strontium carbonate were planned to investigate the thermoelectric performance. SrCO_3 in the $\text{SrTiO}_3/\text{SrCO}_3$ composites would help to scatter the phonons and hence to reduce thermal diffusivity leading to high thermoelectric efficiency.

1.5 References

1. Mirkin, C. A. *Small* **2005**, 1, (1), 14-16.
2. Campelo, J. M.; Luna, D.; Luque, R.; Marinas, J. M.; Romero, A. A. *Chemsuschem* **2009**, 2, (1), 18-45.
3. Murphy, C. J.; San, T. K.; Gole, A. M.; Orendorff, C. J.; Gao, J. X.; Gou, L.; Hunyadi, S. E.; Li, T. *Journal of Physical Chemistry B* **2005**, 109, (29), 13857-13870.
4. Gray, B. M.; Hassan, S.; Hector, A. L.; Kalaji, A.; Mazumder, B. *Chemistry of Materials* **2009**, 21, (18), 4210-4215.
5. Phonthammachai, N.; White, T. J. *Langmuir* **2007**, 23, (23), 11421-11424.
6. Cuenya, B. R. *Thin Solid Films* **2010**, 518, (12), 3127-3150.
7. Cao, A.; Lu, R.; Veser, G. *Physical Chemistry Chemical Physics* **2010**, 12, (41), 13499-13510.
8. De Rogatis, L.; Cargnello, M.; Gombac, V.; Lorenzut, B.; Montini, T.; Fornasiero, P. *Chemsuschem* **2010**, 3, (1), 24-42.
9. Rostovshchikova, T. N.; Smirnov, V. V.; Kozhevin, V. M.; Yavsin, D. A.; Zabelin, M. A.; Yassievich, I. N.; Gurevich, S. A. *Applied Catalysis a-General* **2005**, 296, (1), 70-79.
10. Dahl, J. A.; Maddux, B. L. S.; Hutchison, J. E. *Chemical Reviews* **2007**, 107, (6), 2228-2269.
11. White, R. J.; Luque, R.; Budarin, V. L.; Clark, J. H.; Macquarrie, D. J. *Chemical Society Reviews* **2009**, 38, (2), 481-494.
12. Matura, V.; Guari, Y.; Reye, C.; Corriu, R. J. P.; Tristany, M.; Jansat, S.; Philippot, K.; Maisonnat, A.; Chaudret, B. *Advanced Functional Materials* **2009**, 19, (23), 3781-3787.
13. Huang, Z. W.; Cui, F.; Kang, H. X.; Chen, J.; Zhang, X. Z.; Xia, C. G. *Chemistry of Materials* **2008**, 20, (15), 5090-5099.
14. Liu, H. Y.; Ma, D.; Blackley, R. A.; Zhou, W. Z.; Bao, X. H. *Chemical Communications* **2008**, (23), 2677-2679.
15. Tan, M. Q.; Munusarny, P.; Mahalingam, V.; van Veggel, F. C. J. M. *Journal of the American Chemical Society* **2007**, 129, (46), 14122-14123.
16. Lee, B. S.; Yi, M.; Chu, S. Y.; Lee, J. Y.; Kwon, H. R.; Lee, K. R.; Kang, D.; Kim, W. S.; Bin Lim, H.; Lee, J.; Youn, H. J.; Chi, D. Y.; Hur, N. H. *Chemical Communications* **2010**, 46, (22), 3935-3937.
17. Qian, K.; Lv, S. S.; Xiao, X. Y.; Sun, H. X.; Lu, J. Q.; Luo, M. F.; Huang, W. X. *Journal of Molecular Catalysis a-Chemical* **2009**, 306, (1-2), 40-47.

18. Tjong, S. C.; Chen, H. *Materials Science & Engineering R-Reports* **2004**, 45, (1-2), 1-88.
19. Sui, R.; Charpentier, P. *Chemical Reviews* **2012**, 112, (6), 3057-82.
20. Brinker C. J.; Scherer G. W., *Sol-Gel Science - The Physics and Chemistry of Sol-Gel Processing* Academic Press Inc. , New York, 1990.
21. Lembacher, C.; Schubert, U. *New Journal of Chemistry* **1998**, 22, (7), 721-724.
22. Trimmel, G.; Lembacher, C.; Kickelbick, G.; Schubert, U. *New Journal of Chemistry* **2002**, 26, (6), 759-765.
23. Schubert, U. *Advanced Engineering Materials* **2004**, 6, (3), 173-176.
24. Beck, J. S.; Vartuli, J. C. *Current Opinion in Solid State & Materials Science* **1996**, 1, (1), 76-87.
25. Beck, J. S.; Vartuli, J. C.; Roth, W. J.; Leonowicz, M. E.; Kresge, C. T.; Schmitt, K. D.; Chu, C. T. W.; Olson, D. H.; Sheppard, E. W.; Mccullen, S. B.; Higgins, J. B.; Schlenker, J. L. *Journal of the American Chemical Society* **1992**, 114, (27), 10834-10843.
26. Wan, Y.; Zhao, D. Y. *Chemical Reviews* **2007**, 107, (7), 2821-2860.
27. Kim, J. M.; Sakamoto, Y.; Hwang, Y. K.; Kwon, Y. U.; Terasaki, O.; Park, S. E.; Stucky, G. D. *Journal of Physical Chemistry B* **2002**, 106, (10), 2552-2558.
28. Cheng, Y. R.; Lin, H. P.; Mou, C. Y. *Physical Chemistry Chemical Physics* **1999**, 1, (21), 5051-5058.
29. Yang, P. P.; Gai, S. L.; Lin, J. *Chemical Society Reviews* **2012**, 41, (9), 3679-3698.
30. Liu, J.; Qiao, S. Z.; Hu, Q. H.; Lu, G. Q. *Small* **2011**, 7, (4), 425-443.
31. Wu, P. P.; Xiong, Z. G.; Loh, K. P.; Zhao, X. S. *Catalysis Science & Technology* **2011**, 1, (2), 285-294.
32. Ghosh C. R.; Paria, S. *Chemical reviews* **2012**, 112, (4), 2373-433.
33. Wang, D. P.; Zeng, H. C. *Chemistry of Materials* **2011**, 23, (22), 4886-4899.
34. Sproul, W. D. *Surface & Coatings Technology* **1996**, 81, (1), 1-7.
35. Kaskel, S.; Schlichte, K.; Kratzke, T. *Journal of Molecular Catalysis a-Chemical* **2004**, 208, (1-2), 291-298.
36. Ramanathan, S.; Oyama, S. T. *Journal of Physical Chemistry* **1995**, 99, (44), 16365-16372.
37. Krawiec, P.; De Cola, P. L.; Glaser, R.; Weitkamp, J.; Weidenthaler, C.; Kaskel, S. *Advanced Materials* **2006**, 18, (4), 505-508.
38. Edgar, J. H. *Journal of Materials Research* **1992**, 7, (1), 235-252.

39. Munusamy, P.; Mahalingam, V.; van Veggel, F. C. J. M. *European Journal of Inorganic Chemistry* **2008**, 2008, (23), 3728-3732.
40. Sinha, G.; Panda, S. K.; Mishra, P.; Ganguli, D.; Chaudhuri, S. *Journal of Physics-Condensed Matter* **2007**, 19, (34), 346209.
41. Huang, J.; Bu, L. H.; Xie, J.; Chen, K.; Cheng, Z.; Li, X. G.; Chen, X. Y. *Acs Nano* **2010**, 4, (12), 7151-7160.
42. Ba, J. H.; Polleux, J.; Antonietti, M.; Niederberger, M. *Advanced Materials* **2005**, 17, (20), 2509-2512.
43. Du, Y. X.; Lei, M.; Yang, H. *Journal of Materials Science & Technology* **2008**, 24, (5), 737-741.

Chapter 2

Metal Nitride@SiO₂ and CuS@SiO₂ Nanocomposites by Sol-Gel Processing Starting from Tethered Metal Complexes

Nanocomposite materials consisting of very small particles of a guest compound (typically having diameters less than 100 nm) dispersed throughout a host matrix are of intense interest for potential applications as catalysts, magnetic, electronic, and photonic materials.¹⁻⁶

Nanocomposites with different morphologies, structures, and particle sizes can be broadly categorized into four types: monodisperse nanoparticles embedded in an inert matrix (Fig. 2.1 A), nanoparticles covered with a shell of another material known as core-shell particles (Fig. 2.1 B), ordered mesoporous materials loaded with nanoparticles inside the porous channels or cages (Fig. 2.1 C), and nanoparticles distributed on solid morphologies (Fig. 2.1 D).

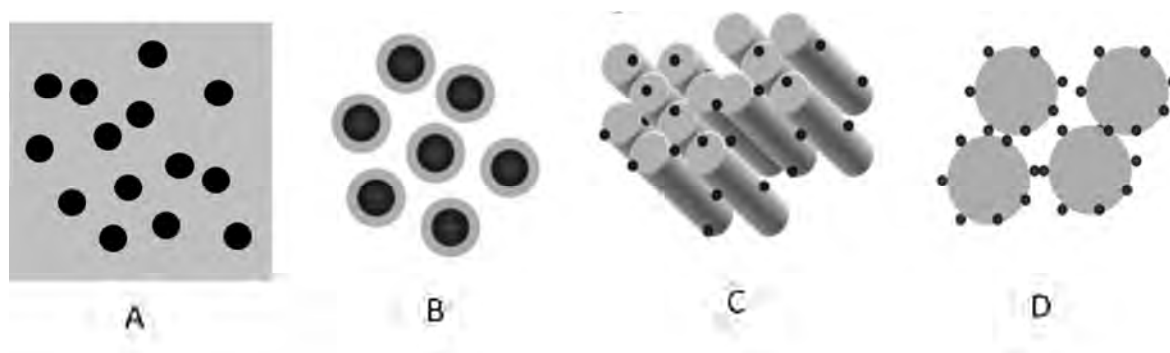


Fig. 2.1 Schematic representations of different nanocomposite morphologies.

Nanoparticles have immense applications in various disciplines⁷⁻¹⁰. However, some problems are associated with them, such as intrinsic instability over long periods due to their tendency to aggregate in order to reduce surface energy. The aggregation of NPs can significantly decrease their interfacial area, thus resulting in the loss of properties arising from nanosize effects. It is therefore crucial to develop strategies to stabilise the nanoparticles against aggregation. Research has shown that hosting nanoparticles in an inert host matrix such as polymers, silica, or other materials can prevent aggregation¹¹⁻¹³. The host matrix supports nanoparticles and provides a physical barrier for migration of the nanoparticles, and thus effectively prevents sintering^{14, 15}.

The focus of this work was on the synthesis and characterisation of different types of metal nitride nanoparticles as well as copper sulphide nanoparticles in a silica matrix starting from sol-gel processing of tethered metal complexes.

2.1 Metal Nitrides

Copper Nitride (Cu_3N)

Copper nitride is a promising material having suitable optical and electronic properties for optical storage devices, high-speed integrated circuits, and microscopic metal links¹⁶⁻¹⁹. The crystal structure of Cu_3N is shown in Fig. 2.2. The structure is made of nitrogen centered octahedra which are corner connected to each other. Cu_3N is a semiconductor with a small indirect band-gap²⁰. Cu_3N is nontoxic and stable in air at room temperature¹⁶.

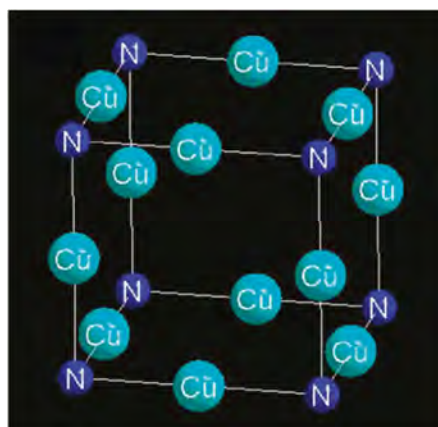


Fig. 2.2 Crystal structure of Cu_3N

In the literature, work has been focused on the synthesis of Cu_3N films by various techniques for desired applications²¹⁻²⁵. Recently $\text{Cu}_3\text{N}/\text{Fe}_3\text{N}$ nanoparticles supported on silica microspheres were used as new catalysts for azide-alkyne click reactions²⁶.

Gallium Nitride (GaN)

Wurtzite-structured GaN is a wide-band-gap semiconductor (energy gap, 3.39 eV) that exhibits luminescence and conduction properties, and thus has potential applications in optoelectronic devices, high-temperature stable gas sensors and high-temperature/high-power electronic devices²⁷⁻³¹. Nanostructured GaN with varied morphology, for instance,

nanoparticles, nanorods, nanowires, nanobelts, and nanotubes has been synthesized³². GaN/SiO₂ nanocomposites exhibited yellow and bright blue luminescence^{33, 34}.

Cobalt Nitride (Co₂N)

Co₂N crystallises into the orthorhombic crystal system. Several cobalt nitride phases have been reported in the literature e.g. CoN, Co₂N, Co₃N, Co₄N, and Co₃N₂^{35, 36}. Being poor in thermal stability, the nitrides of cobalt have received less attention³⁷.

Chromium Nitride (CrN)

Chromium nitride (CrN) has been found to be antiferromagnetic with the Néel temperature of 273–290 K³⁸. In addition, CrN shows unique semiconducting properties. These characteristics, together with the high thermal stability, abrasion resistance, antifriction coefficient, and antioxidation properties open a wide door for its application³⁹⁻⁴².

Vanadium Nitride (VN)

VN has a cubic, rock salt structure. It is currently one of the most promising materials for electrodes of supercapacitors, due to its ability to deliver an impressive specific capacitance as high as 1340 F/g in the form of thin films in a three-electrode cell⁴³. Furthermore, vanadium nitride is a highly active and selective butane dehydrogenation catalysts^{44, 45}.

2.2 Synthesis of Metal Nitrides

Traditionally, nitrides are obtained by heating the metals in flowing nitrogen gas at high temperatures. This route is limited to only certain kinds of nitrides due to the inertness of nitrogen gas⁴⁶. A more viable route is to use the precursor ammonia instead of nitrogen gas in reacting with the metals or metal oxides. Nanocrystalline metal oxides can be converted to metal nitrides by ammonia nitridation reaction. Gas-phase reactions of dry oxide powders with NH₃ are most common. For example, Gao and co-workers have converted nanoparticles of TiO₂, Cr₂O₃, In₂O₃, Ta₂O₅, and Al₂O₃ to metal nitrides of TiN⁴⁷, CrN⁴⁸, InN⁴⁹, Ta₃N₅⁵⁰, and AlN⁵¹, respectively, by nitridation methods. In all cases the oxide nanoparticles converted

completely to nitrides at relatively low temperatures and short heating times while micron-scale powders did not convert completely under equivalent conditions, demonstrating the effect that nanoscale precursors have on reactivity. Other reactions with NH_3 gas at elevated temperatures have been used to produce TiN^{52} and GaN^{53} . In particular, reacting nanocrystalline Ga_2O_3 in the pores of an alumina membrane with NH_3 gas at 1000°C yielded GaN nanoparticles with a diameter of 23.8 nm, which agrees well with the pore diameter of 24 nm⁵³. The morphology of metal oxide nanoparticle precursors can template the morphology of metal nitride nanocrystal products. For example, Hu et al.⁵⁴ reacted amorphous Ga_2O_3 nanotubes with NH_3 at 1400°C for 1 h to generate GaN nanotubes with lengths up to 10 μm , diameters of 80 nm and wall thickness of 20 nm. Conversion reactions mentioned above involve nitridation of metal oxides at elevated temperatures in a NH_3 atmosphere; other nitrogen sources can also be used. For example, Buha et al. reacted appropriate metal oxide nanoparticles with cyanamide or urea to form VN , TiN , AlN , GaN , NbN , TaN , and $\text{Hf}_2\text{ON}_2^{55}$. Tang et al. synthesized metal nitrides through melamine and metal oxides. Other routes such as carbothermal or solvothermal methods, and the pyrolysis of molecular reagents were successful in synthesizing some nitrides⁵⁶⁻⁵⁸.

2.3 Copper Sulphide (CuS)

In addition to metal nitrides, metal sulphides represent an important family of inorganic functional materials for various applications⁵⁹⁻⁶¹. Nanostructured metal sulphides have been extensively studied due to their importance in interpreting quantum size effects and applications in a variety of devices, such as solar cells, light-emitting diodes, sensors, thermoelectric devices, lithium-ion batteries, fuel cells and nonvolatile memory devices⁶²⁻⁶⁷. As a typical representative, copper sulphide nanocrystals, which are expected to be a prominent candidate for optical devices due to their high third-order nonlinear optical susceptibility (about 10^{-7}esu)⁶⁸. Copper sulphides are known in various stoichiometries, at least five phases of which are stable at room temperature: i.e., covellite (CuS), anilite ($\text{Cu}_{1.75}\text{S}$), digenite ($\text{Cu}_{1.8}\text{S}$), djurlite ($\text{Cu}_{1.95}\text{S}$), and chalcocite (Cu_2S). Their complex structures and valence states result in some unique properties and promising applications in numerous fields⁶⁹. Copper monosulphide (CuS) is an excellent semiconductor having potential applications in solar cells, catalyst, cathode material, optical filters, and so on⁷⁰⁻⁷².

2.4 Synthesis of Metal Sulphides

Metal sulphide nanostructures have been synthesized by a variety of chemical or physical methods. Among these are solution-phase reactions, hydrothermal growth, physical vapor deposition (PVD) and chemical vapor deposition (CVD)⁷³⁻⁷⁵.

Metal oxides are often used as precursors to sulphides, for example the use of WO_3 and MoO_3 as precursors for the inorganic fullerenes WS_2 and MoS_2 via reaction with H_2S ⁷⁶. H_2S has been used as a sulphur source for a number of other reactions, including the formation of oxides via hydrothermal, solvothermal, sonochemical, electrochemical, or direct chemical methods followed by heating in the presence of H_2S ⁷⁷⁻⁸¹. In some cases, the oxide is reacted with different sulphur sources such as thioglycolic acid, thiourea, or elemental sulphur to produce the corresponding sulphide. For example, ZnO/ZnS , $\text{SnO}_2/\text{SnS}_2$, $\text{MnO}_2/\text{MnS}_2$ core-shell nanostructures, and nanotubes of ZnS and SnS_2 were formed when the corresponding oxide was reacted with Na_2S and thioglycolic acid⁸². Thiourea was used as the sulphur source to produce hollow ZnS from polymer-stabilized ZnO nanoparticles⁸³, and also for 18-faceted Cu_7S_4 hollow nanoparticles from Cu_2O ⁸⁴. CuS nanoparticles were synthesized hydrothermally from CuO and $\text{Na}_2\text{S}_2\text{O}_3 \cdot 5\text{H}_2\text{O}$ ⁸⁵. MoO_3 was converted to MoS_2 using elemental sulphur and heating to 850 °C. Recently, Zeng et.al proposed synthesis of phase-pure CuS hollow spheres by reaction of Cu_2O nanospheres suspension with aqueous $(\text{NH}_4)_2\text{S}$ ⁸⁶.

2.5 Metal Oxide@ SiO_2 and Metal@ SiO_2 Nanocomposites

Nanocomposites, in which metal oxide or metal nanoparticles are embedded in a silica host matrix, can be easily prepared by sol-gel processing. However, homogeneous distribution of the nanoparticles in the host matrix and the average particle size is often difficult to control³⁴. Previous work by our group has proven that selectively anchoring the metal precursor to the gel matrix by using organically modified silica precursors allows homogeneous dispersion of the metal ions throughout the host structure during the sol-gel step and prevents aggregation of metal ions. This leads to control over average particle size and homogeneous distribution of nanoparticles throughout the host matrix⁸⁷⁻⁹⁵. Thus sol-gel processing of tethered metal complexes allows homogeneous distribution of nanosized particles through the silica host matrix. Metal complexes substituted by amino-functionalised alkoxy silanes function as a single source precursor for the synthesis of nanometer-sized, homogeneously dispersed transition metal, metal oxide, noble metal and bimetallic alloy particles in a SiO_2 matrix⁸⁷⁻⁸⁹.

⁹³. A Scheme for the synthesis of metal oxide/metal@SiO₂ nanocomposites is given in Fig. 2.3.

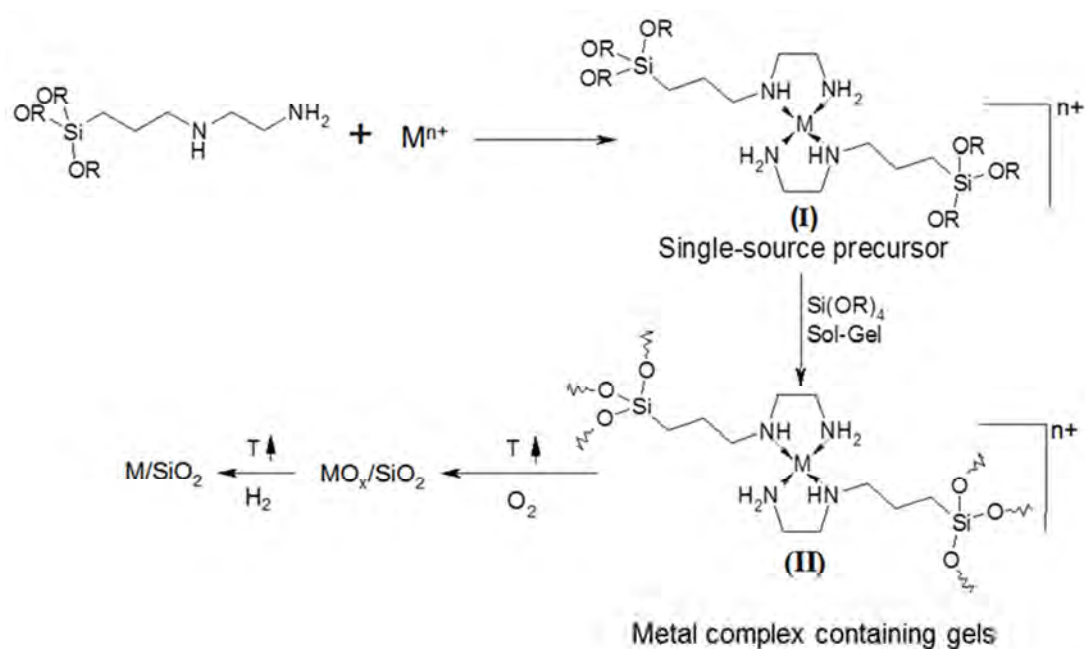


Fig. 2.3 Synthesis of metal oxide/metal@SiO₂ nanocomposites by sol-gel processing of tethered metal complexes.

Reaction of amino-functionalised alkoxy silanes with metal salts results in the in-situ formation of complexes. Amino functionalities from substituted alkoxy silanes tether the metal compound to the silicate network during sol-gel processing. The two-component system (metal salt + alkoxy silane) is thus converted to a single-source precursor (I).

A series of metal salts was homogeneously dispersed in a sol-gel matrix with the aid of organofunctional alkoxy silane precursors, such as (RO)₃Si(CH₂)₃X, (R= methyl, ethyl; X = CN, NH₂, NH-CH₂-CH₂-NH₂ or NH-CH₂-CH₂-NH-CH₂-CH₂-NH₂). Sol-gel processing under standard conditions yields metal complex containing gels (II). Subsequent controlled thermolysis in air results in the degradation of the organic components with concomitant formation of metal oxide nanoparticles in SiO₂ matrix (metal oxide@SiO₂). The particle size and the porosity of the matrix can be influenced by several parameters, such as nature of complexing silane, counter-ion of the employed salt and heat treatment⁹⁵. Metal oxide@SiO₂ gives metal@SiO₂ by hydrogenation at higher temperature. Thus highly dispersed metal nanoparticles in SiO₂ matrix are obtained.

Based on those results we introduce this methodology for the synthesis of metal nitride nanoparticle in SiO₂ matrix. The motivation to attempt the synthesis of metal nitride nanoparticles in SiO₂ matrix was emanated from their technological importance⁹⁶⁻¹⁰⁰.

Synthesis methodologies developed by our group for the synthesis of metal oxide@SiO₂ nanocomposites were followed. Furthermore, metal nitride@SiO₂ nanocomposites were obtained by further nitridation reactions of metal oxide@SiO₂ nanocomposites at elevated temperatures.

2.6 Results and Discussion

In this section various metal nitride nanoparticles in silica host matrix are synthesized and characterised.

2.6.1 Cu₃N@SiO₂ Nanocomposite

A very first example to extend sol-gel processing of amino functionalised alkoxy silane substituted metal complexes (single-source precursor) to metal nitride@SiO₂ is the Cu₃N@SiO₂ nanocomposite.

The synthesis of Cu₃N@SiO₂ as a representative is schematically shown in Fig. 2.4.

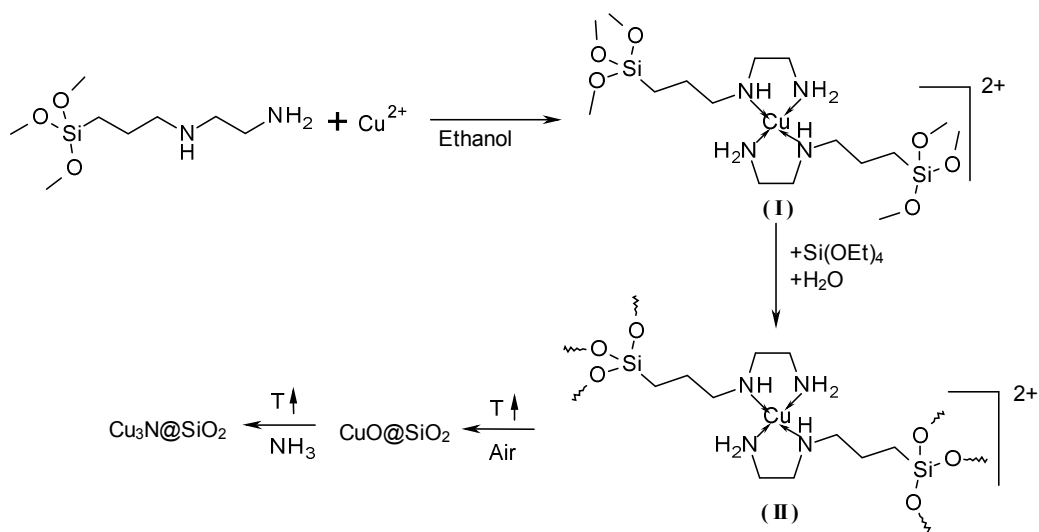


Fig. 2.4 Synthesis of Cu₃N@SiO₂ nanocomposites by sol-gel processing of tethered metal complexes.

The synthesis were carried out by using copper acetate as metal precursor, and two equivalents of AEAPTS ($\text{H}_2\text{NCH}_2\text{CH}_2\text{NH}(\text{CH}_2)_3\text{Si}(\text{OMe})_3$) as the complexing silane. Detailed synthesis procedure is given in section 6.3.1.1. Addition of amino-substituted silanes to ethanolic suspensions of copper acetate results in in-situ formation of a copper complex $[\text{Cu}(\text{AEAPTS})_2]^{2+}$ (I). The colour of the solution changed from green to blue-violet

immediately after addition of AEAPTS. The UV spectrum of the resulting solution ($\lambda_{\text{max}} = 593 \text{ nm}$) also supported the formation of complex I (Fig. 2.5).

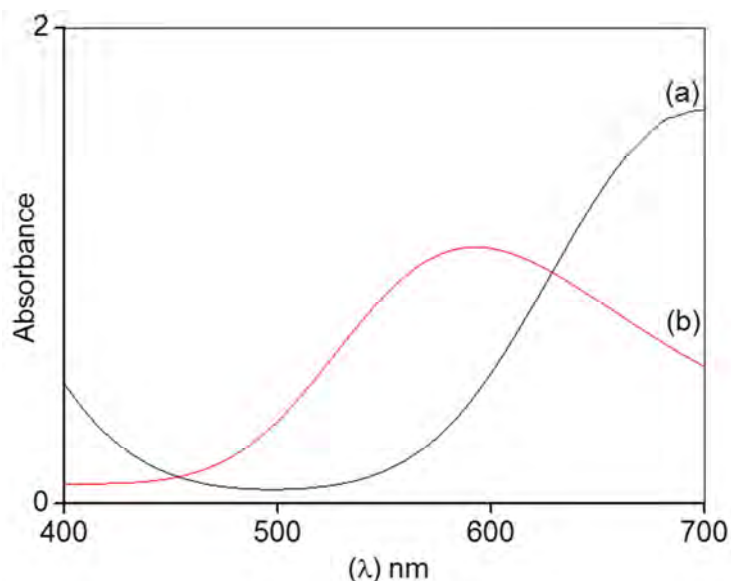


Fig. 2.5 UV spectra of (a) $\text{Cu}(\text{OAc})_2 \cdot \text{H}_2\text{O}$ in ethanolic solution and (b) $\text{Cu}(\text{OAc})_2 \cdot \text{H}_2\text{O}$ and two equivalents of AEAPTS in ethanolic solution.

The two-component system (copper salt + AEAPTS) is thus converted to a single-source precursor with all associated advantages. The single-source precursor was processed by the sol-gel method under basic conditions yields metal complex containing gels (II). The TEOS proportion was chosen so that the final composite had a theoretical Cu_3N content of 8.1 wt %. Metal coordination to the amino group is retained during sol-gel processing, i.e. the copper ions are tethered to the gel matrix via $(\text{CH}_2)_3\text{SiO}_{3/2}$ entities. Aggregation of the copper ions is thus prevented and the tethered copper complexes are homogeneously distributed in the resulting gel matrix. After sufficient gelation time a blue coloured gel (II) was obtained (photographic image in Fig. 2.6), which was dried under reduced pressure.



Fig. 2.6 Photographic image of the obtained gel II.

TGA of the dried gel II (Fig. 2.7) showed that after the loss of adsorbed water at about 110 °C, the main degradation of the organic components of gel II occurred in the range of 150–350 °C. Since an additional ca. 2% weight loss was observed in the range of 350–800 °C the sample was heated to 800 °C in air and CuO nanoparticles were formed. Although this resulted in larger particles and a broader particle size distribution, this temperature was chosen to ensure removal of all carbon residuals which could give rise to carbide or carbonitride species. The calcination temperature must be high enough to remove all organic groups, but should not be too high to avoid excessive growth of metal oxide nanoparticles. During calcination metal oxide nanoparticles start to grow simultaneously with the removal of organic groups i.e. CuO@SiO₂ composite is formed. The colour of the metal complex-containing dry gel changed from blue to black during calcination process.

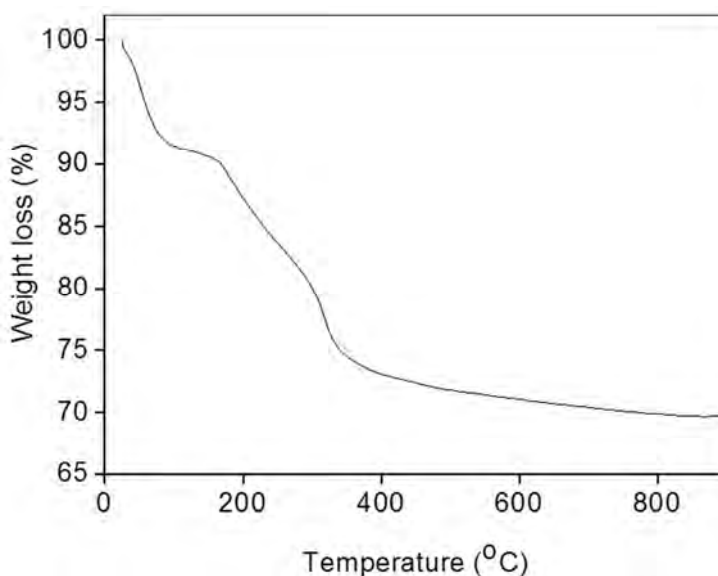


Fig. 2.7 TGA profile of the dry gel.

The CuO@SiO₂ nanocomposite was reacted with ammonia at 300 °C for 8 h in a horizontal tube furnace, and a brown Cu₃N@SiO₂ nanocomposite was obtained. The formation of CuO@SiO₂ and Cu₃N@SiO₂ nanocomposites was confirmed by XRD studies. The XRD pattern of the CuO@SiO₂ nanocomposites after calcination at 800 °C exhibited monoclinic CuO nanocrystals (JCPDS 41-0254) as shown in Fig. 2.8 (a). After nitridation, the diffraction pattern corresponded to cubic Cu₃N nanoparticles (JCPDS-86-2283) (Fig. 2.8 (b)). The average sizes of the CuO and Cu₃N particles, calculated by the Scherrer equation, were 11 and 14 nm, respectively. A broad peak at < 30 degrees is due to amorphous silica.

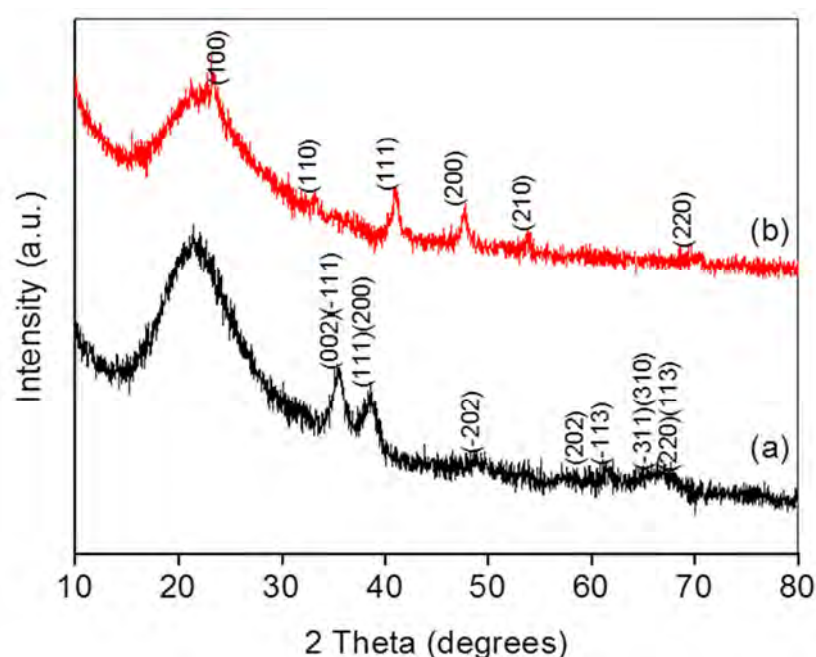


Fig. 2.8 XRD pattern of CuO@SiO₂ (a) and Cu₃N@SiO₂ (b).

During the nitridation reaction it was found that the temperature and duration plays a crucial role, and it is important to optimize nitridation reaction parameters to get a phase-pure Cu₃N@SiO₂ nanocomposite. In the present case, when nitridation temperature was less than 300 °C then a mixture of Cu₂O and Cu₃N was formed. Fig. 2.9 (b) shows reflections for Cu₂O and Cu₃N after nitridation of the CuO@SiO₂ nanocomposite at 275 °C for 8 h. Also, when the nitridation temperature was >300 °C; copper nanoparticles along with Cu₃N and Cu₂O nanoparticles were formed. The XRD pattern of CuO@SiO₂ nanocomposite nitrided at 325 °C for 8 h under ammonia atmosphere is shown in Fig. 2.9 (a). It clearly shows reflections for Cu, Cu₂O and Cu₃N.

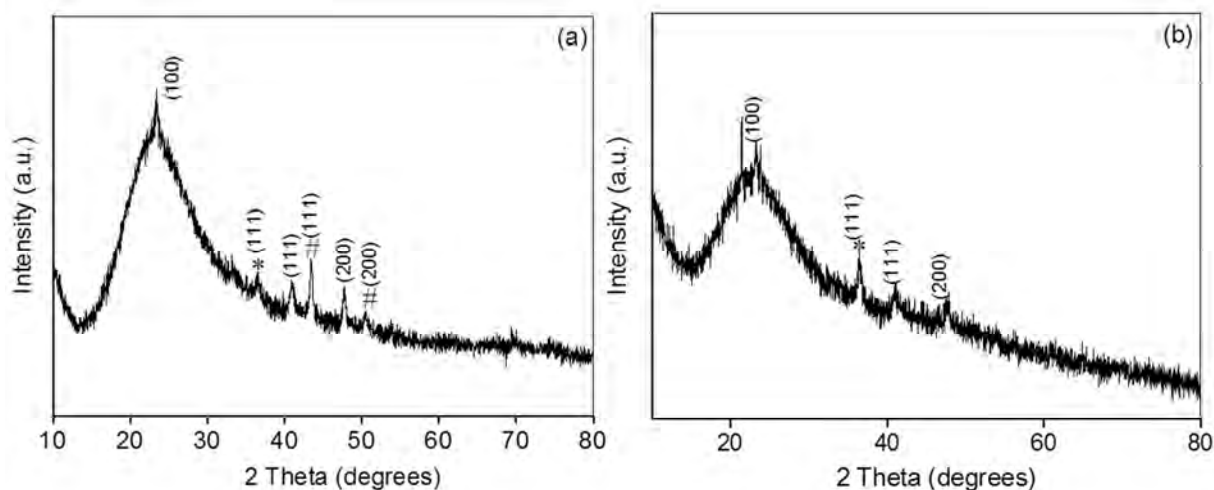


Fig. 2.9 XRD pattern of nitridation products of CuO@SiO_2 nanocomposite at 325 (a) and 275 °C (b) for 8h. (* Cu_2O , # Cu, unmarked reflections corresponds to Cu_3N in Fig. 2.9 a, b)

The $\text{Cu}_3\text{N@SiO}_2$ nanocomposite was analysed by STEM and EDX. The STEM image (Fig. 2.10(a)) of the $\text{Cu}_3\text{N@SiO}_2$ nanocomposite shows distinct nanosized particles fairly well-dispersed in the amorphous silica matrix. The particle sizes are less than 15 nm which is in good agreement with the particle size calculated by the Scherrer equation. To confirm that these bright particles are consisting of Cu_3N , a line scan across two particles (Fig. 2.10(b)) was performed. The count for copper species increases on the brighter regions which supports the presence of copper-containing species.

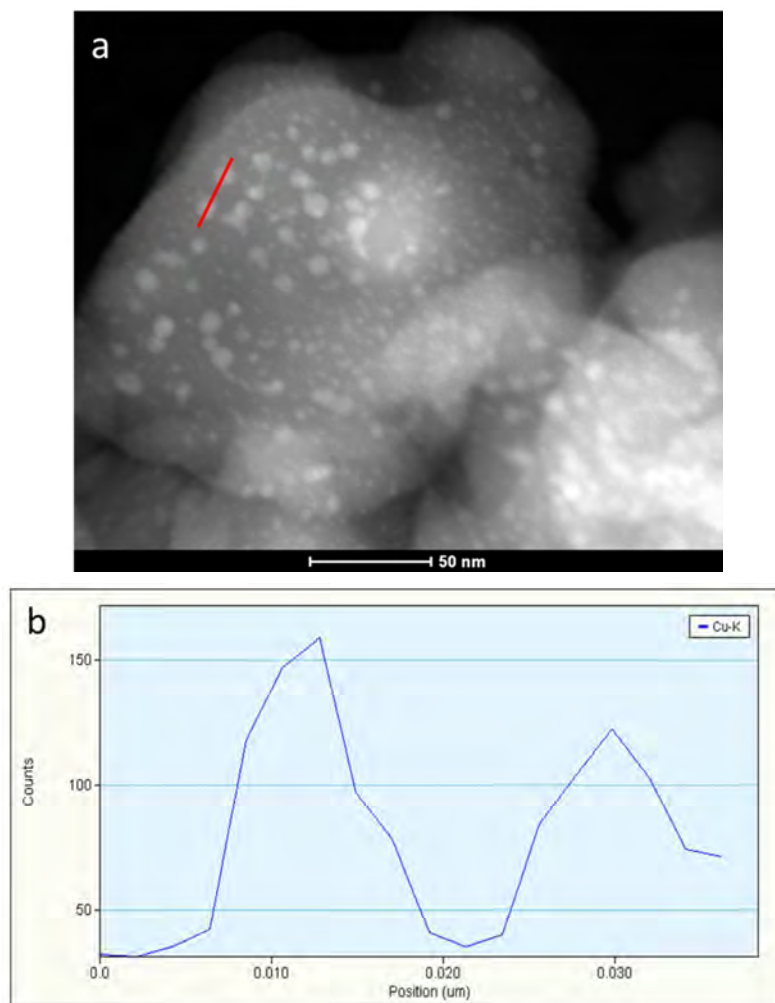


Fig. 2.10 STEM image (a) and (b) EDX line scan profile across two Cu₃N nanoparticles from the Cu₃N@SiO₂ nanocomposite.

2.6.2 GaN@SiO₂ Nanocomposite

Synthesis of a GaN@SiO₂ nanocomposite was performed by employing a similar method. The general procedure for the preparation of the dry gel was same as for Cu₃N@SiO₂. The synthesis were carried out by using Ga(NO₃)₃·H₂O as metal precursor, and three equivalents of AEAPTS as the complexing silane. The detailed synthesis procedure is given in section 6.3.1.2. Thermogravimetric analysis of the dry gel showed weight loss up to 700 °C for the complete removal of organic moieties (Fig. 2.11 (a)). After TGA analysis, the dried gel was calcined at 800 °C for 2 h in air. The XRD pattern of the calcined sample is shown in Fig. 2.11 (b), indicating formation of amorphous Ga/O structures.

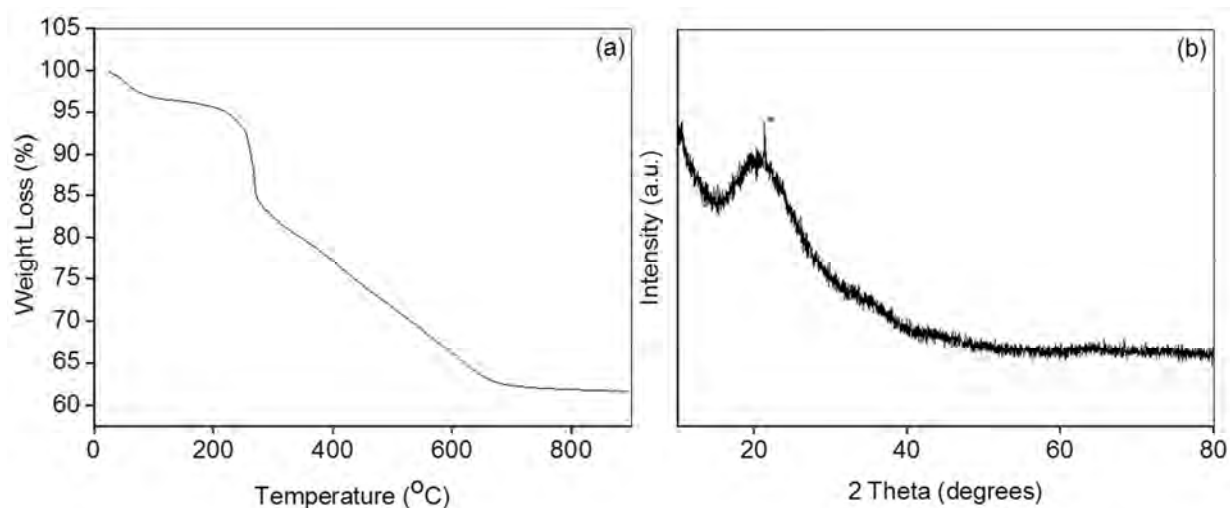


Fig. 2.11 (a) TGA of the dried gel and (b) XRD pattern of the dry gel calcined at 800 °C in air (* cristobalite).

Nitridation of the (amorphous) Ga/O structures at 900 °C for 3 h under ammonia atmosphere leads to formation of crystalline GaN nanoparticles. In the present case the temperature required is higher compared to the case of $\text{Cu}_3\text{N}@SiO_2$. The colour of the sample changed to a light yellowish white after nitridation reaction. The XRD pattern (Fig. 2.12 (a)) shows reflections corresponding to wurtzite GaN and a broad hump at < 30 degrees for amorphous silica. The average particle size of GaN particles calculated by the Scherrer equation is 20 nm which corresponds very well with the TEM image where ~20 nm sized particles were observed (Fig. 2.12 (b)).

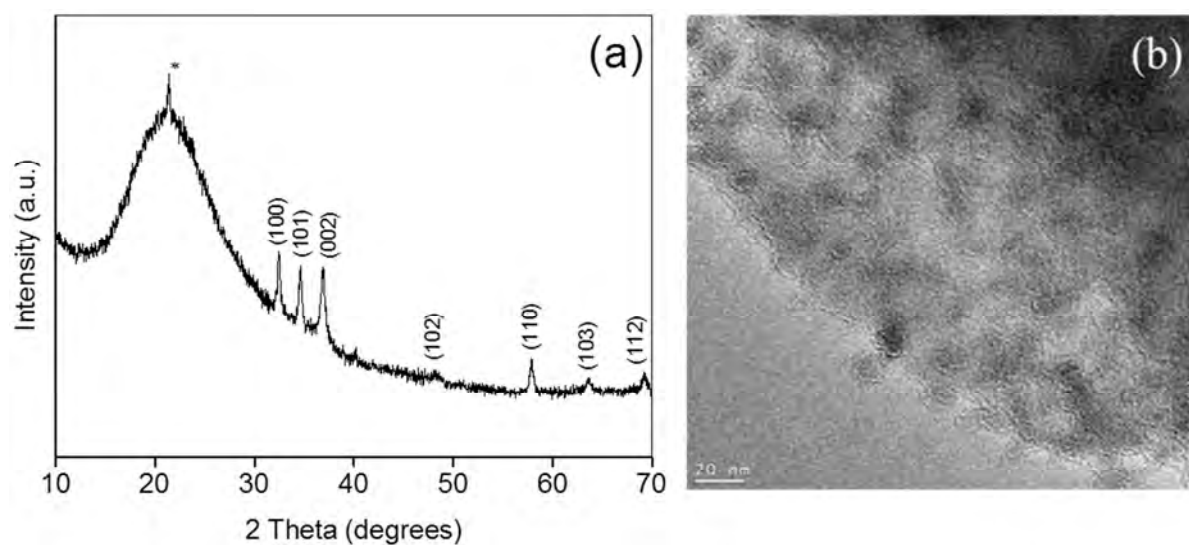


Fig. 2.12 (a) XRD pattern, (b) TEM image of GaN@SiO₂ nanocomposite. (*cristobalite SiO₂)

2.6.3 CrN@SiO₂ Nanocomposite

The synthesis of CrN@SiO₂ nanocomposite were carried out by using Cr(NO₃)₃·9H₂O as metal precursor, and three equivalents of AEAPTS. The detailed synthesis procedure is given in section 6.3.1.3. The colour of the solution changed from green to cadet blue immediately after addition of AEAPTS. TGA of the dried gel (Fig. 2.13) indicated a two-step weight loss pattern, the major weight loss (ca. 45%) at about 210 °C and a second step at 300–400 °C. Based on TGA result, calcination temperatures of 400°C and 500°C were chosen in order to study the effect of calcination temperature on crystallite size of chromium oxide nanoparticles in the silica matrix. The chromium oxide nanoparticles are formed simultaneously during removal of organic groups giving Cr₂O₃@SiO₂ nanocomposites. During calcination, the colour of the metal complex-containing dry gel changed from light cyan to light brown.

Heating of the dry gel to 400 °C or 500 °C resulted in the formation of Cr₂O₃ nanoparticles, giving Cr₂O₃@SiO₂ nanocomposites (denoted as Cr₂O₃@SiO₂-400(O) and Cr₂O₃@SiO₂-500(O), respectively, where the letter O indicates oxidation). In the final step, the Cr₂O₃@SiO₂ nanocomposite was reacted with ammonia at 800 °C giving CrN@SiO₂ nanocomposites (denoted as Cr₂O₃@SiO₂-400(O)-800(N) and Cr₂O₃@SiO₂-500(O)-800(N), respectively, where the letter N indicates nitridation). During nitridation the colour of the composites changed to black.

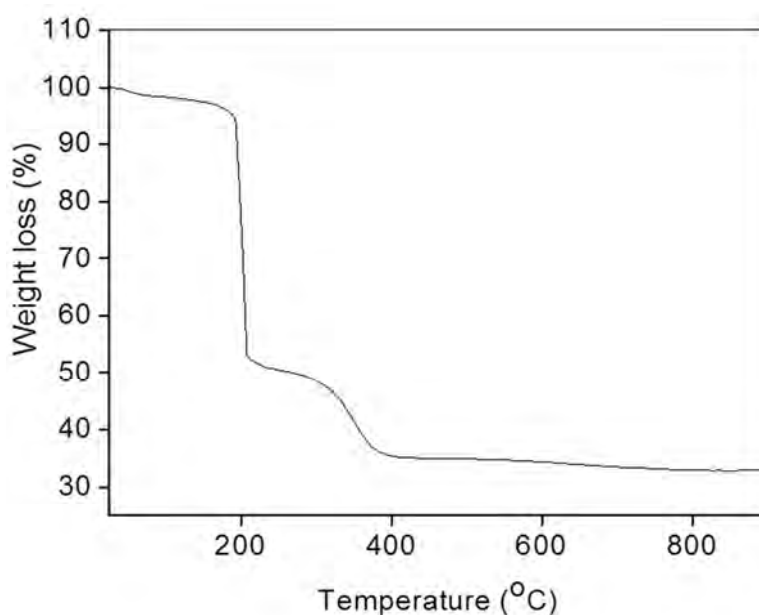


Fig. 2.13 TGA of the dried gel

The XRD patterns of the $\text{Cr}_2\text{O}_3@\text{SiO}_2$ nanocomposites are shown in Fig. 2.14A (a,b). The $\text{Cr}_2\text{O}_3@\text{SiO}_2\text{-400(O)}$ composite was amorphous, or the Cr_2O_3 nanoparticles were too small to give a XRD pattern, while $\text{Cr}_2\text{O}_3@\text{SiO}_2\text{-500(O)}$ exhibited rhombohedral Cr_2O_3 nanocrystals (JCPDS 82-1484). This observation confirms that higher temperatures during calcination step results in the formation of larger particles. After nitridation of $\text{Cr}_2\text{O}_3@\text{SiO}_2\text{-400(O)}$ and $\text{Cr}_2\text{O}_3@\text{SiO}_2\text{-500(O)}$ at 800 °C, diffraction peaks corresponding to face-centred cubic CrN (JCPDS-65-2899) (Fig. 2.14 B) were observed, indicating that Cr_2O_3 was completely transformed into CrN. $\text{Cr}_2\text{O}_3@\text{SiO}_2\text{-500(O)-800(N)}$ shows sharp reflections compared to $\text{Cr}_2\text{O}_3@\text{SiO}_2\text{-400(O)-800(N)}$ clearly indicating that the calcination temperature is important parameter for particle size. The calcination temperature must be high enough to oxidise all organic parts and should not be too high to avoid excessive growth of metal oxide particles. The average size of CrN crystallites, as determined by the Scherrer equation, is about 2.5 nm for $\text{Cr}_2\text{O}_3@\text{SiO}_2\text{-400(O)-800(N)}$ and 6 nm for $\text{Cr}_2\text{O}_3@\text{SiO}_2\text{-500(O)-800(N)}$. The average crystallite size increased as temperature during calcination process is increased from 400 to 500°C

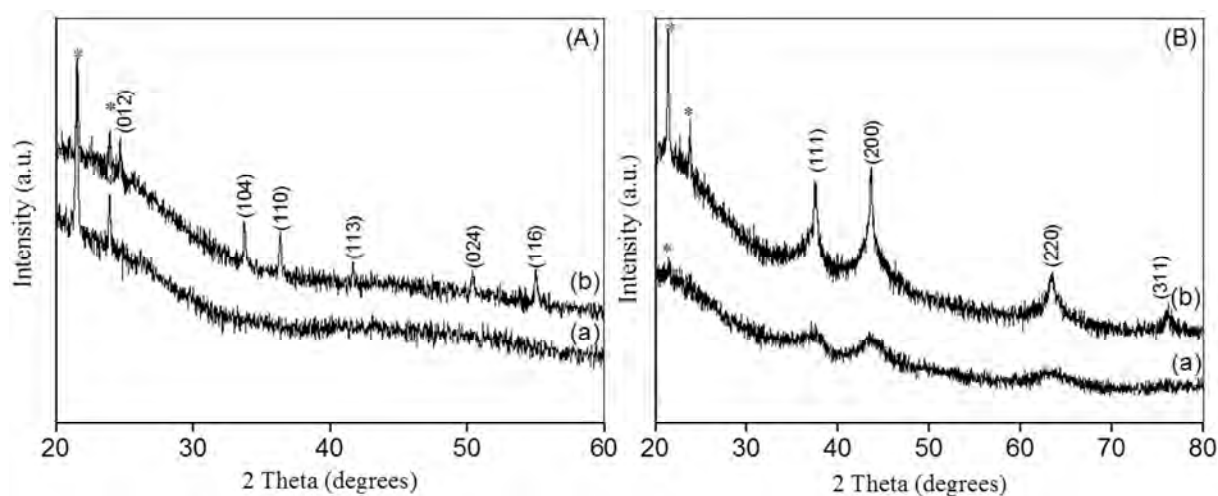


Fig. 2.14 XRD pattern of A (a) $\text{Cr}_2\text{O}_3@\text{SiO}_2\text{-400(O)}$ (b) $\text{Cr}_2\text{O}_3@\text{SiO}_2\text{-500(O)}$ and B (a) $\text{Cr}_2\text{O}_3@\text{SiO}_2\text{-400(O)-800(N)}$ (b) $\text{Cr}_2\text{O}_3@\text{SiO}_2\text{-500(O)-800(N)}$ (* cristobalite)

2.6.4 VN@SiO₂ Nanocomposite

VN synthesis was performed using vanadium chloride (VCl_3) precursor. The molar ratio of $\text{VCl}_3/\text{AEAPTS}/\text{TEOS}$ was 1/3/2. The detailed synthesis procedure is given in section 6.3.1.4. TGA of the dry gel is shown in Fig. 2.15.

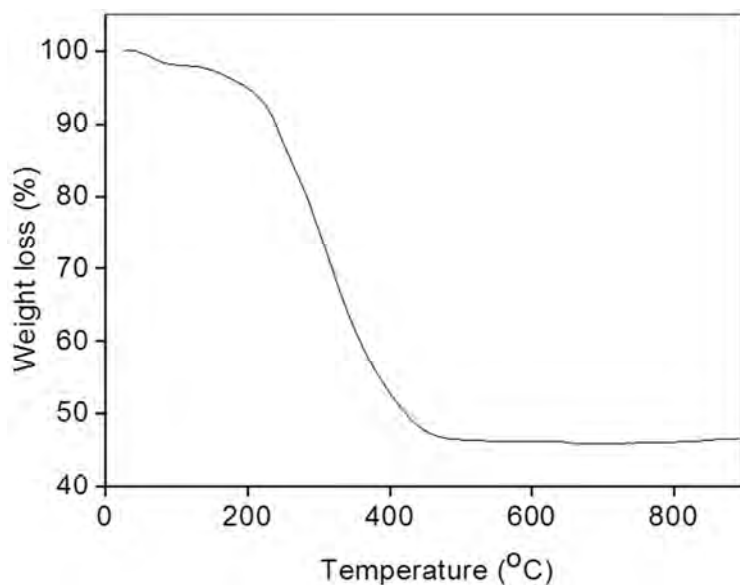


Fig. 2.15 TGA of the dried gel

The off white coloured dry gel after calcination in air at 700 °C gave yellowish-green product. The XRD analysis confirmed formation of orthorhombic $V_2O_5@SiO_2$ as shown in Fig. 2.16 (a) (JCPDS-01-0359). Nitridation of $V_2O_5@SiO_2$ at 900 °C gave a black coloured product. Fig. 2.16 (b) shows XRD corresponding to cubic VN (JCPDS -73-2038). The crystallite sizes were 29.6 and 31.1 nm for $V_2O_5@SiO_2$ and $VN@SiO_2$.

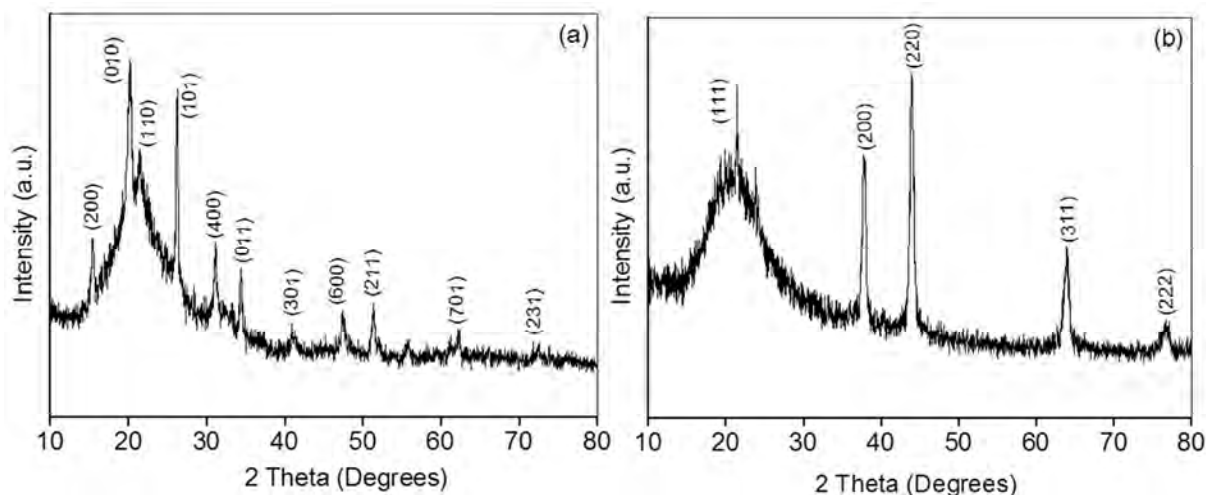


Fig. 2.16 XRD patterns of (a) $V_2O_5@SiO_2$ and (b) $VN@SiO_2$.

2.6.5 Co₂N@SiO₂ Nanocomposite

Here, CoCl₂·6H₂O was employed as a precursor. The detailed synthesis procedure is given in section 6.3.1.5. Different phases of cobalt nitride (CoN, Co₂N, Co₃N, and Co₄N) have been reported in literature³⁵. In present case only Co₂N is formed.

The TGA measurement was done prior to calcination of the dry gel as shown in Fig. 2.17. A turquoise coloured dry gel was calcined in air at 700 °C for 3 h giving the dark blue Co₃O₄@SiO₂ composite.

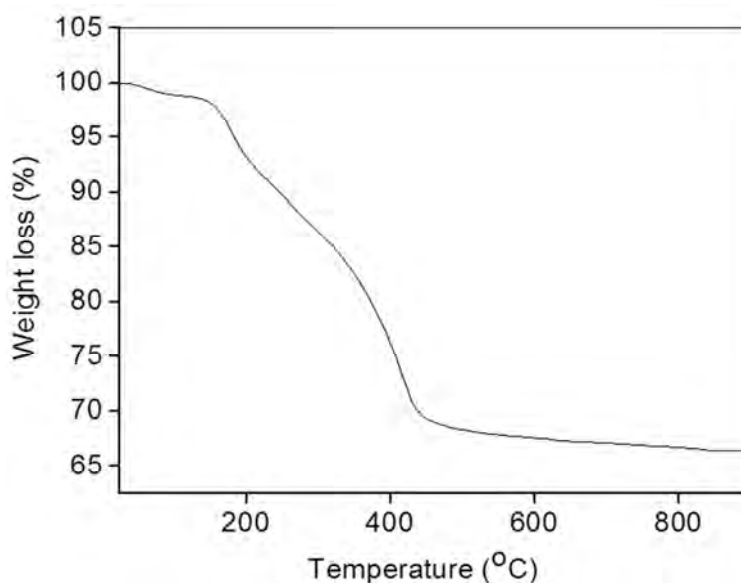


Fig. 2.17 TGA of the dried gel.

The XRD pattern of Co₃O₄@SiO₂ composite clearly shows sharp reflections belonging to cubic phase of Co₃O₄ (Fig. 2.18A (a)) (JCPDS – 43-1003). If calcination time is extended to 8 h at 700 °C then a mixture of Co₃O₄ and Co₂SiO₄ is obtained as shown in Fig. 2.18 (B). Unmarked reflections in XRD pattern belong to Co₂SiO₄. Nitridation reaction of Co₃O₄@SiO₂ at 325°C gave Co₂N@SiO₂ as confirmed by XRD (JCPDS - 72-1368) shown in Fig. 2.18A (b). The crystallite sizes were 47.3 and 43.3 nm for Co₃O₄@SiO₂ and Co₂N@SiO₂ respectively.

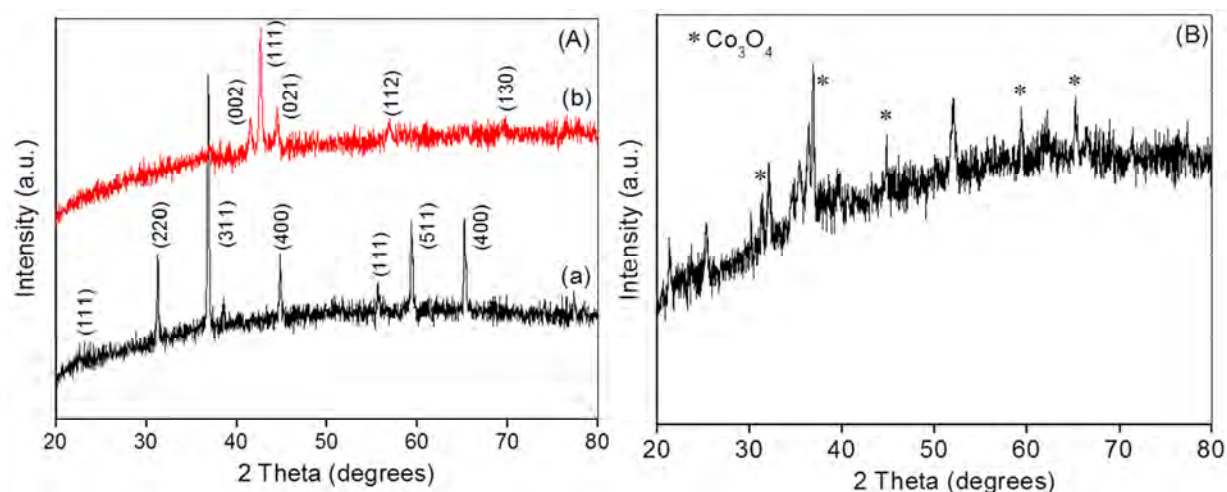


Fig. 2.18 XRD pattern of (A) (a) $\text{Co}_3\text{O}_4@\text{SiO}_2$, (b) $\text{Co}_2\text{N}@\text{SiO}_2$ and (B) dry gel calcined at $700\text{ }^\circ\text{C}$ for 8 h.

2.6.6 $\text{MN}@\text{SiO}_2$ Nanocomposites - Result Summary

Table 1 summarises the synthesis conditions as well as the structural phases observed for metal nitride@ SiO_2 composites.

Table 1

Metal precursor	Metal/ AEAPTS/ TEOS molar ratio	Calcination temperature in air($^\circ\text{C}$)/time (h)	Nitridation temperature under ammonia ($^\circ\text{C}$)/time (h)	Metal oxide@ SiO_2 Crystal structure	Metal nitride@ SiO_2 Crystal structure
$\text{Cr}(\text{NO}_3)_3 \cdot 9\text{H}_2\text{O}$	1:3:5	400/2 and 500/2	800/3	$\text{Cr}_2\text{O}_3@\text{SiO}_2$ Rhombohedral	$\text{CrN}@\text{SiO}_2$ Face-centred cubic
$\text{Ga}(\text{NO}_3)_3 \cdot x\text{H}_2\text{O}$	1:3:10	800/2	900/3	$\text{Ga}_2\text{O}_3@\text{SiO}_2$ -	$\text{GaN}@\text{SiO}_2$ Wurtzite
$\text{Cu}(\text{OAc})_2 \cdot \text{H}_2\text{O}$	1/2/12	800/1	300/8	$\text{CuO}@\text{SiO}_2$ Monoclinic	$\text{Cu}_3\text{N}@\text{SiO}_2$ Cubic
$\text{CoCl}_2 \cdot 6\text{H}_2\text{O}$	1:3:2	700/3	325/15	$\text{Co}_3\text{O}_4@\text{SiO}_2$ Cubic	$\text{Co}_2\text{N}@\text{SiO}_2$ Orthorhombic
VCl_3	1:3:2	700/3	900/6	$\text{V}_2\text{O}_5@\text{SiO}_2$ Orthorhombic	$\text{VN}@\text{SiO}_2$ Cubic

2.7 CuS@SiO₂ Nanocomposites by Sol-gel Processing Starting from Tethered Copper Complexes

The sol-gel chemistry of tethered metal complexes is a well-established route for synthesising homogeneously dispersed nanosized particles in SiO₂ matrix, leading to a great variety of metal/ metal oxide/metal alloy/metal nitride@SiO₂ nanocomposites^{87-89, 93, 101}. The high versatility suggests that this route can be extended beyond metal, metal oxides/nitrides to metal sulphides by subsequent reaction of metal oxide@SiO₂ nanocomposite with sulphur source. Covellite (CuS) was chosen as an illustrative example to extend sol-gel chemistry of tethered metal complexes to metal sulphide@SiO₂ nanocomposites by post-synthesis treatment of the copper oxide@SiO₂ nanocomposite with aq. (NH₄)₂S at room temperature. The synthesis of CuS@SiO₂ is schematically shown in Fig. 2.19.

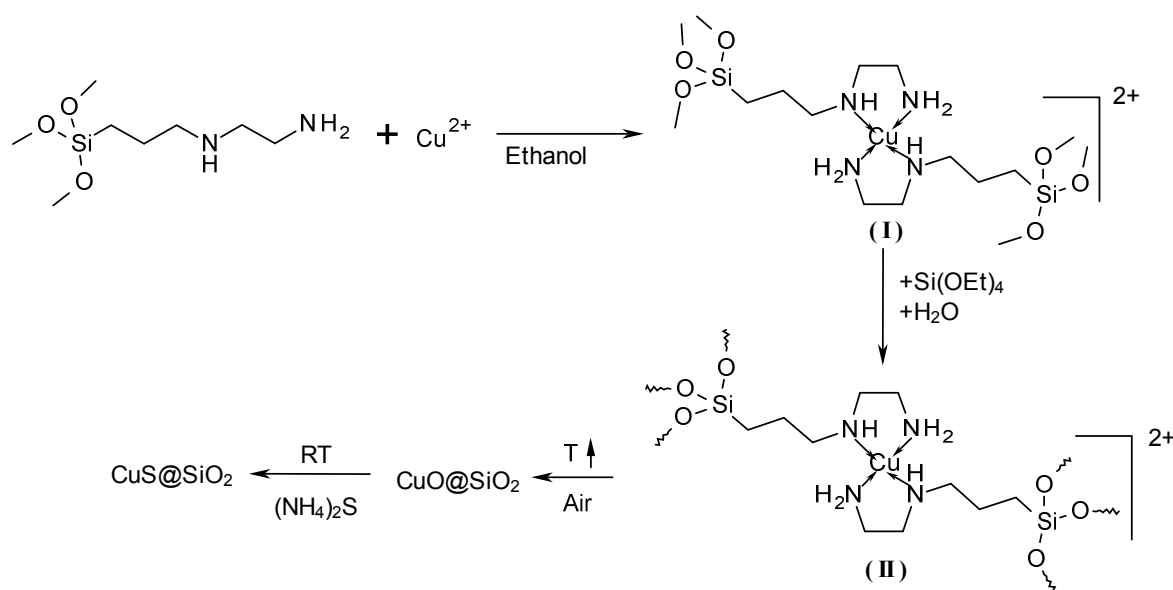


Fig. 2.19 Synthesis of the CuS@SiO₂ nanocomposite.

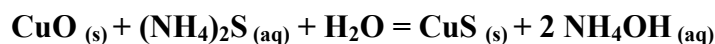
For the synthesis of CuS@SiO₂ nanocomposites four steps are necessary.

1. In situ formation of metal complexes of the type (I) upon reaction of copper salt with complexing silane (RO)₃Si(CH₂)₃A, where A=-NH-CH₂-CH₂-NH₂.
2. Sol-gel processing of in-situ formed copper complexes (I).
3. Oxidation of dry copper complex containing gels at elevated temperatures.

4. Treatment of the resulting CuO@SiO₂ nanocomposite with aqueous (NH₄)₂S at room temperature.

The first three steps for the synthesis of the CuS@SiO₂ nanocomposite are similar to CuO@SiO₂ nanocomposite formation (as described in section 2.6.1). In the last step the CuO@SiO₂ nanocomposite was used as a precursor to synthesize CuS@SiO₂ nanocomposite. Aqueous (NH₄)₂S solution in a stoichiometric amount was added into an aqueous suspension of the CuO@SiO₂ nanocomposite with stirring. The colour of the reaction solution changed to green immediately after addition of (NH₄)₂S. The suspension resulted in a green coloured powder after centrifugation, washing and drying process. The detailed experimental procedure is given in section 6.3.1.6.

The formation of CuS nanoparticles in a silica matrix in aqueous medium is described in the following equation. The O²⁻ from CuO is replaced by S²⁻ from (NH₄)₂S.



The formation of the CuS@SiO₂ nanocomposite was confirmed by XRD studies. Phase pure CuS (Covellite) is obtained in the present case (JCPDS 06-0464) excluding other copper sulphide phases (Fig. 2.20). A broad peak at < 30 degrees is from amorphous silica. After treatment with (NH₄)₂S for 6 h no CuO was left according to XRD. The average sizes of the CuO and CuS particles, calculated by the Scherrer equation, were 11 and 15 nm, respectively.

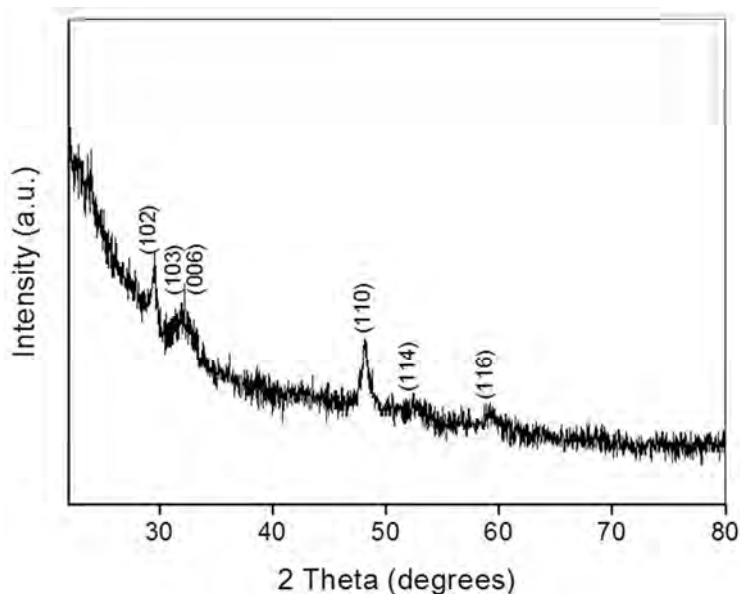


Fig. 2.20 XRD pattern of the CuS@SiO₂ nanocomposite.

The STEM image of the CuS@SiO₂ nanocomposite is shown in Fig. 2.21 (a) and an EDX scan over a single CuS nanoparticle (bright spot) in Fig. 2.21 (b). The EDX spectrum confirms the presence of Cu, S, Si and O.

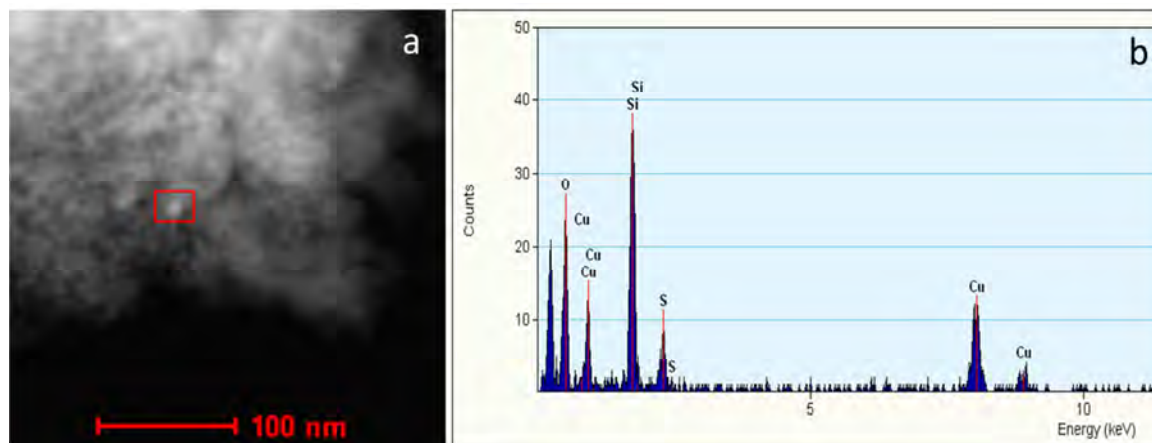


Fig. 2.21 STEM image (a) and (b) EDX scan profile of single CuS nanoparticle from CuS@SiO₂ nanocomposite.

The TEM image (Fig. 2.22) of the CuS@SiO₂ nanocomposite shows finely distributed CuS nanoparticles in the SiO₂ matrix. Thus the sol-gel processing of tethered metal complexes strategy is successfully applied for the formation of CuS@SiO₂ nanocomposite.

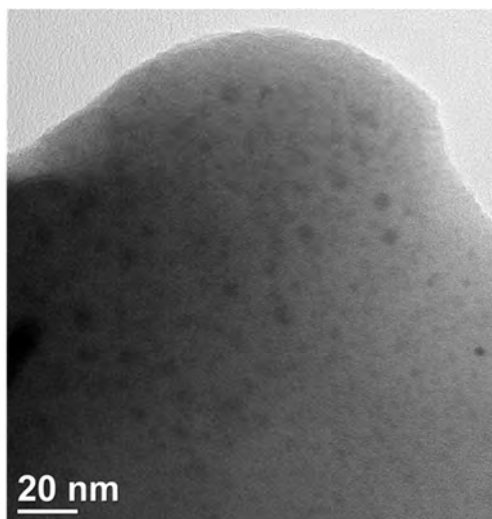


Fig. 2.22 TEM image of CuS@SiO₂ nanocomposite

2.7 Conclusion

In conclusion a simple method has been explored for the preparation of MN@SiO₂ nanocomposites (MN = Cu₃N, GaN, CrN, Co₂N, VN) and also CuS@SiO₂ nanocomposite. This method takes advantage of the combination of an organometallic approach for the synthesis of metal complexes and a sol-gel method for the formation of the silica matrix. The key point of this work is the use of a tether of the type (RO)₃Si-(CH₂)₃-X, where X = -NH-CH₂-CH₂-NH₂ is a coordinating group. The groups X allow tethering of metal ions to the silicate network during sol-gel processing due to the intermediate formation of complexes (RO)₃Si(CH₂)₃-X-M, where M is a metal ion. A two component system is transformed into a single-source precursor. Thus, a high dispersion of the metal precursor during sol-gel processing is obtained. The proportion of metal in final composite materials is easily controlled by using TEOS as silica source during sol-gel processing. A controlled thermal treatment to dry gel results in the degradation of the organic groups and simultaneous formation of metal oxide nanoparticles in the silica matrix. Subsequent, reaction of the metal oxide@SiO₂ nanocomposites under ammonia atmosphere at higher temperature gave metal nitride@SiO₂ nanocomposites with relatively high metal nitride content. Additionally, sulphidation reaction of copper oxide@SiO₂ nanocomposite in aqueous (NH₄)₂S allowed synthesis of a CuS@SiO₂ nanocomposite. The obtained hybrid materials showed a homogeneous dispersion of the size-controlled metal nitride and CuS nanoparticles. Thus, the use of organo-functionalized silica precursors appears to be a favourable and simple way to achieve size-controlled and well-dispersed metal nitride as well as metal sulphide nanoparticles exclusively within the silica host matrix.

2.8 References

1. You, T. Y.; Niwa, O.; Tomita, M.; Hirono, S. *Analytical Chemistry* **2003**, 75, (9), 2080-2085.
2. Liu, H. Y.; Ma, D.; Blackley, R. A.; Zhou, W. Z.; Bao, X. H. *Chemical Communications* **2008**, (23), 2677-2679.
3. Lee, J. E.; Lee, N.; Kim, T.; Kim, J.; Hyeon, T. *Accounts of Chemical Research* **2011**, 44, (10), 893-902.
4. Wang, Q.; Zhu, L. *Journal of Polymer Science Part B: Polymer Physics* **2011**, 49, (20), 1421-1429.
5. Yi, D. K.; Lee, S. S.; Ying, J. Y. *Chemistry of Materials* **2006**, 18, (10), 2459-2461.
6. Li, J. J.; Claude, J.; Norena-Franco, L. E.; Il Seok, S.; Wang, Q. *Chemistry of Materials* **2008**, 20, (20), 6304-6306.
7. Sperling, R. A.; Rivera Gil, P.; Zhang, F.; Zanella, M.; Parak, W. J. *Chemical Society reviews* **2008**, 37, (9), 1896-908.
8. Ho, D.; Sun, X. L.; Sun, S. H. *Accounts of Chemical Research* **2011**, 44, (10), 875-882.
9. González-Gálvez, D.; Nolis, P.; Philippot, K.; Chaudret, B.; van Leeuwen, P. W. N. M. *ACS Catalysis* **2012**, 2, (3), 317-321.
10. Ow, H.; Larson, D. R.; Srivastava, M.; Baird, B. A.; Webb, W. W.; Wiesner, U. *Nano letters* **2005**, 5, (1), 113-117.
11. Sun, Y. M.; Hu, X. L.; Luo, W.; Huang, Y. H. *Journal of Materials Chemistry* **2012**, 22, (2), 425-431.
12. Garcia-Martinez, J.; Linares, N.; Sinibaldi, S.; Coronado, E.; Ribera, A. *Microporous and Mesoporous Materials* **2009**, 117, (1-2), 170-177.
13. Li, S.; Meng Lin, M.; Toprak, M. S.; Kim do, K.; Muhammed, M. *Nano Reviews* **2010**, 1.
14. Park, J. N.; Forman, A. J.; Tang, W.; Cheng, J. H.; Hu, Y. S.; Lin, H. F.; McFarland, E. W. *Small* **2008**, 4, (10), 1694-1697.
15. Matura, V.; Guari, Y.; Reye, C.; Corriu, R. J. P.; Tristany, M.; Jansat, S.; Philippot, K.; Maisonnat, A.; Chaudret, B. *Advanced Functional Materials* **2009**, 19, (23), 3781-3787.
16. Maruyama, T.; Morishita, T. *Applied Physics Letters* **1996**, 69, (7), 890-891.
17. Wang, J.; Chen, J. T.; Yuan, X. M.; Wu, Z. G.; Miao, B. B.; Yan, P. X. *Journal of Crystal Growth* **2006**, 286, (2), 407-412.

18. Du, Y.; Ji, A. L.; Ma, L. B.; Wang, Y. Q.; Cao, Z. X. *Journal of Crystal Growth* **2005**, 280, (3-4), 490-494.
19. Wang, T.; Pan, X. J.; Wang, X. M.; Duan, H. G.; Li, R. S.; Li, H.; Xie, E. Q. *Applied Surface Science* **2008**, 254, (21), 6817-6819.
20. Guillaume, C.; Serghiou, G.; Morniroli, J. P.; Frost, D. J. *Joint 21st Airapt and 45th Ehprg International Conference on High Pressure Science and Technology* **2008**, 121.
21. Ji, A.; Li, C.; Du, Y.; Ma, L.; Song, R.; Huang, R.; Cao, Z. *Nanotechnology* **2005**, 16, (10), 2092-2095.
22. Yuan, X. M.; Yan, P. X.; Liu, J. Z. *Materials Letters* **2006**, 60, (15), 1809-1812.
23. Lu, Q. A.; Zhang, X.; Zhu, W.; Zhou, Y. N.; Zhou, Q. F.; Liu, L. L.; Wu, X. J. *Physica Status Solidi a-Applications and Materials Science* **2011**, 208, (4), 874-877.
24. Borsa, D. M.; Grachev, S.; Presura, C.; Boerma, D. O. *Applied Physics Letters* **2002**, 80, (10), 1823-1825.
25. Nosaka, T.; Yoshitake, M.; Okamoto, A.; Ogawa, S.; Nakayama, Y. *Thin Solid Films* **1999**, 348, (1-2), 8-13.
26. Lee, B. S.; Yi, M.; Chu, S. Y.; Lee, J. Y.; Kwon, H. R.; Lee, K. R.; Kang, D.; Kim, W. S.; Bin Lim, H.; Lee, J.; Youn, H. J.; Chi, D. Y.; Hur, N. H. *Chemical Communications* **2010**, 46, (22), 3935-3937.
27. Koester, R.; Hwang, J. S.; Salomon, D.; Chen, X. J.; Bougerol, C.; Barnes, J. P.; Dang, D. L.; Rigutti, L.; Bugallo, A. D.; Jacopin, G.; Tchernycheva, M.; Durand, C.; Eymery, J. *Nano Letters* **2011**, 11, (11), 4839-4845.
28. Subramania, G.; Li, Q. M.; Lee, Y. J.; Figiel, J. J.; Wang, G. T.; Fischer, A. J. *Nano Letters* **2011**, 11, (11), 4591-4596.
29. Schwenzler, B.; Hu, J.; Morse, D. E. *Advanced Materials* **2011**, 23, (20), 2278-2283.
30. Dong, Y. J.; Tian, B. Z.; Kempa, T. J.; Lieber, C. M. *Nano letters* **2009**, 9, (5), 2183-2187.
31. Wu, H.; Sun, Y.; Lin, D.; Zhang, R.; Zhang, C.; Pan, W. *Advanced materials* **2009**, 21, (2), 227-231.
32. Sun, X. M.; Li, Y. D. *Angewandte Chemie-International Edition* **2004**, 43, (29), 3827-3831.
33. Bouguerra, M.; Belkhir, M. A.; Chateigner, D.; Samah, M.; Gerbous, L.; Nouet, G. *Physica E: Low-dimensional Systems and Nanostructures* **2008**, 41, (2), 292-298.
34. Sinha, G.; Panda, S. K.; Mishra, P.; Ganguli, D.; Chaudhuri, S. *Journal of Physics: Condensed Matter* **2007**, 19, (34), 346209.

35. Wang, X.; Jia, H.; Zheng, W. T.; Chen, Y.; Feng, S. *Thin Solid Films* **2009**, 517, (15), 4419-4424.
36. Shi, Y. F.; Wan, Y.; Zhang, R. Y.; Zhao, D. Y. *Advanced Functional Materials* **2008**, 18, (16), 2436-2443.
37. Yao, Z.; Zhu, A.; Au, C. T.; Shi, C. *Catalysis Letters* **2009**, 130, (1-2), 63-71.
38. Hahn, U.; Weber, W. *Physical Review B* **1996**, 53, (19), 12684-12693.
39. Tricoteaux, A.; Jouan, P. Y.; Guerin, J. D.; Martinez, J.; Djouadi, A. *Surface & Coatings Technology* **2003**, 174, 440-443.
40. Han, S.; Lin, J. H.; Wang, D. Y.; Lu, F. H.; Shih, H. C. *Journal of Vacuum Science & Technology a-Vacuum Surfaces and Films* **2001**, 19, (4), 1442-1446.
41. Chen, J. S.; Duh, J. G.; Wu, F. B. *Surface & Coatings Technology* **2002**, 150, (2-3), 239-245.
42. Scheerer, H.; Hoche, H.; Broszeit, E.; Berger, C. *Surface & Coatings Technology* **2001**, 142, 1017-1022.
43. Glushenkov, A. M.; Hulicova-Jurcakova, D.; Llewellyn, D.; Lu, G. Q.; Chen, Y. *Chemistry of Materials* **2010**, 22, (3), 914-921.
44. Ghimbeu, C. M.; Raymundo-Pinero, E.; Fioux, P.; Beguin, F.; Vix-Guterl, C. *Journal of Materials Chemistry* **2011**, 21, (35), 13268-13275.
45. Kwon, H.; Choi, S.; Thompson, L. T. *Journal of Catalysis* **1999**, 184, (1), 236-246.
46. Song, B.; Chen, X. L.; Han, J. C.; Jian, J. K.; Wang, W. Y.; Zuo, H. B.; Zhang, X. H.; Meng, S. H. *Inorganic Chemistry* **2009**, 48, (22), 10519-10527.
47. Li, J. G.; Gao, L.; Sun, J.; Zhang, Q. H.; Guo, J. K.; Yan, D. S. *Journal of the American Ceramic Society* **2001**, 84, (12), 3045-3047.
48. Li, Y.; Gao, L.; Li, J.; Yan, D. *Journal of the American Ceramic Society* **2002**, 85, (5), 1294-1296.
49. Gao, L.; Zhang, Q.; Li, J. *Journal of Materials Chemistry* **2003**, 13, (1), 154-158.
50. Zhang, Q. H.; Gao, L. *Langmuir* **2004**, 20, (22), 9821-9827.
51. Zhang, Q.; Gao, L. *Journal of the American Ceramic Society* **2006**, 89, (2), 415-421.
52. Aghababazadeh, R.; Mirhabibi, A. R.; Rand, B.; Banijamali, S.; Pourasad, J.; Ghahari, M. *Surface Science* **2007**, 601, (13), 2881-2885.
53. Schmid, G. *Journal of Materials Chemistry* **2002**, 12, (5), 1231-1238.
54. Hu, J. Q.; Bando, Y.; Golberg, D.; Liu, Q. L. *Angewandte Chemie-International Edition* **2003**, 42, (30), 3493-3497.

55. Buha, J.; Djerdj, I.; Antonietti, M.; Niederberger, M. *Chemistry of Materials* **2007**, 19, (14), 3499-3505.
56. Qin, M. L.; Du, X. L.; Li, Z. X.; Humail, I. S.; Qu, X. H. *Materials Research Bulletin* **2008**, 43, (11), 2954-2960.
57. Chirico, P.; Hector, A. L.; Mazumder, B. *Dalton transactions* **2010**, 39, (26), 6092-6097.
58. Fischer, R. A.; Miehr, A.; Herdtweck, E.; Mattner, M. R.; Ambacher, O.; Metzger, T.; Born, E.; Weinkauff, S.; Pulham, C. R.; Parsons, S. *Chemistry-a European Journal* **1996**, 2, (11), 1353-1358.
59. Wu, Y.; Wadia, C.; Ma, W. L.; Sadtler, B.; Alivisatos, A. P. *Nano letters* **2008**, 8, (8), 2551-2555.
60. Bierman, M. J.; Jin, S. *Energy & Environmental Science* **2009**, 2, (10), 1050-1059.
61. Li, T. L.; Lee, Y. L.; Teng, H. S. *Journal of Materials Chemistry* **2011**, 21, (13), 5089-5098.
62. Wu, B.; Song, H. H.; Zhou, J. S.; Chen, X. H. *Chemical Communications* **2011**, 47, (30), 8653-8655.
63. Ge, Z. H.; Zhang, B. P.; Chen, Y. X.; Yu, Z. X.; Liu, Y.; Li, J. F. *Chemical Communications* **2011**, 47, (47), 12697-12699.
64. Dowland, S.; Lutz, T.; Ward, A.; King, S. P.; Sudlow, A.; Hill, M. S.; Molloy, K. C.; Haque, S. A. *Advanced Materials* **2011**, 23, (24), 2739-2744.
65. Kim, C. S.; Kim, M.; Larrabee, D. C.; Vurgaftman, I.; Meyer, J. R.; Lee, S. H.; Kafafi, Z. H. *Journal of Applied Physics* **2009**, 106, (11), 113105.
66. Zhu, N.; Zhang, A.; Wang, Q.; He, P.; Fang, Y. *Electroanalysis* **2004**, 16, (7), 577-582.
67. Vorontsov, V.; Luo, J. L.; Sanger, A. R.; Chuang, K. T. *Journal of Power Sources* **2008**, 183, (1), 76-83.
68. Klimov, V.; Haring Bolivar, P.; Kurz, H.; Karavanskii, V.; Krasovskii, V.; Korkishko, Y. *Applied Physics Letters* **1995**, 67, (5), 653.
69. Klimov, V. I.; Karavanskii, V. A. *Physical Review B* **1996**, 54, (11), 8087-8094.
70. Raevskaya, A. E.; Stroyuk, A. L.; Kuchmii, S. Y.; Kryukov, A. I. *Journal of Molecular Catalysis A: Chemical* **2004**, 212, (1-2), 259-265.
71. Chung, J. S.; Sohn, H. J. *Journal of Power Sources* **2002**, 108, (1-2), 226-231.
72. Yu, X. L.; Cao, C. B.; Zhu, H. S.; Li, Q. S.; Liu, C. L.; Gong, Q. H. *Advanced Functional Materials* **2007**, 17, (8), 1397-1401.

73. Roy, P.; Srivastava, S. K. *Crystal Growth & Design* **2006**, 6, (8), 1921-1926.
74. Ge, J. P.; Wang, J.; Zhang, H. X.; Li, Y. D. *Chemistry-a European Journal* **2004**, 10, (14), 3525-3530.
75. Gu, F.; Li, C. Z.; Wang, S. F.; Lu, M. K. *Langmuir* **2006**, 22, (3), 1329-1332.
76. Feldman, Y.; Frey, G. L.; Homyonfer, M.; Lyakhovitskaya, V.; Margulis, L.; Cohen, H.; Hodes, G.; Hutchison, J. L.; Tenne, R. *Journal of the American Ceramic Society* **1996**, 118, (23), 5362-5367.
77. Elizondo-Villarreal, N.; Velázquez-Castillo, R.; Galván, D. H.; Camacho, A.; José Yacamán, M. *Applied Catalysis A: General* **2007**, 328, (1), 88-97.
78. Panda, S. K.; Dev, A.; Chaudhuri, S. *Journal of Physical Chemistry C* **2007**, 111, (13), 5039-5043.
79. Li, Q.; Newberg, J. T.; Walter, E. C.; Hemminger, J. C.; Penner, R. M. *Nano letters* **2004**, 4, (2), 277-281.
80. Camacho-Bragado, G. A.; Jose-Yacaman, M. *Applied Physics A* **2005**, 82, (1), 19-22.
81. Hu, W.; Zhao, Y.; Liu, Z.; Zhu, Y. *Nanotechnology* **2007**, 18, (9), 095605.
82. Zhang, H.; Yang, D.; Ma, X.; Que, D. *Nanotechnology* **2005**, 16, (11), 2721-2725.
83. Shao, H.-F.; Qian, X.-F.; Zhu, Z.-K. *Journal of Solid State Chemistry* **2005**, 178, (11), 3522-3528.
84. Cao, H. L.; Qian, X. F.; Wang, C.; Ma, X. D.; Yin, J.; Zhu, Z. K. *Journal of the American Ceramic Society* **2005**, 127, (46), 16024-16025.
85. Zhang, Y. C.; Qiao, T.; Ya Hu, X. *Journal of Crystal Growth* **2004**, 268, (1-2), 64-70.
86. Pang, M. L.; Zeng, H. C. *Langmuir* **2010**, 26, (8), 5963-5970.
87. Morke, W.; Lamber, R.; Schubert, U.; Breitscheidel, B. *Chemistry of Materials* **1994**, 6, (10), 1659-1666.
88. Trimmel, G.; Lembacher, C.; Kickelbick, G.; Schubert, U. *New Journal of Chemistry* **2002**, 26, (6), 759-765.
89. Breitscheidel, B.; Zieder, J.; Schubert, U. *Chemistry of Materials* **1991**, 3, (3), 559-566.
90. Schubert, U.; Tewinkel, S.; Lamber, R. *Chemistry of Materials* **1996**, 8, (8), 2047-2055.
91. Schubert, U. *Polymer International* **2009**, 58, (3), 317-322.
92. Trimmel, G.; Schubert, U. *Journal of Non-Crystalline Solids* **2001**, 296, (3), 188-200.
93. Schubert, U. *Advanced Engineering Materials* **2004**, 6, (3), 173-176.

94. Martinez, S.; Moreno-Manas, M.; Vallribera, A.; Schubert, U.; Roig, A.; Molins, E. *New Journal of Chemistry* **2006**, 30, (7), 1093-1097.
95. Lembacher, C.; Schubert, U. *New Journal of Chemistry* **1998**, 22, (7), 721-724.
96. Duan, C. G.; Sabiryanov, R. F.; Liu, J. J.; Mei, W. N.; Dowben, P. A.; Hardy, J. R. *Physical Review Letters* **2005**, 94, (23).
97. Fischer, A.; Makowski, P.; Mueller, J. O.; Antonietti, M.; Thomas, A.; Goettmann, F. *Chemosuschem* **2008**, 1, (5), 444-449.
98. Ponce, F. A.; Bour, D. P. *Nature* **1997**, 386, (6623), 351-359.
99. Nyk, M.; Jabłoński, J. M.; Stręk, W.; Misiewicz, J. *Optical Materials* **2004**, 26, (2), 133-136.
100. Zeng, X. T. *Surface and Coatings Technology* **1999**, 113, (1-2), 75-79.
101. Deshmukh, R.; Schubert, U. *Journal of Materials Chemistry* **2011**, 21, (46), 18534-18536.

Chapter 3

Functional Nanoparticles (CuO and Cu₃N) within Hollow Mesoporous Silica Capsules

Considerable efforts have been devoted in past few decades towards the fabrication of nanomaterials with well-defined morphologies for specific applications¹⁻³. The preparation of hollow inorganic capsules of defined structure and composition with functionalised interior is of immense scientific and technological interest⁴⁻⁷. The hollow nanostructures with functionalised inner core have been found to have diverse and fascinating applications in catalysis, drug delivery, lithium-ion batteries and biosensors^{8, 9}. Hollow nanostructures with functionalised inner core possess many unique and interesting properties such as low density, void space between the core and the shell, and ready tailorability and functionality of both the cores and shells^{2, 9, 10}. In view of these advantages, many attempts have been made to synthesize hollow particles with functionalised interior¹¹⁻¹⁴.

The synthesis of hollow particles through a sacrificial core template is a commonly used methodology. Generally, templates like silica spheres, carbon spheres, polystyrene spheres etc. are employed¹⁵⁻¹⁷. The structure of the hollow product obtained by using a sacrificial template has well-defined and monodisperse morphology^{18, 19}. Uniform carbon spheres synthesized by hydrothermal carbonisation of polysaccharides have been employed successfully as sacrificial template for the synthesis of various types of hollow/core shell nanostructures²⁰⁻²⁵.

A schematic growth model for carbon spheres is shown in Fig. 3.1.²⁶ According to the literature, the transformation of glucose molecules into carbon spheres involves several processes, such as dehydration, polymerization, and carbonization²⁶. First of all, the intermolecular dehydration between glucose molecules occurs under hydrothermal conditions. This process continues, leading to formation of oligosaccharides denoted as polymerization. When the solution reached a critical supersaturation, a short single burst of nuclei resulted. This carbonization step may arise from cross-linking induced by intermolecular dehydration of linear or branchlike oligosaccharides, or other macromolecules formed in the prior step. The resulting nuclei then grew uniformly and isotropically by diffusion of solutes toward the particle surfaces until the final size was attained.

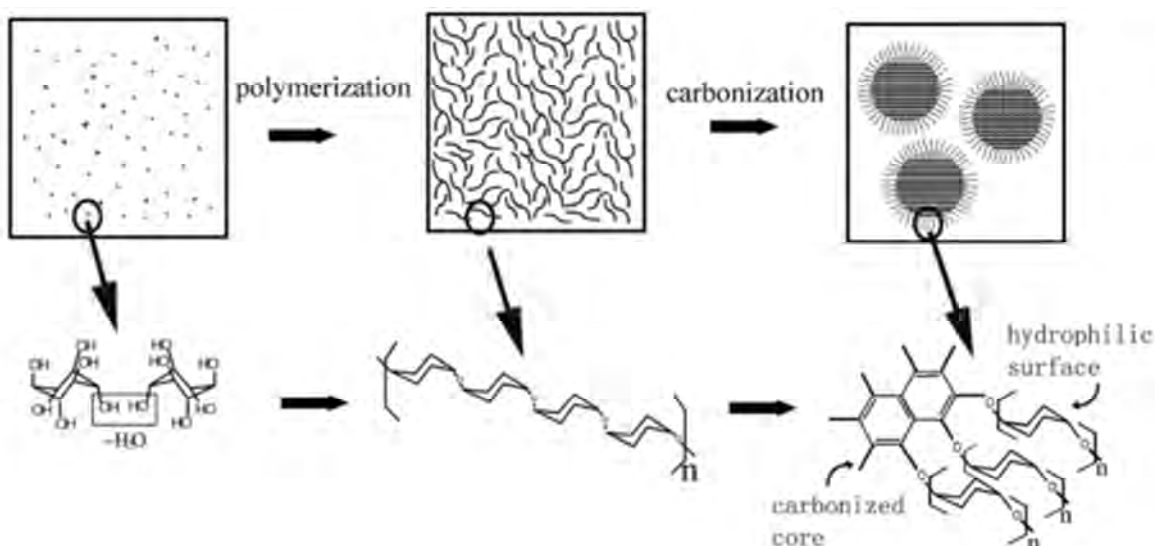


Fig. 3.1 Schematic growth model for synthesis of carbon spheres via dehydration and aromatization of glucose under hydrothermal conditions.

Such carbon sphere obtained by the hydrothermal carbonisation process have many important features such as: (1) tunable and uniform sizes of 150-1500 nm, (2) hydrophilic and reactive surfaces due to the existence of functional groups like -OH, -CHO, and -COOH, and (3) porous microstructures²⁶. Carbon spheres have shown an amazing ability to encapsulate noble metal nanoparticles to form carbon-metal core-shell nanostructures²⁷. Silver nanoparticles with tunable sizes were encapsulated in a carbonaceous shell through a wet chemical route - the catalysed dehydration of glucose under hydrothermal condition²⁸ (Fig. 3.2). Here glucose was used as the reducing agent to react with silver ions, and it also served as the source of carbonaceous shells.

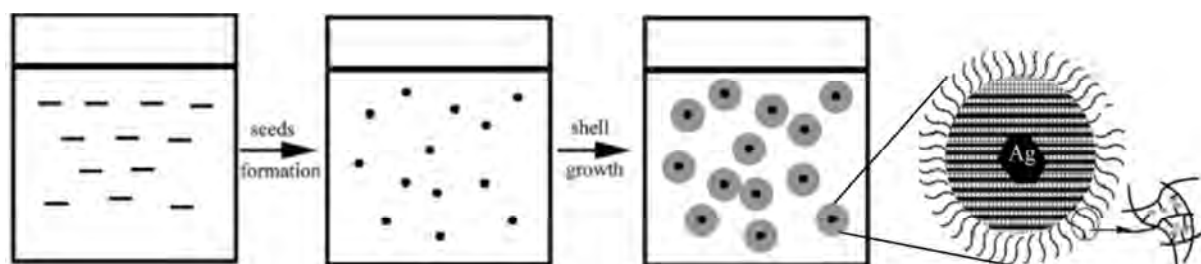


Fig. 3.2 The schematic illustration on formation mechanism of Ag@C core/shell structured nanospheres.

Besides their amazing encapsulation abilities in forming various carbon-metal core-shell nanostructures, these carbon microspheres have been evidenced as effective hard templates in producing uniform oxide or nitride hollow microspheres (Fig. 3.3),²⁵ due to their uniform sizes and outer reactive surface. There is no need to perform an additional surface

modification process when using these carbon spheres as templates because of their affluent functional groups on the surface.

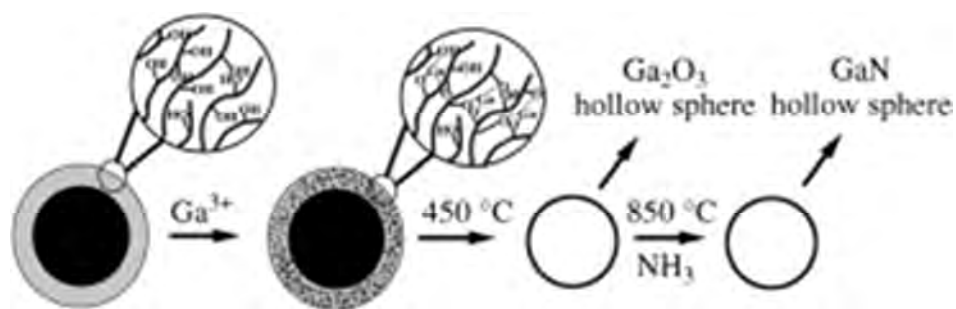


Fig. 3.3. Schematic mechanism for the formation of GaN hollow spheres using carbon spheres as templates.

Carbon spheres were also used as template for the fabrication of composite nanoreactors²⁰. Pd nanoparticles were anchored through residual hydroxyl groups on the surfaces of the carbon nanospheres. By using sol-gel processing, followed by a calcination step, a nanoreactor with Pd nanoparticles inside the hollow mesoporous silica spheres was obtained (Fig. 3.4).

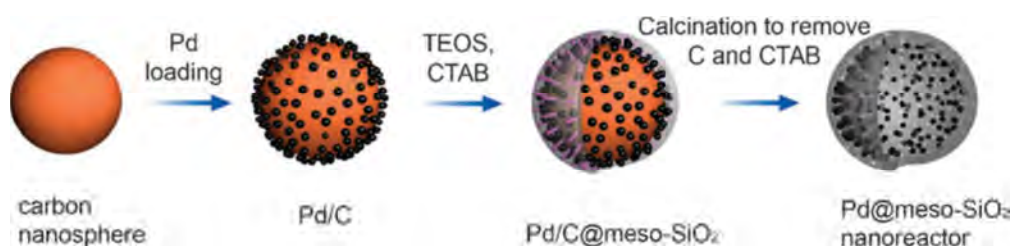


Fig. 3.4 Synthesis route to the composite nanoreactor.

Furthermore CdS nanoparticles were coated on the surface of colloidal carbon spheres using a microwave-assisted method²⁹ (Fig. 3.5).

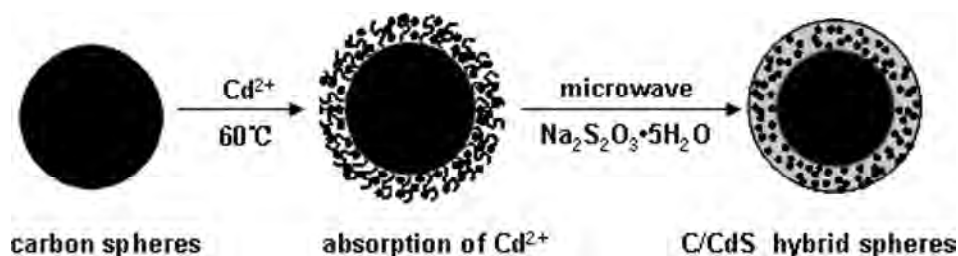


Fig. 3.5 Schematic illustration of the coating of CdS nanoparticles on colloidal carbon spheres.

Rattle-type $\text{Fe}_3\text{O}_4@\text{SiO}_2$ hollow mesoporous spheres with large cavities were synthesized by using colloidal carbon spheres to which an iron source was adsorbed²¹. The synthesis procedure is schematically shown in Fig. 3.6.

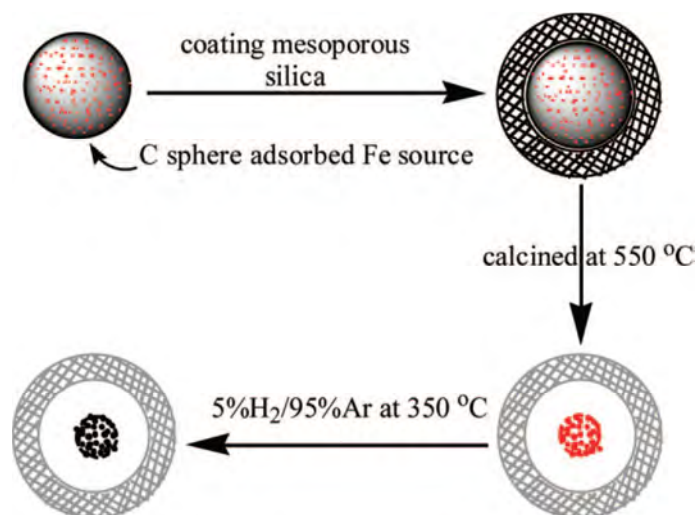


Fig. 3.6 Procedure for the preparation of rattle-type $\text{Fe}_3\text{O}_4@\text{SiO}_2$ hollow mesoporous spheres.

Additionally, highly dispersed Pd nanoparticles with small diameter were successfully prepared on the surface of carbon spheres through an in situ reduction process³⁰ (Fig. 3.7 (a)). A microwave assisted synthesis of carbon spheres with Ag nanoparticles (Ag-NP/C composites) was performed by using aqueous $[\text{Ag}(\text{NH}_3)_2]^+$ and PVP as reducing agent³¹ (Fig. 3.7 (b)).

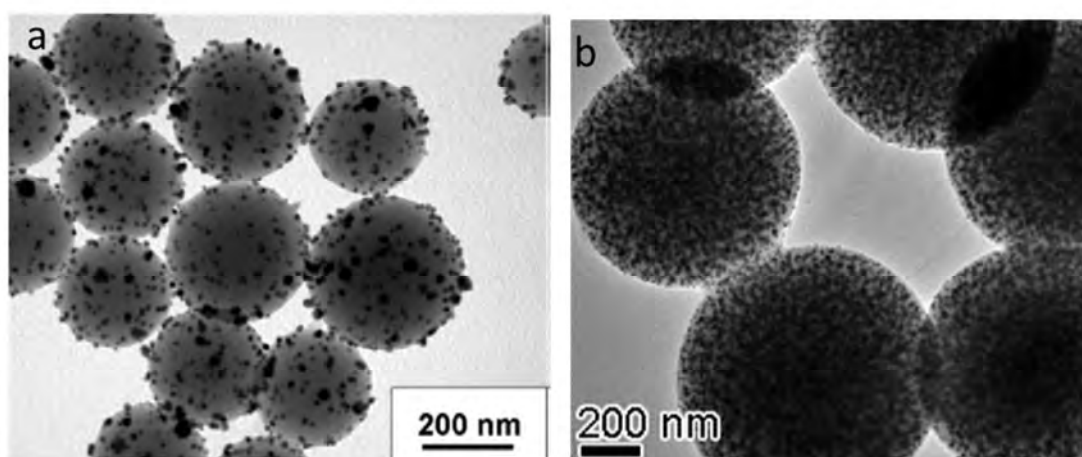


Fig. 3.7 (a) Pd nanoparticles on carbon surface and (b) Ag-nanoparticle/C composite

It is evidenced that the carbon spheres serve as potential host as well as template material for creating various hollow/spherical nanostructures.

Hollow spheres with a mesoporous shell allows the possibility of encapsulating a variety of substances like drugs, catalysts etc. within their core^{10, 32, 33}. The mesoporous capsules are promising because of their unique features such as high surface area, large void volume suitable for selectively encapsulating molecules, protecting the encapsulated particles in the core from the surrounding environment and the ordered mesopores providing a fast diffusion path to the cores³⁴⁻³⁷. Several methods were described to fabricate hollow capsules with various types of shells^{3, 8, 38}.

Mesoporous silica capsules are of importance because of their high surface area, tunable pore size, chemical inertness and thermal/mechanical stability which make them attractive for drug delivery, heterogeneous catalysis, nanoreactors³⁹⁻⁴¹. There are reports which describe encapsulation of nanoparticles within mesoporous silica hollow spheres to fabricate functional composite materials⁴²⁻⁴⁴.

Nanoparticles hold great promise as robust heterogeneous catalysts due to their high surface area and the presence of quantum confinement effects, which makes them highly active and selective catalyst compared to bulk particles⁴⁵⁻⁴⁷. However nanoparticles tend to agglomerate to minimise their surface energy which reduces the catalytic activity. The catalyst encapsulation in a thermally stable and chemically inert porous oxide shell has proved to be important for efficient catalytic activity, recyclability and facile separation of products⁴⁸⁻⁵¹. Recently several attempts have been made towards synthesis of heterogeneous nanoreactors, where metal/metal oxide nanoparticles are encapsulated inside an inert porous oxide shells⁵²⁻⁵⁵. The porous structure of the outer shell provides channels for the reactant to reach the active surface of the catalyst. For example, Song and co-workers prepared an excellent nano-reactor, that was composed of hollow spheres of mesoporous silica with Pd nanoparticles residing inside the spheres, for coupling of aryl iodides with phenylboronic acids²⁰. Anisur and co-workers fabricated hollow porous silica particles with functionalised interior surface of a catalytically active MnO₂ layer for cyanosilylation reactions⁵⁶. Sanles-Sobrido et al. reported the synthesis of highly active nanoreactors based on the encapsulation of dendritic Pt nanoparticles inside hollow porous silica capsules⁵⁷. Park et al. synthesized a Ni@SiO₂ yolk-shell nanoreactor framework comprising Ni cores inside hollow silica shells. This system was employed as a model catalyst for steam methane reforming and also for heterogeneous hydrogen-transfer reactions of acetophenone⁵⁸. In addition to the given examples there are additional examples for the synthesis of active and selective catalysts based on hollow mesoporous particles with functionalised inner core^{59, 60}.

In particular, for further development of heterogeneous nanoreactors it is important to design simple and new methods for internal surface functionalization of porous hollow shells by highly active heterogeneous catalysts, which will allow chemical reactions to occur within the hollow shell. CuO is an important functional material having exciting applications in catalysis, gas sensors, lithium-ion battery material and photovoltaic cells. Various CuO/SiO₂ composite materials have been synthesized to explore their properties for heterogeneous catalytic applications⁶¹⁻⁶⁴. Furthermore, Cu₃N also represents useful properties as catalyst, optical storage material, cathode catalyst in alkaline fuel cells⁶⁵⁻⁶⁷.

In this chapter three different approaches towards synthesis of nanocomposites made of inorganic nanoparticles (especially CuO and Cu₃N) within mesoporous silica hollow shells are presented.

3.1 Results and Discussion

3.1.1 Route 1

The strategy used to obtain hollow mesoporous silica spheres with copper nitride nanoparticles within the hollow core is described as follows (Fig. 3.8): (1) synthesis of carbon spheres by hydrothermal carbonisation of glucose (2) adsorption of copper ions from solution into the surface layer of the carbon spheres (denoted as Cu²⁺/carbon sphere), (3) coating of a silica shell on the Cu²⁺/carbon sphere through sol-gel processing of tetraethylorthosilicate and cetyl trimethylammonium bromide (CTAB) as the surfactant to create mesoporosity after the calcination step, (4) calcination of the composite spheres in air to remove the carbon core and organic porogen CTAB, which results in hollow mesoporous silica spheres with copper oxide nanoparticles residing within the hollow core (denoted as CuO@H-mSiO₂ sphere), and (5) conversion of CuO@H-mSiO₂ into copper nitride nanoparticles in hollow mesoporous silica spheres by ammonia nitridation (denoted as Cu₃N@H-mSiO₂ sphere).

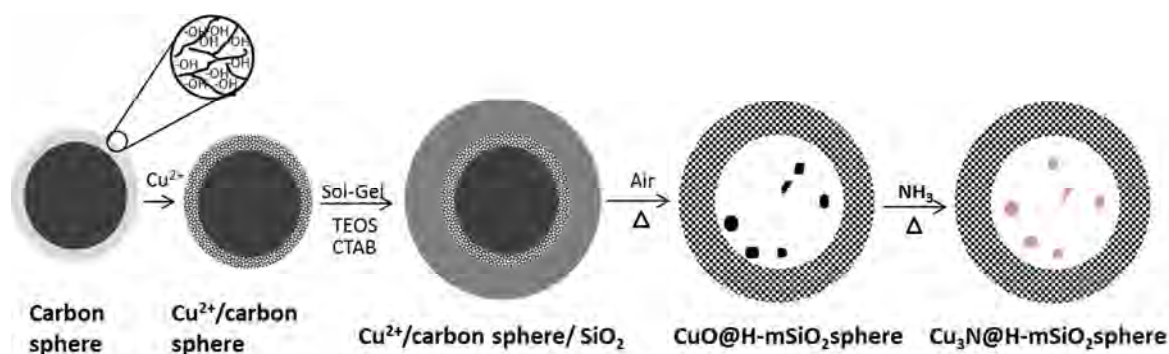


Fig. 3.8 Scheme for the synthesis of Cu₃N@H-mSiO₂.

The carbon spheres were prepared from aqueous solutions of glucose under hydrothermal conditions at 180 °C according to the procedure reported by Li et al²⁵. The surface of the carbon spheres is hydrophilic and reactive due to the existence of functional groups like -OH, -CHO, and -COOH. This active surface is interesting with respect to the adsorption of metal ions²⁶. Dispersion of these carbon spheres into the copper nitrate solution in water leads to adsorption of copper ions on the surface as the functional groups on the carbon spheres surface are able to bind copper ions through coordination or electrostatic interactions. Copper ion-adsorbed carbon spheres were coated with silica by sol-gel processing using TEOS and CTAB denoted as Cu²⁺/carbon sphere/SiO₂. Calcination of Cu²⁺/carbon sphere/SiO₂ in air at 550 °C leads to the formation of copper oxide nanoparticles within the hollow mesoporous silica spheres with simultaneous removal of carbon and CTAB. The CuO@H-mSiO₂ spheres were converted into Cu₃N@H-mSiO₂ spheres by ammonia nitridation reaction at 300 °C. All experimental details are given in section 6.3.2.

The SEM image of the carbon spheres synthesized by hydrothermal process of glucose is shown in Fig. 3.9. The carbon spheres obtained are monodisperse with diameters of around 300 nm.

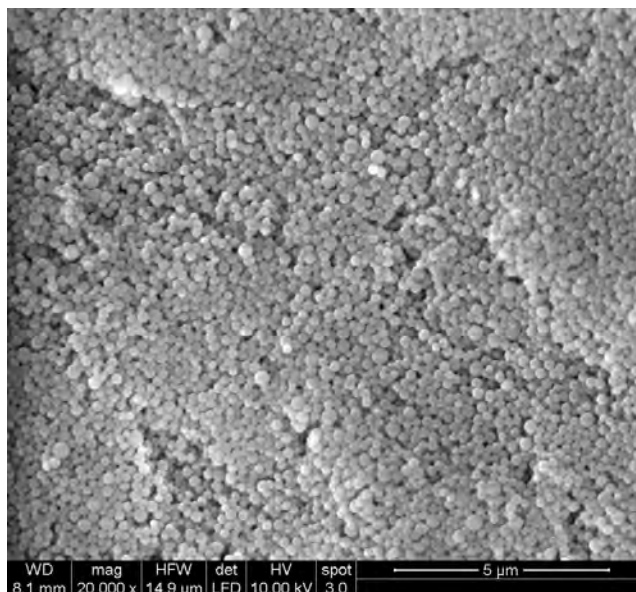


Fig. 3.9 SEM image of carbon spheres.

The TGA of Cu^{2+} /carbon sphere/ SiO_2 is shown in Fig. 3.10. The TGA curve indicates a two-step weight loss pattern, in the temperature range of 30 to 120 °C and 120 to 500 °C. The first weight loss is ascribed to the removal of physically adsorbed water. The second major weight loss is attributed to the degradation of CTAB and carbon spheres.

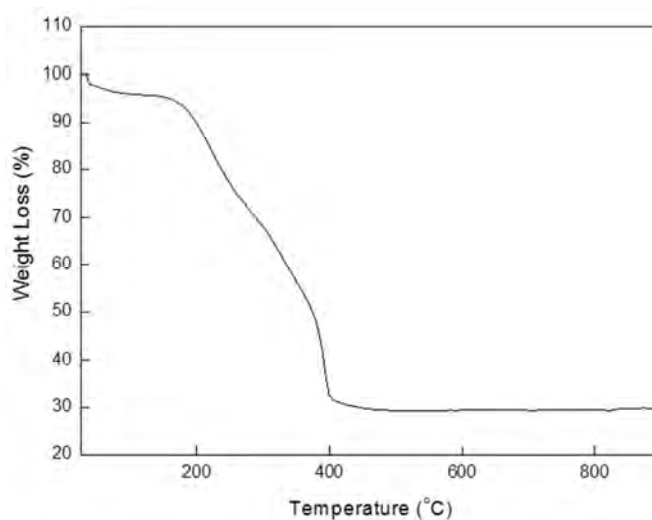


Fig. 3.10 TGA of Cu^{2+} /carbon sphere/ SiO_2 .

Based on the TGA analysis, the Cu^{2+} /carbon sphere/ SiO_2 were calcined at 550 °C in air. The black product obtained after calcination was denoted as $\text{CuO}@H\text{-mSiO}_2$ sphere. The XRD pattern of $\text{CuO}@H\text{-mSiO}_2$ sphere (Fig. 3.11a) reveals that the CuO nanoparticles crystallised in the monoclinic crystal system (JCPDS 41-0254). The crystallite size was calculated to be 19 nm by using Scherrer's equation.

Nitridation of CuO@H-mSiO₂ at 300 °C under ammonia atmosphere gave a brown product, denoted as Cu₃N@H-mSiO₂. The XRD pattern corresponding to cubic Cu₃N is revealed in Fig. 3.11b. A broad hump at < 30 degrees due to presence of amorphous silica is observed in both XRD patterns (Fig. 3.11a, b). The average crystallite size of Cu₃N calculated by Scherrer's equation is 17 nm, i.e. the crystallite size is preserved upon nitridation.

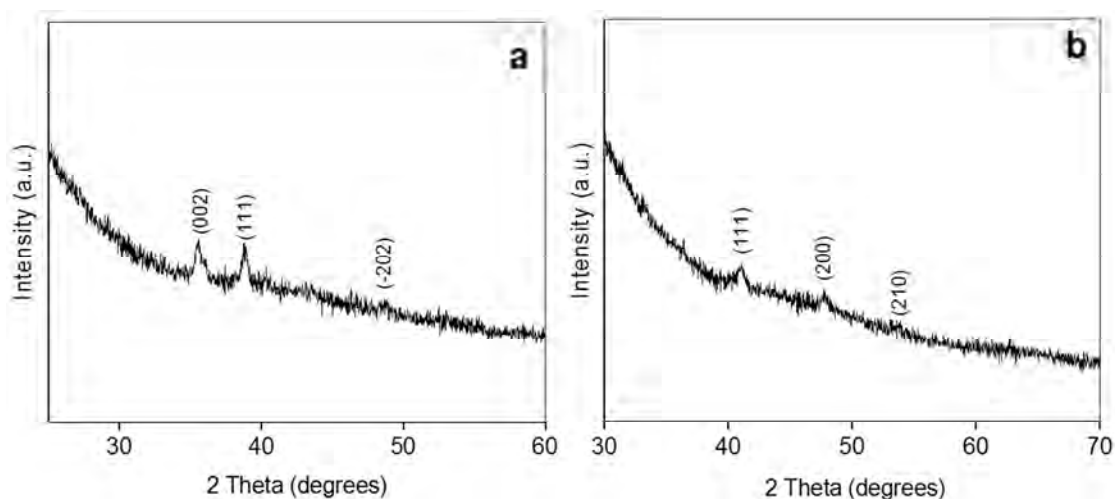


Fig. 3.11 XRD patterns of (a) CuO@H-mSiO₂ sphere and (b) Cu₃N@H-mSiO₂ sphere.

The nitrogen adsorption and desorption isotherms of CuO@H-mSiO₂ and Cu₃N@H-mSiO₂ are depicted in Fig. 3.12 (a, b). Both isotherms are type IV isotherms characteristic of the mesoporous material along with some extent of micro and macro pores. The structural properties of the samples are summarized in Table 1. The CuO@H-mSiO₂ sphere shows high surface area and the pore size distribution is centred at 2.5 nm. The surface area and pore volume is slightly lower for Cu₃N@H-mSiO₂. The reason for this decrease may be due to the heating during the nitridation reaction which might leads to collapse of some of the mesopores/micropores.

Table 1

Sample	Specific surface area ^a /m ² g ⁻¹	Pore diameter ^b / nm	Pore volume ^c /cm ³ g ⁻¹
CuO@H-mSiO ₂ sphere	953	2.5	0.78
Cu ₃ N@H-mSiO ₂ sphere	671	2.3	0.53

^a The surface area was calculated according to the BET equation. ^b The pore diameter and ^c pore volume was calculated according to the BJH method from the N₂ adsorption isotherm.

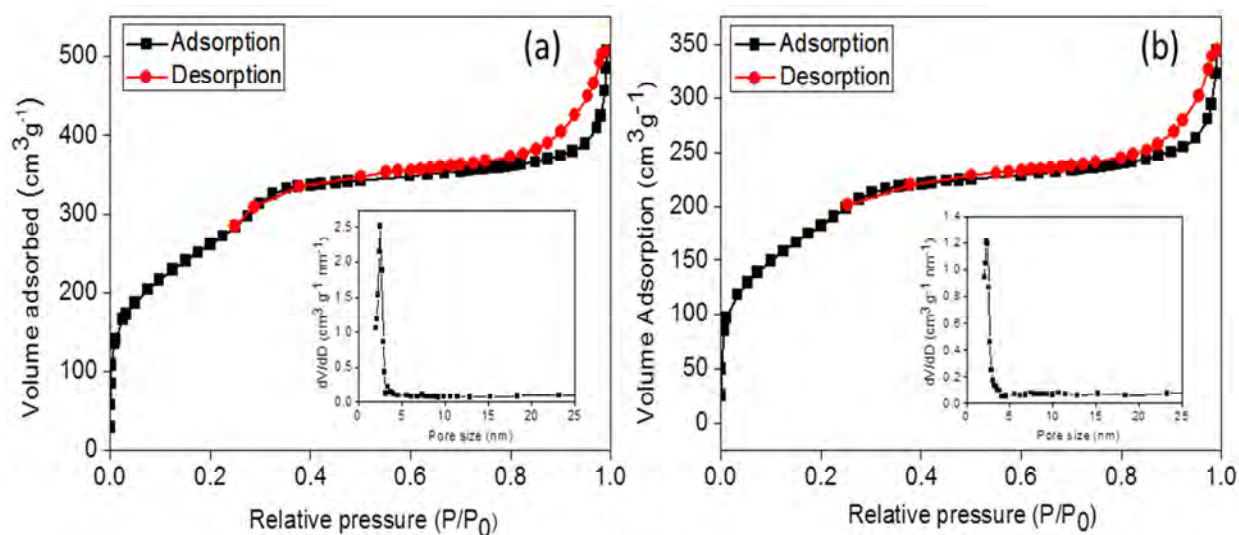


Fig. 3.12 N₂ adsorption and desorption isotherms of (a) CuO@H-mSiO₂ and (b) Cu₃N@H-mSiO₂. (Inset shows pore size distribution for corresponding sample)

The SEM image (Fig. 3.13) of Cu₃N@H-mSiO₂ shows that the spherical morphology is retained after calcination and nitridation steps.

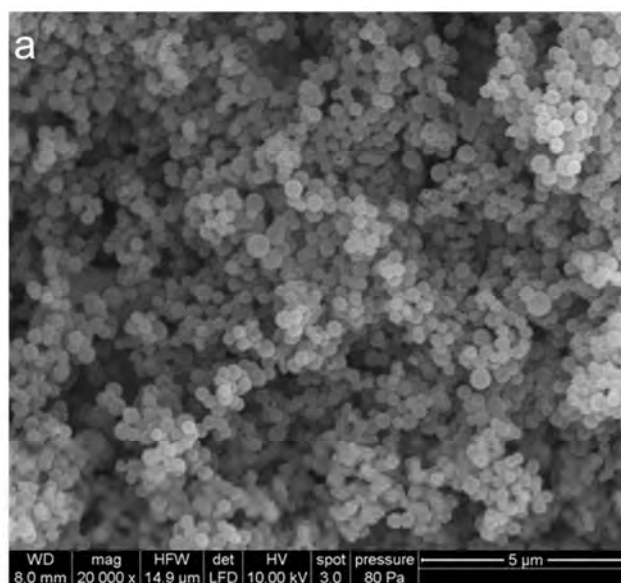


Fig. 3.13 SEM image of Cu₃N@H-mSiO₂ sphere.

The EDX spectrum (Fig. 3.14) of Cu₃N@H-mSiO₂ confirms the presence of Cu, N, O, Si, with 4 wt% of Cu loading.

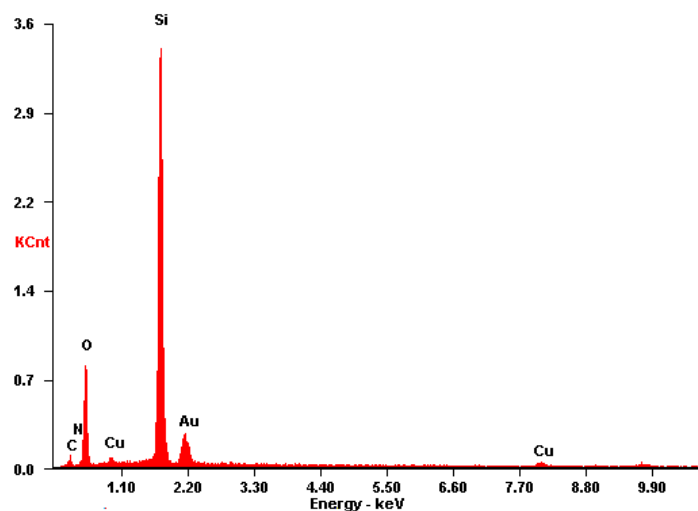


Fig. 3.14 EDX spectra of $\text{Cu}_3\text{N}@H\text{-mSiO}_2$.

The TEM images of $\text{Cu}_3\text{N}@H\text{-mSiO}_2$ spheres shown in Fig. 3.15 demonstrate the unique structure of the prepared samples. The Cu_3N nanoparticles, appearing as a bright spots, are almost entirely encapsulated in the hollow mesoporous SiO_2 spheres. This was verified from Fig. 3.15 b, where Cu_3N nanoparticles follow the shape of the sphere. The Cu_3N nanoparticles with a size of < 30 nm are well separated in the hollow core of mesoporous SiO_2 spheres.

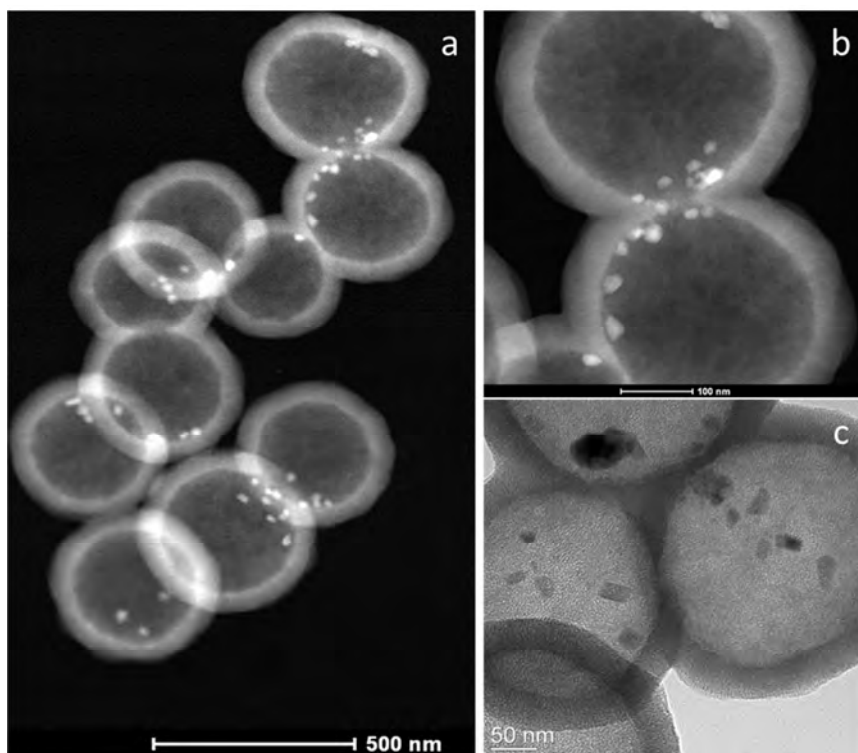


Fig. 3.15 TEM images (a,b,c) of $\text{Cu}_3\text{N}@H\text{-mSiO}_2$ sphere.

In summary, a carbon template strategy for the fabrication of $\text{Cu}_3\text{N}@H\text{-mSiO}_2$ spheres is described. Cu^{2+} adsorbed carbon spheres were successfully used as a template for the formation of $\text{CuO}@H\text{-mSiO}_2$ sphere. Post synthesis treatment of $\text{CuO}@H\text{-mSiO}_2$ sphere with ammonia at 300 °C gave $\text{Cu}_3\text{N}@H\text{-mSiO}_2$ spheres. Well separated Cu_3N nanoparticles with diameters < 30 nm in the hollow mesoporous silica shell were successfully obtained. However, loading of Cu_3N nanoparticles per silica hollow sphere is limited by the present route.

3.1.2 Route 2

A pre-shell and post-core strategy has been applied for the synthesis of inorganic cores with hollow mesoporous silica shells^{42, 68-70}. Here a similar method is used for the synthesis of hollow mesoporous silica spheres with the inner core functionalised with Cu_3N nanoparticles. The procedure for the synthesis of nanocomposites made up of copper nitride nanoparticles inside the mesoporous silica hollow spheres is shown in Fig. 3.16.

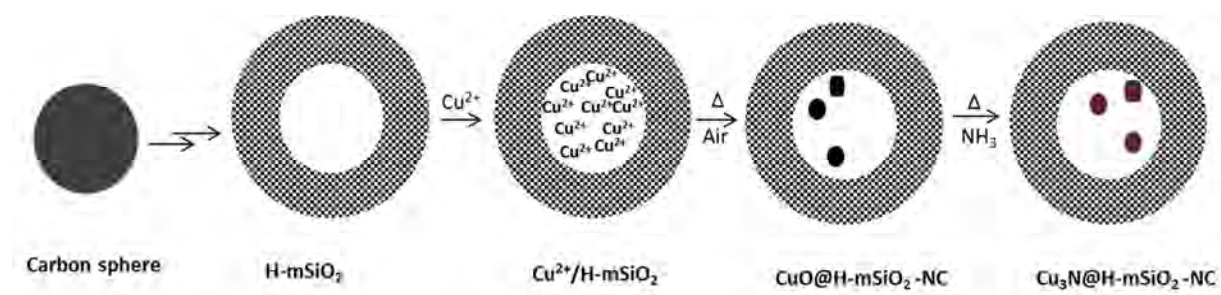


Fig. 3.16 Scheme for synthesis of $\text{Cu}_3\text{N}@H\text{-mSiO}_2\text{-NC}$.

The first step involves the synthesis of hollow mesoporous silica spheres (denoted as $H\text{-mSiO}_2$) by using monodisperse carbon spheres as template. The second step is loading of Cu^{2+} ions into the preformed $H\text{-mSiO}_2$ by following a vacuum nano-casting route described by Guo et. al⁷¹. The next step is calcination of $\text{Cu}^{2+}/H\text{-mSiO}_2$ at 400 °C in air. The calcination product was denoted as $\text{CuO}@H\text{-mSiO}_2\text{-NC}$. Further nitridation of $\text{CuO}@H\text{-mSiO}_2\text{-NC}$ at 300 °C gave $\text{Cu}_3\text{N}@H\text{-mSiO}_2\text{-NC}$. All experimental details are given in section 6.3.3.

Synthesis and morphology of carbon spheres is described in section 3.1.1. Using TEOS as the silica source and CTAB as an organic porogen, a layer of silica is coated on the carbon spheres by sol-gel processing. The TGA analysis was performed on silica-coated carbon spheres (Fig. 3.17). The silica-coated carbon spheres were calcined at 650 °C to remove the carbon spheres and CTAB, leaving only mesoporous hollow silica spheres ($H\text{-mSiO}_2$).

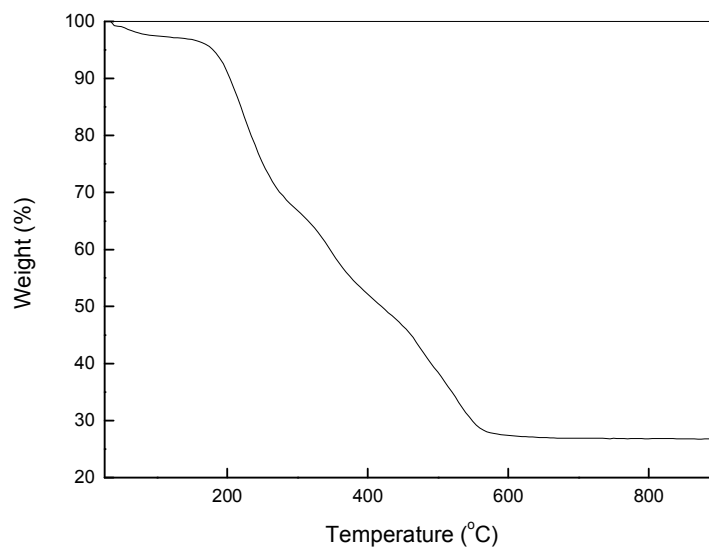


Fig. 3.17 TGA of silica coated carbon sphere.

The SEM image (Fig. 3. 18) of H-mSiO₂ spheres shows the spherical morphology, some broken spheres confirms the hollow nature of the spheres.

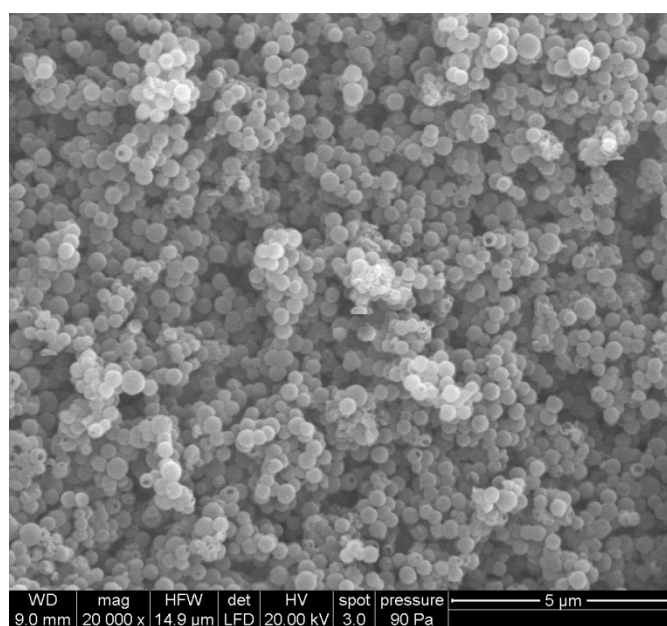


Fig. 3.18 SEM image of H-mSiO₂ spheres.

Further TEM investigation (Fig. 3.19) clearly shows the hollow spherical morphology of H-mSiO₂ with shell thickness of around 50 nm.

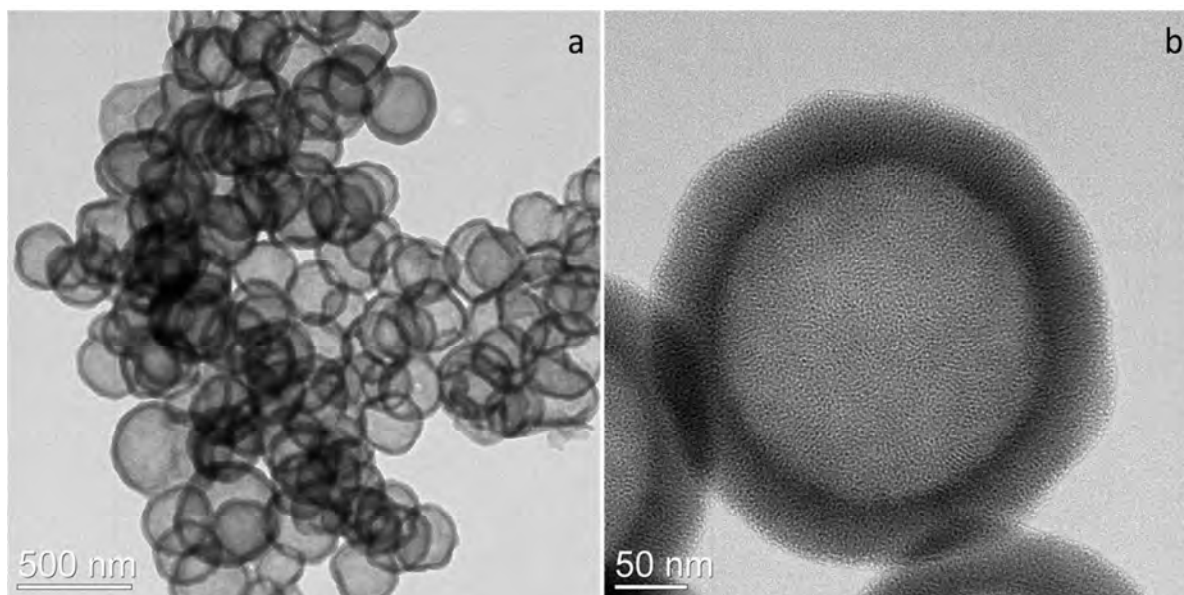


Fig. 3.19 TEM images (a, b) of H-mSiO₂ spheres.

The hollow H-mSiO₂ spheres were loaded with Cu²⁺ ions by using the vacuum nano-casting route. The H-mSiO₂ spheres were suspended in an ethanolic Cu(NO₃)₂·3H₂O solution. The turbid suspension was subjected to vacuum under ultrasonic conditions so the air in the hollow part of H-mSiO₂ could be pumped off. Next, the air pressure in the container was adjusted to normal atmosphere so that the hollow parts of the H-mSiO₂ under transitory vacuum conditions would be filled by the copper nitrate solution driven by the atmospheric pressure. The H-mSiO₂ containing Cu²⁺ ions were separated by centrifugation, dried at ambient atmosphere and washed thoroughly three times with ethanol to remove copper ions outside of H-mSiO₂. H-mSiO₂ spheres loaded with copper ions (Cu²⁺/SiO₂) were calcined in air at 400 °C. The obtained black product was denoted as CuO@H-mSiO₂-NC.

The XRD pattern of CuO@H-mSiO₂-NC composite shows a monoclinic structure of CuO crystals (JCPDS 41-0254) and amorphous silica (Fig. 3.20a). The nitridation of CuO@H-mSiO₂-NC at 300 °C under ammonia atmosphere gave a brown product denoted as Cu₃N@H-mSiO₂-NC. All peaks in the XRD pattern of Cu₃N@H-mSiO₂-NC (Fig. 3.20b) can be clearly indexed to cubic Cu₃N particles (JCPDS-86-2283), and a broad hump at < 30 degrees due to amorphous silica. The crystallite sizes calculated by Scherrer's equation were 31 and 22 nm for CuO and Cu₃N particles in CuO@H-mSiO₂-NC and Cu₃N@H-mSiO₂-NC, respectively.

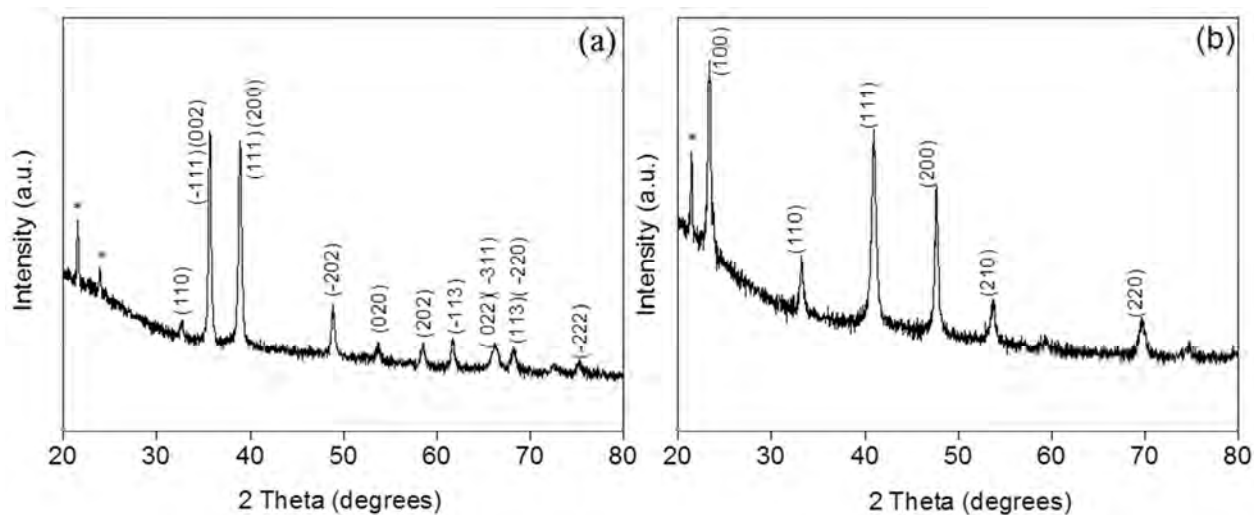


Fig. 3.20 XRD patterns of (a) CuO@H-mSiO₂-NC and (b) Cu₃N@H-mSiO₂-NC (*cristobalite).

The nitrogen adsorption and desorption isotherms of H-mSiO₂, CuO@H-mSiO₂-NC, Cu₃N@H-mSiO₂-NC are depicted in Fig. 3.21(a,b,c). All isotherms show the characteristic shape of mesoporous materials. The isotherms corresponding to CuO@H-mSiO₂-NC and Cu₃N@H-mSiO₂-NC do not show significant differences with respect to H-mSiO₂. It clearly reveals that the ordered mesostructure of H-mSiO₂ is well-preserved even after formation of CuO and Cu₃N particles. The structure parameters of all samples are summarized in Table 1.

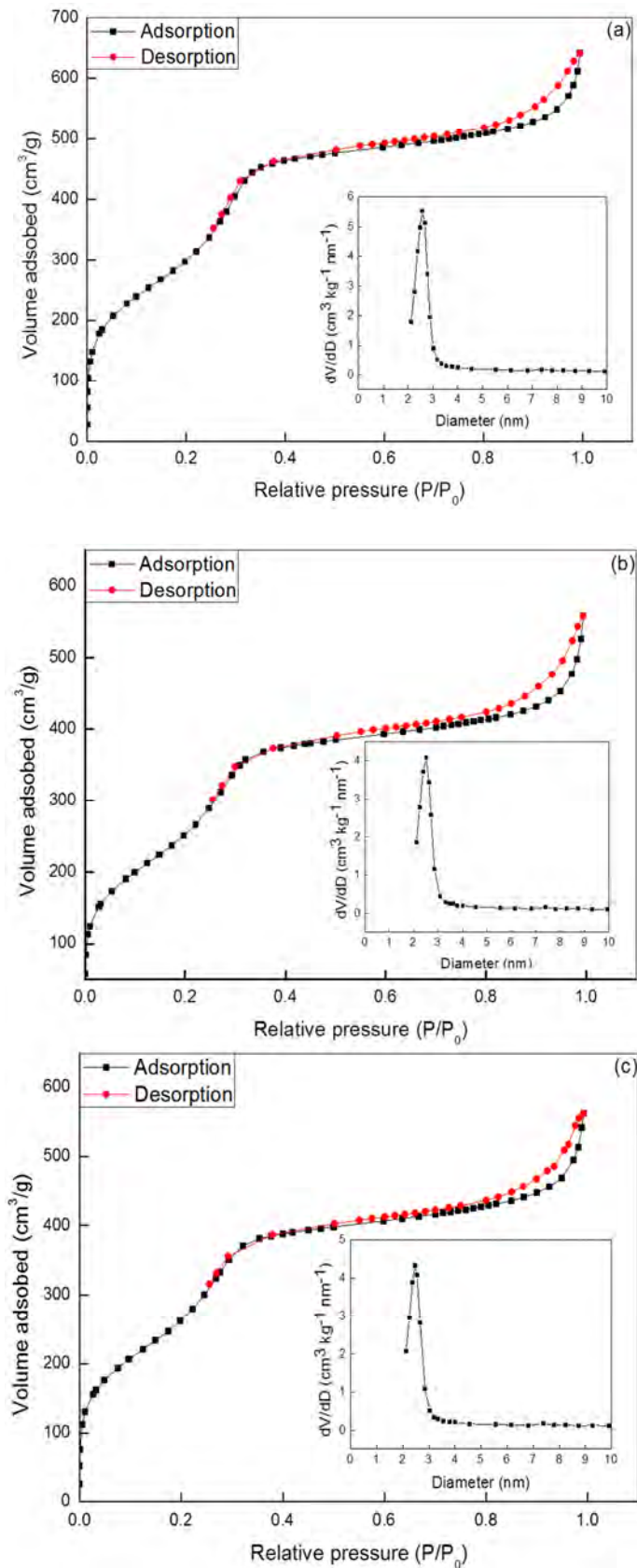


Fig. 3.21 N_2 adsorption-desorption isotherms of samples (a) H-mSiO₂ (b) CuO@H-mSiO₂-NC (c) Cu₃N@H-mSiO₂-NC. The inset shows the pore size distribution by the Barrett-Joyner-Halenda (BJH) method from adsorption branch of the corresponding sample.

Table.1

Sample	Specific surface area ^a /m ² g ⁻¹	Pore diameter ^b / nm	Pore volume ^c /cm ³ g ⁻¹
H-mSiO ₂	1104	2.6	0.79
CuO@H-mSiO ₂ -NC	936	2.6	0.64
Cu ₃ N@H-mSiO ₂ -NC	975	2.4	0.66

^a The surface area was calculated according to the BET equation. ^b The pore diameter and ^c pore volume was calculated according to the BJH method from the N₂ adsorption isotherm

The surface areas of CuO@H-mSiO₂-NC and Cu₃N@H-mSiO₂-NC are smaller than that of H-mSiO₂, which can be attributed to the inorganic phases incorporated into the hollow mesoporous silica capsules.

The SEM image was taken from Cu₃N@H-mSiO₂-NC (Fig. 3.22). The morphology remained spherical after several processing steps. EDX spectrum shown in Fig. 3.22b clearly indicates the presence of the desired elements.

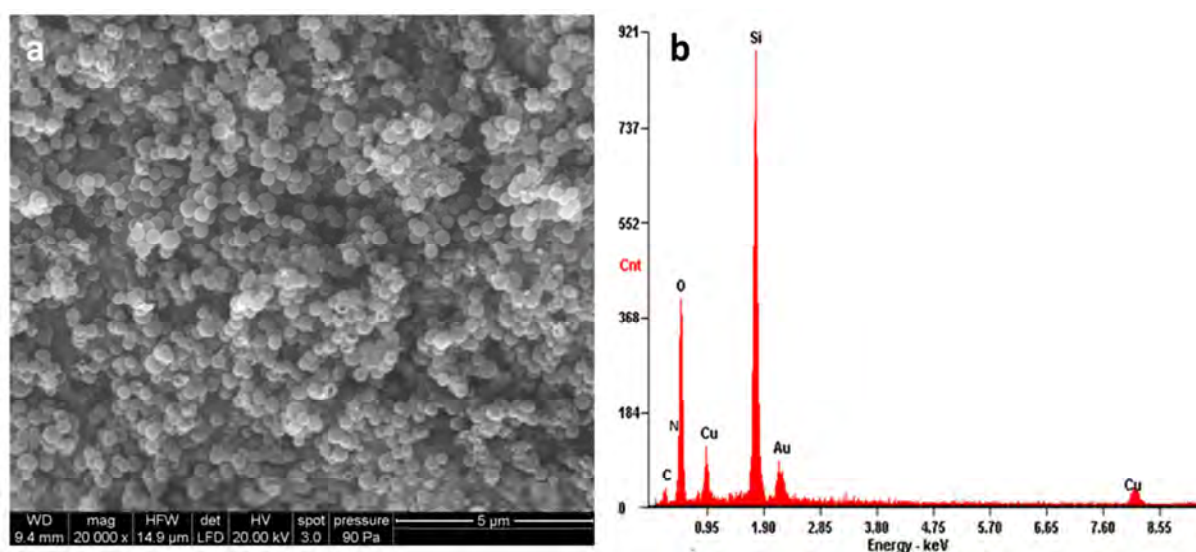


Fig. 3.22 (a) SEM image and (b) EDX spectra of Cu₃N@H-mSiO₂-NC.

In order to get more insight into the arrangement of Cu₃N nanoparticles TEM analysis was performed on Cu₃N@H-mSiO₂-NC. The TEM image (Fig. 3.23 (a)) clearly shows that the Cu₃N nanoparticles are inside as well as outside of the H-mSiO₂ shell. The STEM images (Fig. 3.23 b,c) show that the distribution of the bright spots (which corresponds to Cu₃N nanoparticles) is not even in all H-mSiO₂ and some H-mSiO₂ do not contain any Cu₃N

nanoparticles. A line scan over two hollow mesoporous silica spheres containing Cu_3N nanoparticles confirms the elemental composition (Fig. 3.23 b,d,e) of shell and core. After TEM analysis it is concluded that the vacuum nano-casting route was partially successful to obtain homogeneously distributed Cu_3N nanoparticles inside the hollow mesoporous silica shells. The Cu_3N nanoparticles outside the hollow mesoporous silica shell indicate that copper ions outside of H-mSiO₂ spheres were not completely removed by thorough washing with ethanol during synthesis.

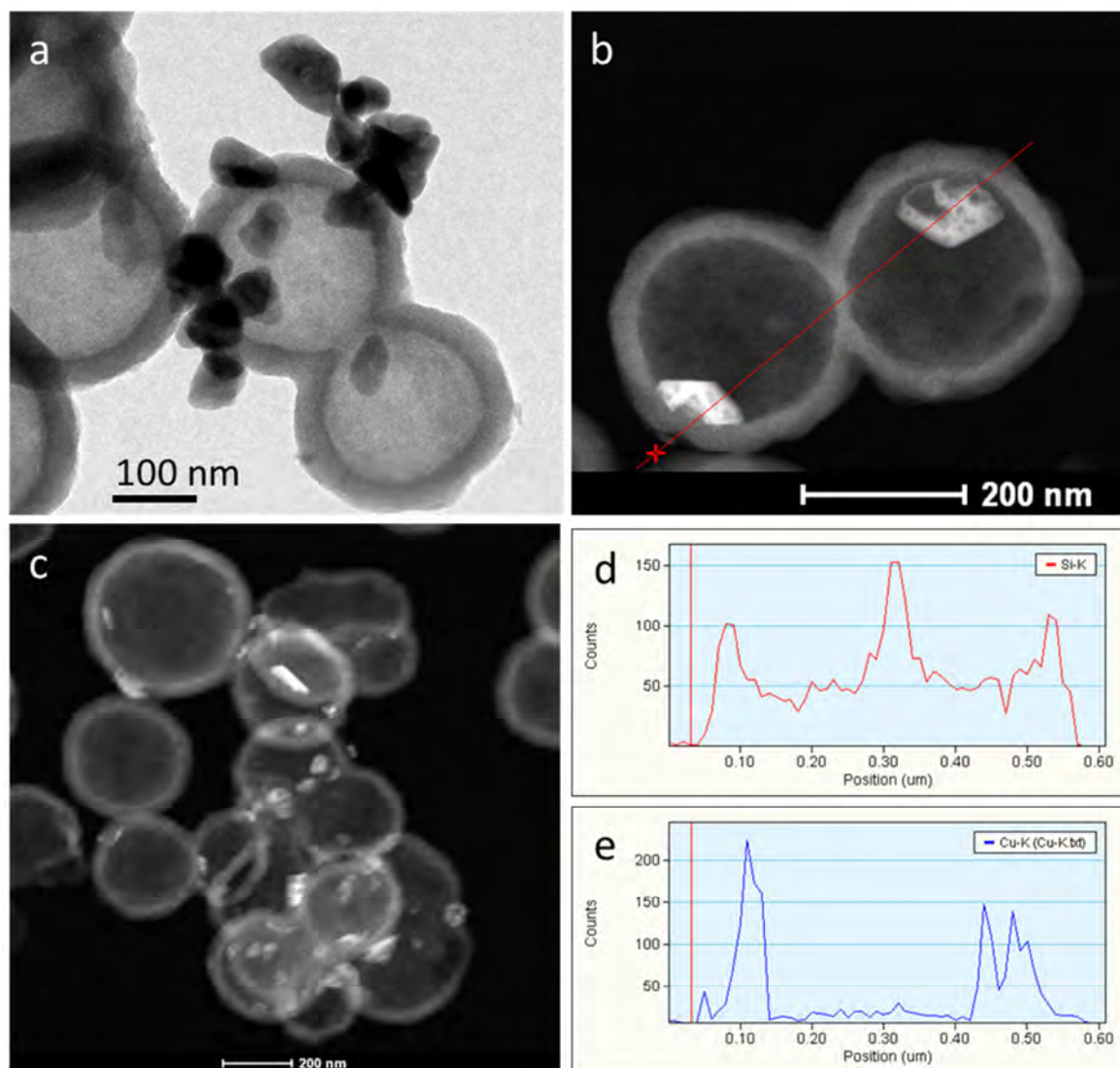


Fig. 3.23 TEM image (a,b,c) and EDX line scan over two spheres (d,e) of $\text{Cu}_3\text{N}@H\text{-mSiO}_2\text{-NC}$.

In summary, a pre-shell and post-core strategy was applied for the synthesis of Cu_3N nanoparticles inside hollow mesoporous silica spheres. The results showed however that Cu_3N nanoparticles were inside as well as outside the pre-formed H-mSiO₂ shell, and some H-

mSiO₂ do not contain any Cu₃N particles. The hollow mesoporous silica spheres were successfully synthesized via carbon sphere templating method. The CuO@H-mSiO₂-NC and Cu₃N@H-mSiO₂-NC nanocomposites were obtained by loading of copper ions into mesoporous silica hollow spheres followed by thermal oxidation and nitridation.

3.1.3 Route 3

The synthesis of Cu₃N@H-mSiO₂ spheres is schematically shown in Fig. 3.24. The synthesis and morphology of carbon spheres is described in section 3.1.1. The carbon spheres were added to an aqueous solution of [Cu(NH₃)₄(H₂O)₂]²⁺. The [Cu(NH₃)₄(H₂O)₂]²⁺ ions interact with the surface functional groups on the carbon spheres by electrostatic interaction or through coordination, forming Cu²⁺/carbon sphere. In the next step, a silica shell is coated on the surface of the Cu²⁺/carbon spheres through sol-gel processing of tetraethoxysilane and CTAB. Finally, calcination of the Cu²⁺/carbon sphere/SiO₂ composite at 500 °C in air removes the carbon spheres and CTAB giving copper oxide nanoparticles inside the mesoporous hollow silica spheres (denoted as CuO@H-mSiO₂ sphere). Finally nitridation of the CuO@H-mSiO₂ spheres at 350 °C yields Cu₃N@H-mSiO₂ spheres. All experimental details are given in section 6.3.4.

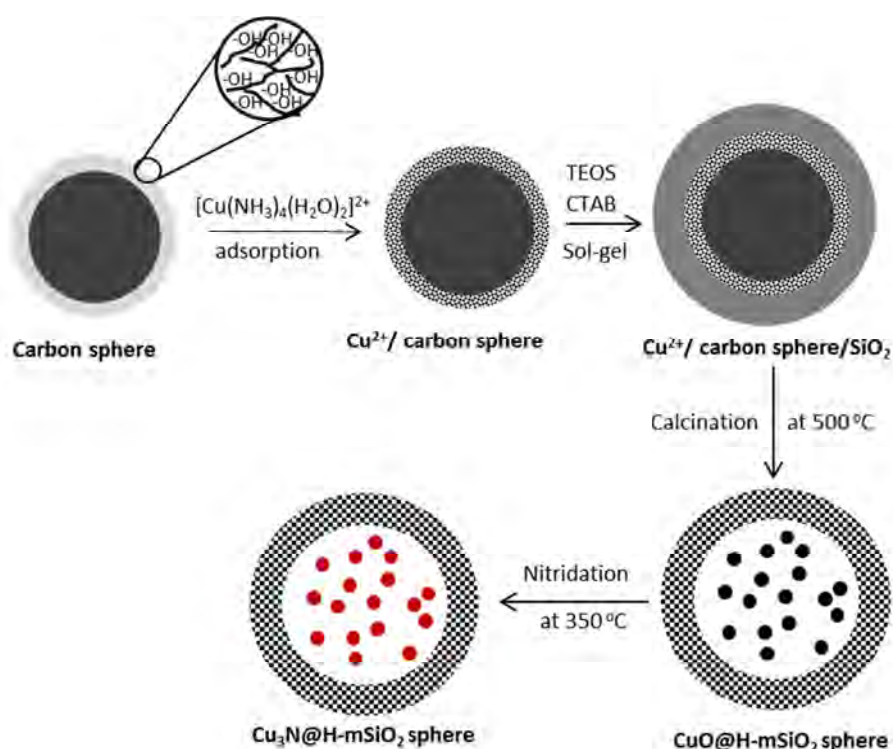


Fig. 3.24 Schematics for the synthesis of Cu₃N@H-mSiO₂ spheres.

The thermogravimetric analysis of Cu²⁺/carbon sphere/SiO₂ shows weight loss of about 65 wt.% up to 400 °C (Fig. 3.25). The Cu²⁺/carbon sphere/SiO₂ composite was calcined at 500 °C for 2 h in air. The obtained black powder, CuO@H-mSiO₂ spheres, was analysed by XRD.

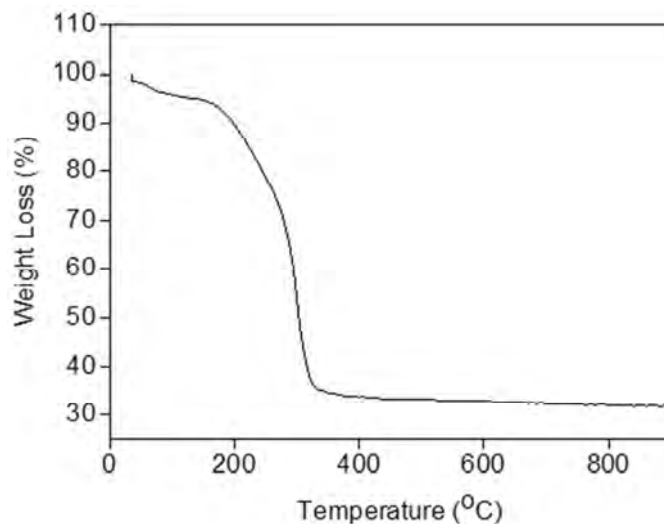


Fig. 3.25 Thermogravimetric analysis of the Cu²⁺/carbon sphere/SiO₂ composite.

The XRD pattern of the CuO@H-mSiO₂ spheres shows the monoclinic structure of the CuO crystals (JCPDS 41-0254) (Fig. 3.26a). The crystallite size calculated by Scherrer's equation was 22 nm. A broad hump at < 30 degrees is due to the amorphous silica. The nitrogen adsorption and desorption isotherms of the CuO@H-mSiO₂ spheres is depicted in Fig. 3.26 b. The isotherm is characteristic of mesoporous materials (type IV isotherms). The CuO@H-mSiO₂ spheres show surface area of 747 cm³/g, and the pore size distribution shows a sharp maximum centred at 2.6 nm.

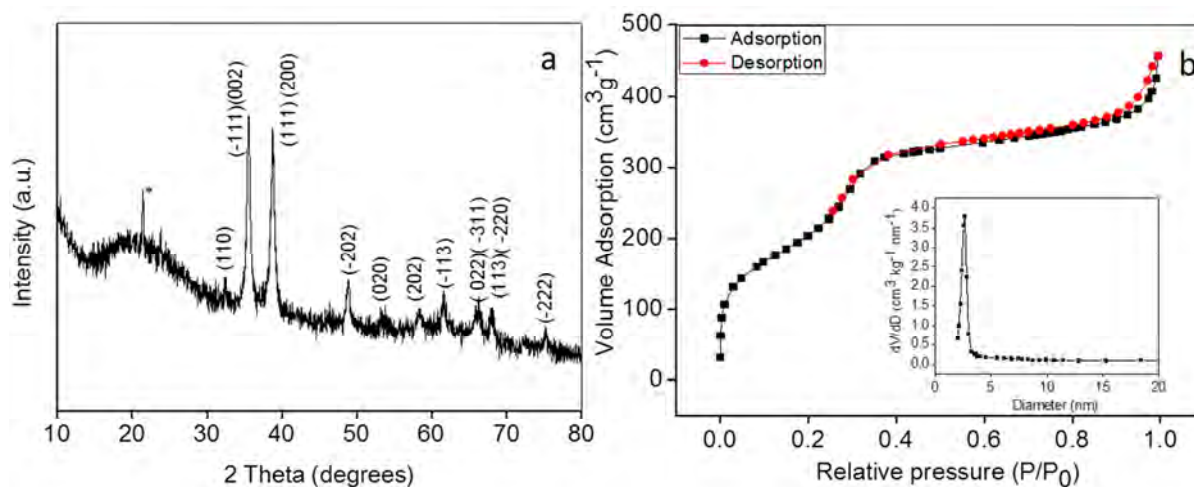


Fig. 3.26 (a) XRD pattern (* cristoballite) (b) N₂ adsorption-desorption isotherm of CuO@H-mSiO₂ spheres. The inset shows the pore size distribution by the Barrett-Joyner-Halenda (BJH) method from the adsorption branch.

The SEM image of CuO@H-mSiO₂ spheres (Fig. 3.27) shows that the spherical morphology of the template is retained. Some broken spheres in the SEM image confirm the hollow morphology of the obtained spheres.

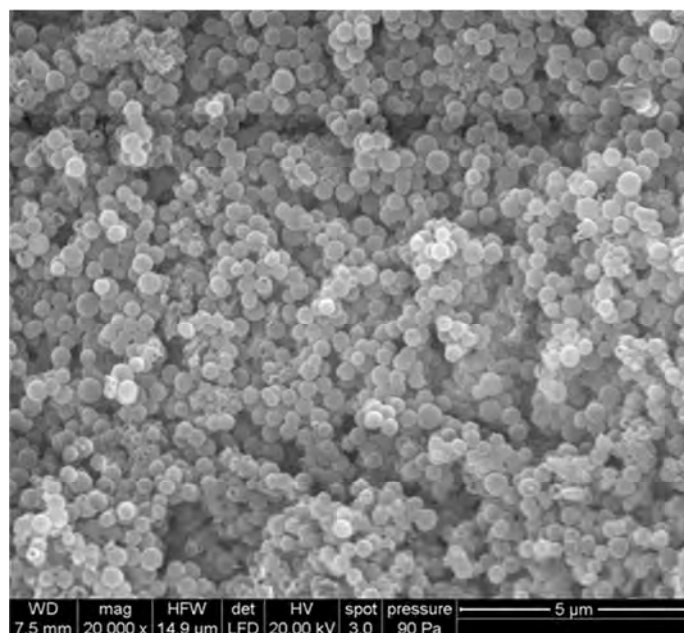


Fig. 3.27 SEM image of CuO@H-mSiO₂ spheres.

The EDX spectrum (Fig. 3.28) of CuO@H-mSiO₂ confirms the presence of Cu, O, Si, with 24 wt% of Cu loading. The copper loading is higher in the present case compared to route 1. This effect can be due to the stronger electrostatic or coordination interactions between the copper-ammonia complex and the carbon spheres compared to Cu²⁺ ions used in route 1.

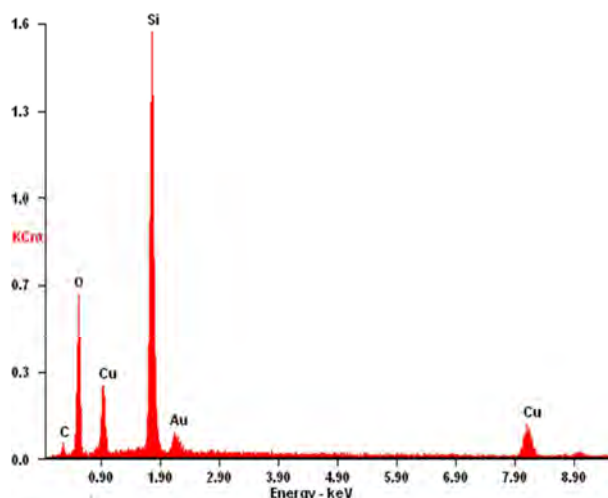


Fig. 3.28 EDX spectra of CuO@H-mSiO₂ spheres.

The TEM images (Fig. 3.29 a-d) of CuO@H-mSiO₂ spheres clearly confirm that CuO nanoparticles are exclusively located inside the hollow silica spheres. Fig 3.29c indicates the mesoporous structure of the silica shell. The thickness of silica shell is around 40 nm in the present case while it could be easily tuned by changing the weight ratio of carbon sphere to TEOS.

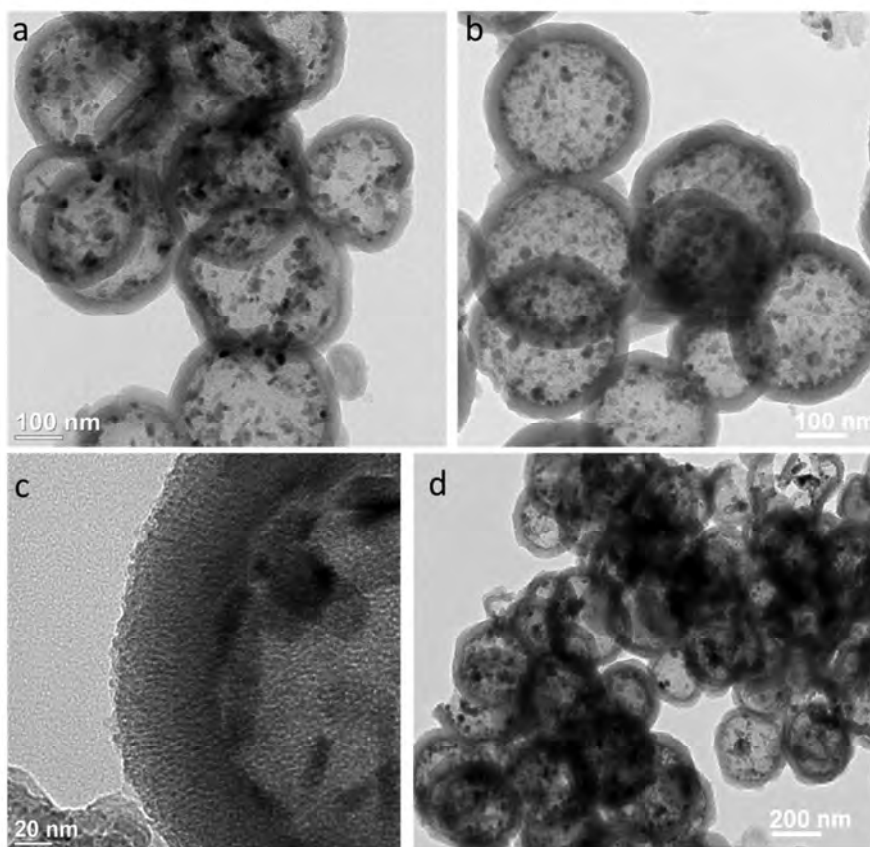


Fig. 3.29 TEM images (a,b,c,d) of CuO@H-mSiO₂ spheres.

Nitridation of the CuO@H-mSiO₂ spheres at 350 °C for 2 h in ammonia atmosphere gave a brown product denoted as Cu₃N@H-mSiO₂ spheres. The XRD analysis (Fig. 3.30a) of the product showed cubic Cu₃N particles (JCPDS-86-2283). The crystallite size calculated by Scherrer's equation was 15 nm for Cu₃N particles. A broad hump at < 30 degrees is due to amorphous silica.

The nitrogen adsorption and desorption isotherms of the Cu₃N@H-mSiO₂ spheres are depicted in Fig. 3.30b. It shows type IV isotherms characteristic of mesoporous materials. The surface area after nitridation is 523 cm³/g, and the pore size distribution is centred at 2.4 nm.

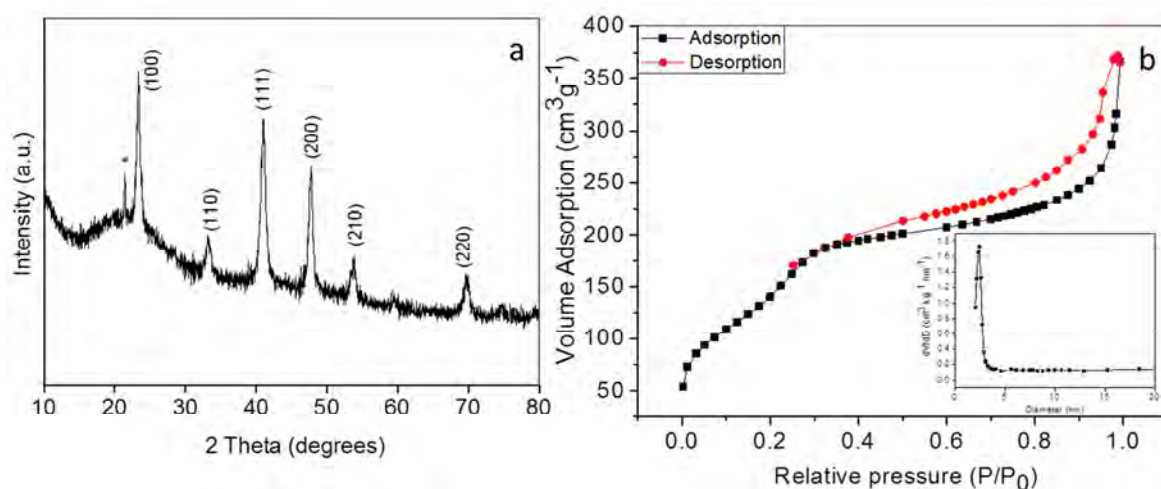


Fig. 3.30 (a) XRD pattern (* cristobalite) (b) N₂ adsorption-desorption isotherm of Cu₃N@H-mSiO₂ spheres. The inset shows the pore size distribution by the Barrett-Joyner-Halenda (BJH) method from the adsorption branch of the corresponding sample.

The morphology of the Cu₃N@H-mSiO₂ spheres is almost similar to CuO@H-mSiO₂ spheres as shown in Fig. 3.31.

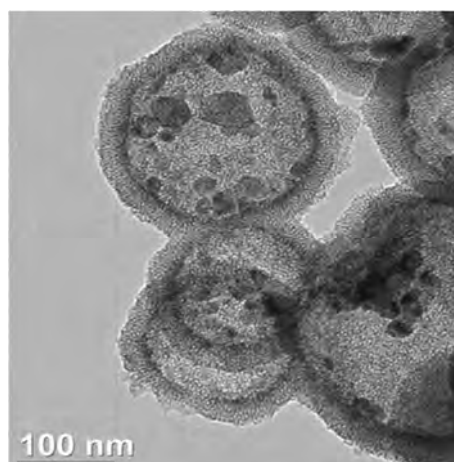


Fig. 3.31 TEM image of Cu₃N@H-mSiO₂ spheres.

3.2 Conclusion

A multistep synthesis methodology using carbon spheres as a template and [Cu(NH₃)₄(H₂O)₂]²⁺ precursor is developed for the synthesis of CuO@H-mSiO₂ spheres. The CuO nanoparticles are formed exclusively inside the mesoporous hollow silica shell. The CuO nanoparticles in the hollow mesoporous silica spheres were transformed into Cu₃N nanoparticles by nitridation without affecting the silica shell structure. The copper loading

per silica shell is high compared to route 1, which might be due to strong electrostatic or coordination interactions between $[\text{Cu}(\text{NH}_3)_4(\text{H}_2\text{O})_2]^{2+}$ ions with functional groups on the surface of carbon spheres compared to Cu^{2+} ions used in route 1.

3.3 References

1. Xue, X. J.; Wang, F.; Liu, X. G. *Journal of Materials Chemistry* **2011**, 21, (35), 13107-13127.
2. Hu, J.; Chen, M.; Fang, X. S.; Wu, L. W. *Chemical Society reviews* **2011**, 40, (11), 5472-5491.
3. Wang, Z. Y.; Zhou, L.; Lou, X. W. *Advanced materials* **2012**, 24, (14), 1903-1911.
4. Hu, J.; Chen, M.; Fang, X.; Wu, L. *Chemical Society reviews* **2011**, 40, (11), 5472-91.
5. Lou, X. W.; Archer, L. A.; Yang, Z. C. *Advanced materials* **2008**, 20, (21), 3987-4019.
6. Lai, X. Y.; Halpert, J. E.; Wang, D. *Energy & Environmental Science* **2012**, 5, (2), 5604-5618.
7. Zeng, H. C. *Journal of Materials Chemistry* **2011**, 21, (21), 7511.
8. Ghosh Chaudhuri, R.; Paria, S. *Chemical reviews* **2012**, 112, (4), 2373-433.
9. Liu, J.; Qiao, S. Z.; Chen, J. S.; Lou, X. W.; Xing, X. R.; Lu, G. Q. *Chemical communications* **2011**, 47, (47), 12578-12591.
10. Tang, F. Q.; Li, L. L.; Chen, D. *Advanced materials* **2012**, 24, (12), 1504-1534.
11. Shevchenko, E. V.; Bodnarchuk, M. I.; Kovalenko, M. V.; Talapin, D. V.; Smith, R. K.; Aloni, S.; Heiss, W.; Alivisatos, A. P. *Advanced materials* **2008**, 20, (22), 4323-4329.
12. Deng, D.; Lee, J. Y. *Chemistry of Materials* **2008**, 20, (5), 1841-1846.
13. Liu, J.; Qiao, S. Z.; Hu, Q. H.; Lu, G. Q. *Small* **2011**, 7, (4), 425-443.
14. Zhang, W. M.; Hu, J. S.; Guo, Y. G.; Zheng, S. F.; Zhong, L. S.; Song, W. G.; Wan, L. J. *Advanced Materials* **2008**, 20, (6), 1160-1165.
15. Titirici, M. M.; Antonietti, M.; Thomas, A. *Chemistry of Materials* **2006**, 18, (16), 3808-3812.
16. Strandwitz, N. C.; Stucky, G. D. *Chemistry of Materials* **2009**, 21, (19), 4577-4582.
17. Caruso, R. A.; Susha, A.; Caruso, F. *Chemistry of Materials* **2001**, 13, (2), 400-409.
18. Blas, H.; Save, M.; Pasetto, P.; Boissiere, C.; Sanchez, C.; Charleux, B. *Langmuir* **2008**, 24, (22), 13132-13137.
19. Atae-Esfahani, H.; Nemoto, Y.; Wang, L.; Yamauchi, Y. *Chemical communications* **2011**, 47, (13), 3885-3887.
20. Chen, Z.; Cui, Z. M.; Niu, F.; Jiang, L.; Song, W. G. *Chemical Communications* **2010**, 46, (35), 6524-6526.

21. Zhu, Y. F.; Kockrick, E.; Ikoma, T.; Hanagata, N.; Kaskel, S. *Chemistry of Materials* **2009**, 21, (12), 2547-2553.
22. Wang, X.; Hu, P.; Yuan, F. L.; Yu, L. J. *Journal of Physical Chemistry C* **2007**, 111, (18), 6706-6712.
23. He, F.; Yang, P. P.; Wang, D.; Li, C. X.; Niu, N.; Gai, S. L.; Zhang, M. L. *Langmuir* **2011**, 27, (9), 5616-5623.
24. Sun, X. M.; Liu, J. F.; Li, Y. D. *Chemistry-a European Journal* **2006**, 12, (7), 2039-2047.
25. Sun, X. M.; Li, Y. D. *Angewandte Chemie-International Edition* **2004**, 43, (29), 3827-3831.
26. Sun, X. M.; Li, Y. D. *Angewandte Chemie-International Edition* **2004**, 43, (5), 597-601.
27. Makowski, P.; Cakan, R. D.; Antonietti, M.; Goettmann, F.; Titirici, M. M. *Chemical communications* **2008**, (8), 999-1001.
28. Sun, X. M.; Li, Y. D. *Langmuir* **2005**, 21, (13), 6019-6024.
29. Hu, Y.; Liu, Y.; Qian, H. S.; Li, Z. Q.; Chen, J. F. *Langmuir* **2010**, 26, (23), 18570-18575.
30. Kong, L. R.; Lu, X. F.; Bian, X. J.; Zhang, W. J.; Wang, C. *Langmuir* **2010**, 26, (8), 5985-5990.
31. Tang, S. C.; Vongehr, S.; Meng, X. K. *Journal of Materials Chemistry* **2010**, 20, (26), 5436-5445.
32. Wu, S. H.; Tseng, C. T.; Lin, Y. S.; Lin, C. H.; Hung, Y.; Mou, C. Y. *Journal of Materials Chemistry* **2011**, 21, (3), 789-794.
33. Wang, X. L.; Cui, T. Y.; Cui, F.; Zhang, Y. J.; Li, D.; Zhang, Z. D. *Chemical communications* **2011**, 47, (22), 6329-6331.
34. Sasidharan, M.; Gunawardhana, N.; Inoue, M.; Yusa, S.; Yoshio, M.; Nakashima, K. *Chemical Communications* **2012**, 48, (26), 3200-3202.
35. Liu, J.; Yang, H. Q.; Kleitz, F.; Chen, Z. G.; Yang, T. Y.; Strounina, E.; Lu, G. Q.; Qiao, S. Z. *Advanced Functional Materials* **2012**, 22, (3), 591-599.
36. Du, X.; He, J. H. *Nanoscale* **2011**, 3, (10), 3984-4002.
37. Chen, J. S.; Li, C. M.; Zhou, W. W.; Yan, Q. Y.; Archer, L. A.; Lou, X. W. *Nanoscale* **2009**, 1, (2), 280-285.
38. Fang, B. Z.; Kim, M.; Kim, J. H.; Yu, J. S. *Langmuir* **2008**, 24, (20), 12068-12072.
39. Zhu, Y.; Meng, W.; Hanagata, N. *Dalton transactions* **2011**, 40, (39), 10203-8.

40. Wang, S. N.; Zhang, M. C.; Zhang, W. Q. *ACS Catalysis* **2011**, 1, (3), 207-211.
41. Chen, Y.; Chen, H. R.; Sun, Y.; Zheng, Y. Y.; Zeng, D. P.; Li, F. Q.; Zhang, S. J.; Wang, X.; Zhang, K.; Ma, M.; He, Q. J.; Zhang, L. L.; Shi, J. L. *Angewandte Chemie-International Edition* **2011**, 50, (52), 12505-12509.
42. Zhai, X. F.; Yu, M.; Cheng, Z. Y.; Hou, Z. Y.; Ma, P. A.; Yang, D. M.; Kang, X. J.; Dai, Y. L.; Wang, D.; Lin, J. *Dalton transactions* **2011**, 40, (48), 12818-12825.
43. Wang, D. P.; Zeng, H. C. *Chemistry of Materials* **2011**, 23, (22), 4886-4899.
44. Yamada, Y.; Mizutani, M.; Nakamura, T.; Yano, K. *Chemistry of Materials* **2010**, 22, (5), 1695-1703.
45. Tsunoyama, H.; Sakurai, H.; Ichikuni, N.; Negishi, Y.; Tsukuda, T. *Langmuir* **2004**, 20, (26), 11293-11296.
46. Ranu, B. C.; Dey, R.; Chatterjee, T.; Ahammed, S. *ChemSusChem* **2012**, 5, (1), 22-44.
47. Huang, W. Y.; Liu, J. H. C.; Alayoglu, P.; Li, Y. M.; Witham, C. A.; Tsung, C. K.; Toste, F. D.; Somorjai, G. A. *Journal of the American Chemical Society* **2010**, 132, (47), 16771-16773.
48. Fang, X.; Liu, Z.; Hsieh, M. F.; Chen, M.; Liu, P.; Chen, C.; Zheng, N. *ACS Nano* **2012**, 6, (5), 4434-4444.
49. Wang, H.; Wang, J. G.; Zhou, H. J.; Liu, Y. P.; Sun, P. C.; Chen, T. H. *Chemical communications* **2011**, 47, (27), 7680-7682.
50. Ikeda, S.; Ishino, S.; Harada, T.; Okamoto, N.; Sakata, T.; Mori, H.; Kuwabata, S.; Torimoto, T.; Matsumura, M. *Angewandte Chemie-International Edition* **2006**, 45, (42), 7063-7066.
51. Liu, B.; Zhang, W.; Feng, H. L.; Yang, X. L. *Chemical communications* **2011**, 47, (42), 11727-11729.
52. Park, J. C.; Song, H. *Nano Research* **2011**, 4, (1), 33-49.
53. Park, J. C.; Lee, H. J.; Kim, J. Y.; Park, K. H.; Song, H. *Journal of Physical Chemistry C* **2010**, 114, (14), 6381-6388.
54. Yao, K. X.; Zeng, H. C. *Chemistry of Materials* **2012**, 24, (1), 140-148.
55. Park, J. C.; Heo, E.; Kim, A.; Kim, M.; Park, K. H.; Song, H. *Journal of Physical Chemistry C* **2011**, 115, (32), 15772-15777.
56. Anisur, R. M.; Shin, J.; Choi, H. H.; Yeo, K. M.; Kang, E. J.; Lee, I. S. *Journal of Materials Chemistry* **2010**, 20, (47), 10615-10621.
57. Sanles-Sobrido, M.; Perez-Lorenzo, M.; Rodriguez-Gonzalez, B.; Salgueirino, V.; Correa-Duarte, M. A. *Angewandte Chemie-International Edition* **2012**, 51, (16), 3877-3882.

58. Park, J. C.; Bang, J. U.; Lee, J.; Ko, C. H.; Song, H. *Journal of Materials Chemistry* **2010**, 20, (7), 1239-1246.
59. Lin, C. H.; Liu, X. Y.; Wu, S. H.; Liu, K. H.; Mou, C. Y. *Journal of Physical Chemistry Letters* **2011**, 2, (23), 2984-2988.
60. Valdes-Solis, T.; Valle-Vigon, P.; Sevilla, M.; Fuertes, A. B. *Journal of Catalysis* **2007**, 251, (1), 239-243.
61. Chen, C. Q.; Qu, J.; Cao, C. Y.; Niu, F.; Song, W. G. *Journal of Materials Chemistry* **2011**, 21, (15), 5774-5779.
62. Zaccheria, F.; Santoro, F.; Psaro, R.; Ravasio, N. *Green Chemistry* **2011**, 13, (3), 545-548.
63. Song, C. Y.; Wang, C. L.; Zhu, H. Y.; Wu, X. C.; Dong, L.; Chen, Y. *Catalysis Letters* **2008**, 120, (3-4), 215-220.
64. Chen, C. K.; Chen, Y. W.; Lin, C. H.; Lin, H. P.; Lee, C. F. *Chemical communications* **2010**, 46, (2), 282-284.
65. Maruyama, T.; Morishita, T. *Applied Physics Letters* **1996**, 69, (7), 890-891.
66. Wu, H. B.; Chen, W. *Journal of the American Chemical Society* **2011**, 133, (39), 15236-15239.
67. Lee, B. S.; Yi, M.; Chu, S. Y.; Lee, J. Y.; Kwon, H. R.; Lee, K. R.; Kang, D.; Kim, W. S.; Bin Lim, H.; Lee, J.; Youn, H. J.; Chi, D. Y.; Hur, N. H. *Chemical Communications* **2010**, 46, (22), 3935-3937.
68. Guo, L. M.; Cui, X. Z.; Li, Y. S.; He, Q. J.; Zhang, L. X.; Bu, W. B.; Shi, J. L. *Chemistry-an Asian Journal* **2009**, 4, (9), 1480-1485.
69. Hah, H. J.; Um, J. I.; Han, S. H.; Koo, S. M. *Chemical communications* **2004**, (8), 1012-1013.
70. Fuertes, A. B.; Sevilla, M.; Valdes-Solis, T.; Tartaj, P. *Chemistry of Materials* **2007**, 19, (22), 5418-5423.
71. Guo, L. M.; Li, J. T.; Zhang, L. X.; Li, J. B.; Li, Y. S.; Yu, C. C.; Shi, J. L.; Ruan, M. L.; Feng, J. W. *Journal of Materials Chemistry* **2008**, 18, (23), 2733-2738.

Chapter 4

Synthesis of CuO@SiO_2 and $\text{Cu}_3\text{N@SiO}_2$ Hierarchical Hollow Spheres (HHSs) via CuSiO_3 HHSs

Nanostructured inorganic materials having spherical hollow morphologies have received much attention owing to their characteristic shape, well-controlled size, high surface area and large void space, which makes them potential candidates for various technological applications¹⁻⁵. Nanostructured metal silicates with hierarchical morphologies have potential applications in catalysis, gas adsorption, and biomolecule separation⁶⁻⁸. Recently, hollow nanostructures of metal silicate materials were synthesized and showed applications in removal of organic dyes and heavy metal ions from waste water, as well as biomolecule separation⁹⁻¹¹.

The scheme for the general synthesis of porous hollow nanostructures of metal silicate materials through a hydrothermal process using Stöber silica spheres as a chemical template is shown in Fig. 4.1. During hydrothermal reaction at elevated temperature silica spheres dissolve through breaking silicon-oxygen bonds and form silicate ions in alkaline media. These silicate ions react with the metal cations around the SiO_2 spheres and produce a metal silicate on the surface of the SiO_2 sphere. The metal silicate shell continues growing thicker until all the metal ions are transformed into a metal silicate shell. The rest of the silica core dissolves in alkaline medium under hydrothermal conditions leading to the formation of a hollow metal silicate nanostructure¹²⁻¹⁴.

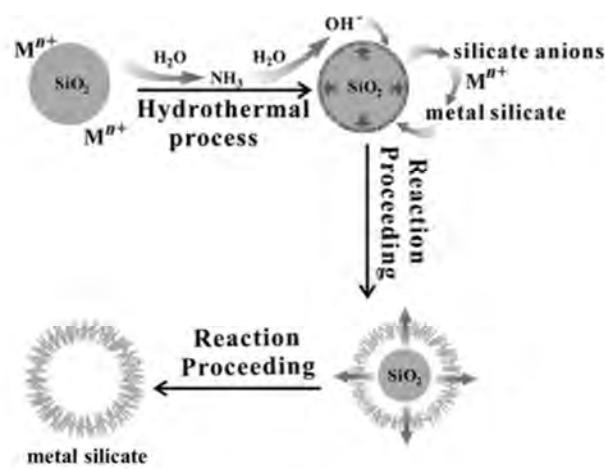


Fig. 4.1 Scheme for the synthesis of metal silicate hollow nanostructures through a hydrothermal process.

The feasibility to chemically convert metal silicate nanostructures with hierarchical morphologies into structurally new chemical entities offers great advantages for fabrication of new functional materials. In the literature, nanostructured metal silicates with hierarchical morphologies were employed as precursors for constructing new materials by subsequent reactions. For example, SiO₂@nickel silicate was used as template to synthesize hierarchical NiS hollow spheres¹⁵. The synthesis of hierarchical NiS hollow spheres is schematically shown in Fig. 4.2.

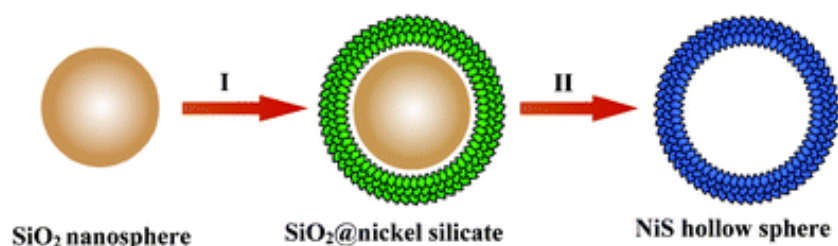


Fig. 4.2 Schematic illustration of the formation of NiS hollow spheres by a template conversion route: (I) uniform precipitation of a nickel silicate shell on silica nanospheres; (II) chemical conversion to NiS hollow spheres with simultaneous template elimination in the presence of Na₂S.

Jin and co-workers reported the synthesis of nickel-silica composite hollow spheres by reduction of Ni₃Si₂O₅(OH)₄ under hydrogen at elevated temperature (Fig. 4.3). The as-prepared hollow nanospheres exhibited high catalytic activity and good selectivity in acetone hydrogenation reaction¹⁶.

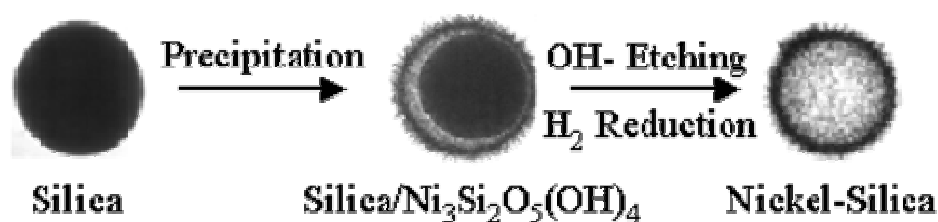


Fig. 4.3 Schematic illustration for the preparation of nickel-silica composite hollow nanospheres.

Furthermore nickel nanoparticles on SiO₂ were synthesized through hydrogen reduction of nickel phyllosilicate/SiO₂ as shown in Fig. 4.4. The final morphology was successfully employed as an active nanocatalyst for the hydrogen transfer reaction of acetophenone¹⁷.

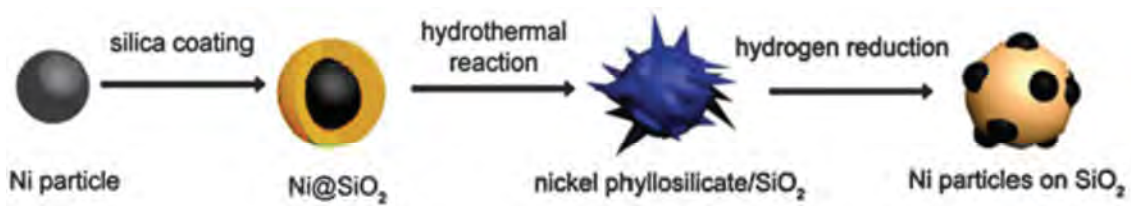


Fig. 4.4 Chemical transformation and subsequent morphology change of nickel–silica hybrid nanoparticles.

Very recently arrays of ultrafine CuS nanoneedles on a carbon nanotube (CNT) backbone were synthesized from copper silicate nanoneedles under hydrothermal conditions (Fig. 4.5). The unique architecture and intrinsic properties of the CNT@CuS hierarchical structures exhibited high capacitance and excellent cycling stability¹⁸.

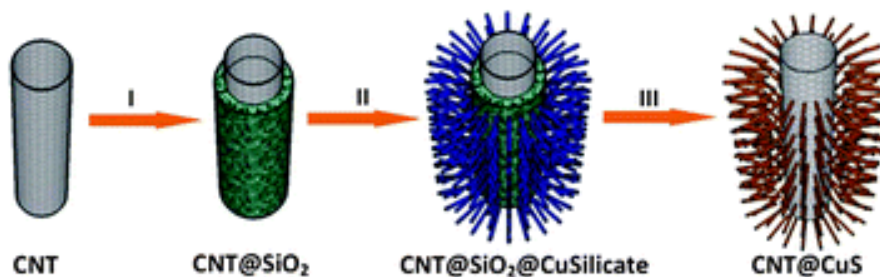


Fig. 4.5 Schematic illustration of the formation of a CuS nanoneedles array supported on the CNT backbone (CNT@CuS) by a template conversion route: (I) Uniform coating of a silica layer on CNT; (II) growth of copper silicate nanoneedles on the silica layer; and (III) chemical conversion to CNT@CuS with simultaneous elimination of the silica layer.

Recent advances in research show that there is tremendous scope to explore metal silicate based hierarchical nanostructures for synthesis of new composite materials.

Inorganic silica-based composite materials having structural features in the nanometer regime have been investigated in various fields, such as catalysis, sensing and optics¹⁹⁻²². Silica supports various nanostructures without altering their chemical and physical properties²³⁻²⁵. The chemical inertness, high temperature stability and biocompatibility are important features of silica which makes them ideal ingredient of composite materials²⁶⁻²⁸.

Metal oxides along with metal nitrides comprise major classes of inorganic materials having important technological applications²⁹⁻³¹. For example, copper oxide (CuO) shows great potential in catalysis. More recently the applications also involve an effective photocathode for water splitting and gas sensing. Copper nitride (Cu₃N) is regarded as one of the most promising materials for optical storage devices, high-speed integrated circuits and catalysis³²⁻³⁷. There is tremendous scope to synthesize composites based on these materials with

hierarchical nanostructures, which is interesting for a wide range of potential new applications. In this work, hierarchical hollow spherical nanostructures of copper oxide@SiO₂ and copper nitride@SiO₂ were synthesized and characterised.

4.1 Results and Discussion

Synthesis of CuO@SiO₂ and Cu₃N@SiO₂ HHSs from single source CuSiO₃ HHSs is depicted in Fig. 4.6. CuSiO₃ HHSs were synthesized by using Stöber silica spheres as a chemical template under hydrothermal process by following experimental procedure reported by Wang et al. with slight modifications³⁸. Monodisperse silica spheres were prepared by the well-known Stöber process³⁹. Interfacial reaction between finely dispersed Stöber silica spheres with copper nitrate in an alkaline medium under hydrothermal treatment at 140 °C resulted in formation of CuSiO₃ HHSs. Heat treatment in air at 700 °C of the CuSiO₃ HHSs led to formation of CuO@SiO₂ HHSs with conserving morphological features of CuSiO₃ HHSs. Cu₃N@SiO₂ HHSs were obtained by reaction of CuSiO₃ HHSs with gaseous ammonia at 350 °C in a horizontal tube furnace. All experimental details are given in section 6.3.5. The morphology of Cu₃N@SiO₂ HHSs consists of Cu₃N nanoparticles on the surface of SiO₂ hierarchical hollow shell.

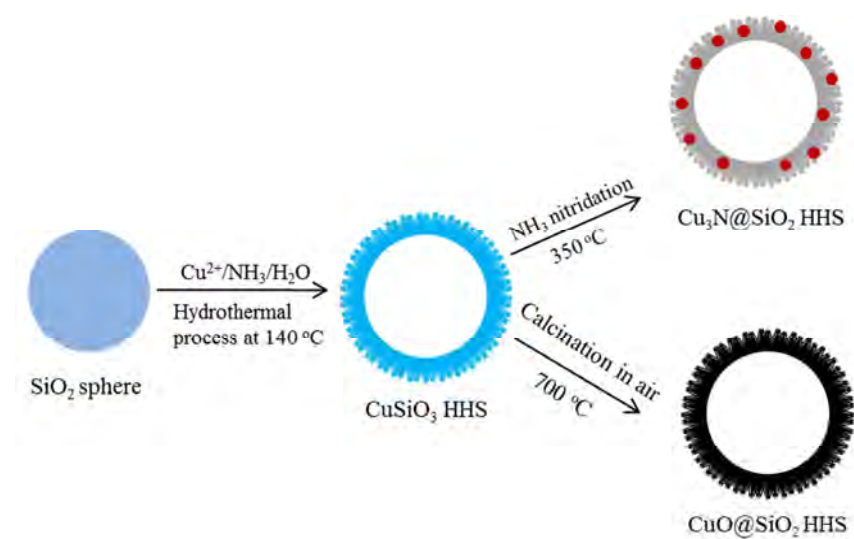


Fig. 4.6 Synthesis of CuO@SiO₂ and Cu₃N@SiO₂ HHSs using colloidal Stöber silica spheres via CuSiO₃ HHSs.

The SEM image of Stöber silica spheres synthesized by hydrolysis and condensation of TEOS in alkaline media shows monodisperse spheres with an average diameter of 700 nm (Fig. 4.7).

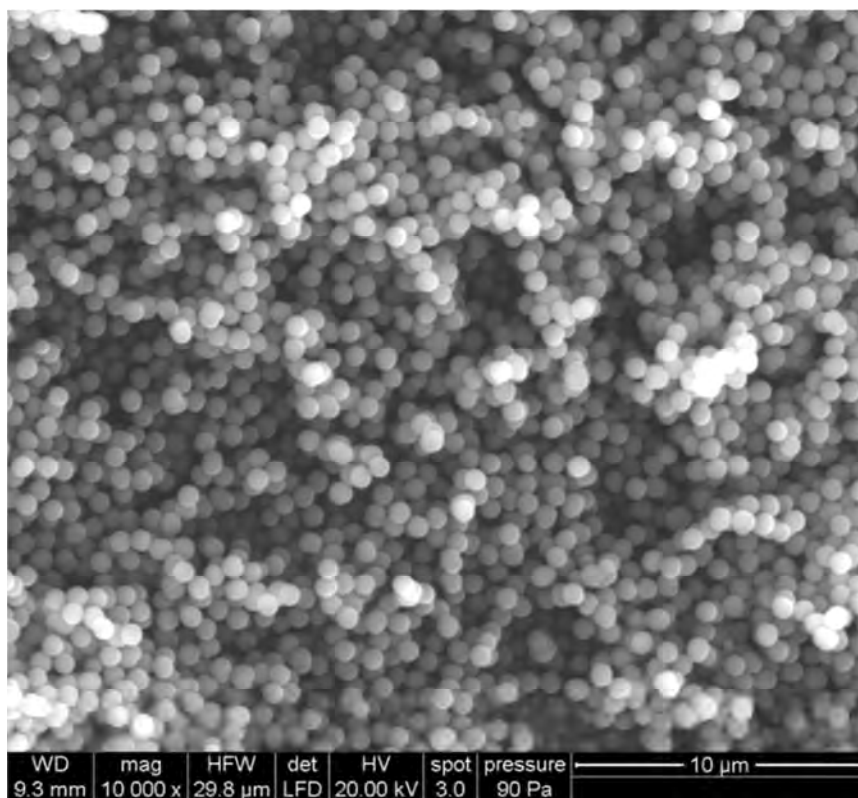


Fig. 4.7 SEM image of silica spheres synthesized by Stöbers process.

The XRD pattern of CuSiO_3 HHSs (Fig. 4.8 e) shows clear evidence for copper silicate formation (JCPDS 03-0219). The broadening of peaks clearly reveals that the material is nanocrystalline. Fig. 4.8 a, b shows the TEM images of CuSiO_3 consisting of predominantly uniform hierarchical hollow spheres. A closer look at these structures (Fig. 4.8 c, d) shows that the sphere is composed of a large number of nanotubes. Most of the nanotubes are arranged vertically on the surface of the sphere. These hierarchical hollow structures are in accordance to the structures reported by Wang et al.³⁸.

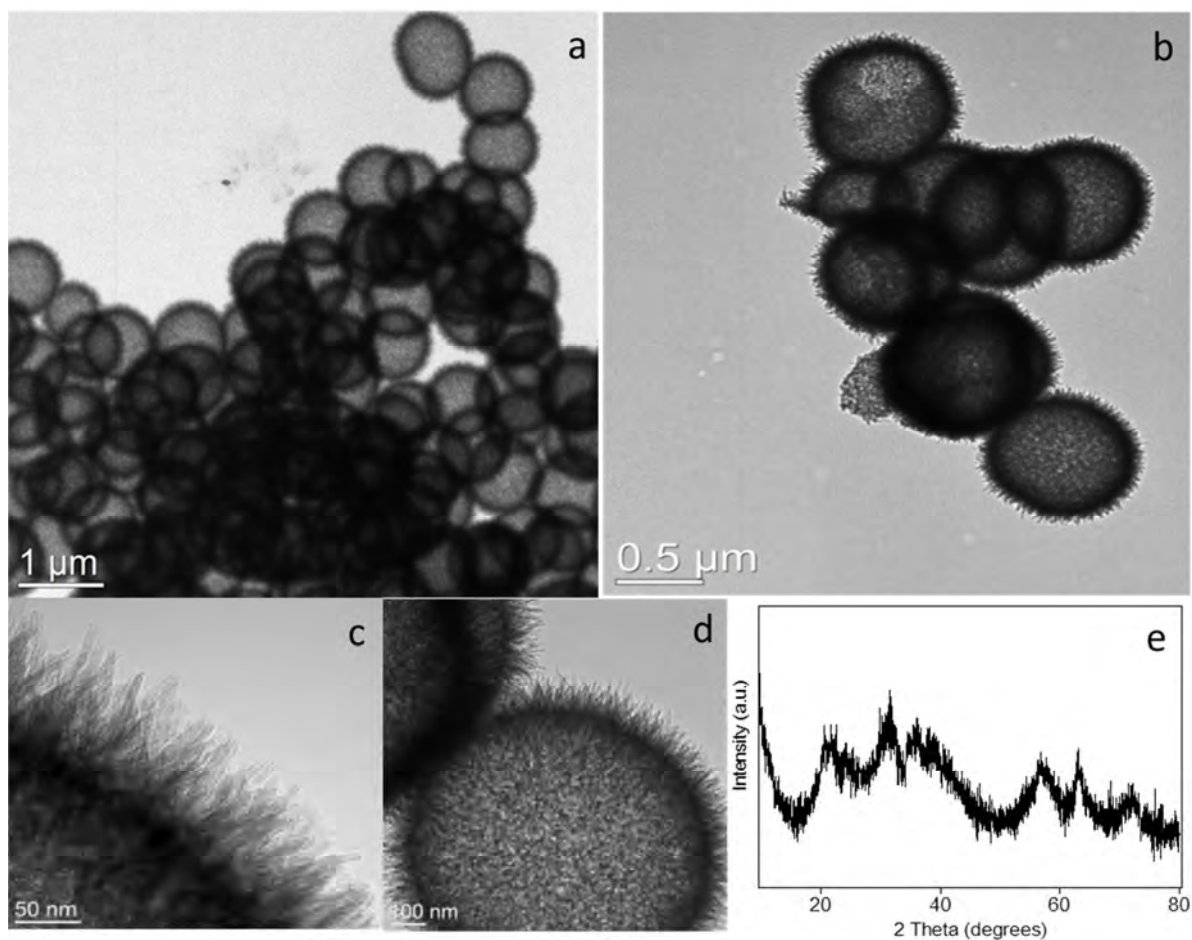


Fig. 4.8 TEM images (a,b,c,d) and XRD pattern (e) of CuSiO_3 HHSs.

Heat treatment of CuSiO_3 HHSs at $700\text{ }^\circ\text{C}$ in air leads to formation of CuO@SiO_2 HHSs through disintegration of the copper silicate framework. The blue colour of CuSiO_3 HHSs was changed to black after heat treatment. The XRD pattern (Fig. 4.9 a) shows clear evidence for monoclinic CuO nanocrystals formation (JCPDS 41-0254) along with a broad hump at < 30 degrees due to amorphous silica. The crystallite size of CuO crystals in CuO@SiO_2 determined by the Scherrer equation is 10 nm. Heat treatment of CuSiO_3 HHSs below $700\text{ }^\circ\text{C}$ gave no evidence for CuO phase formation as confirmed by XRD (XRD not shown). The surface area and pore size distribution of CuO@SiO_2 HHSs are $181\text{ m}^2/\text{g}$ and 3 nm respectively (Fig. 4.9 b).

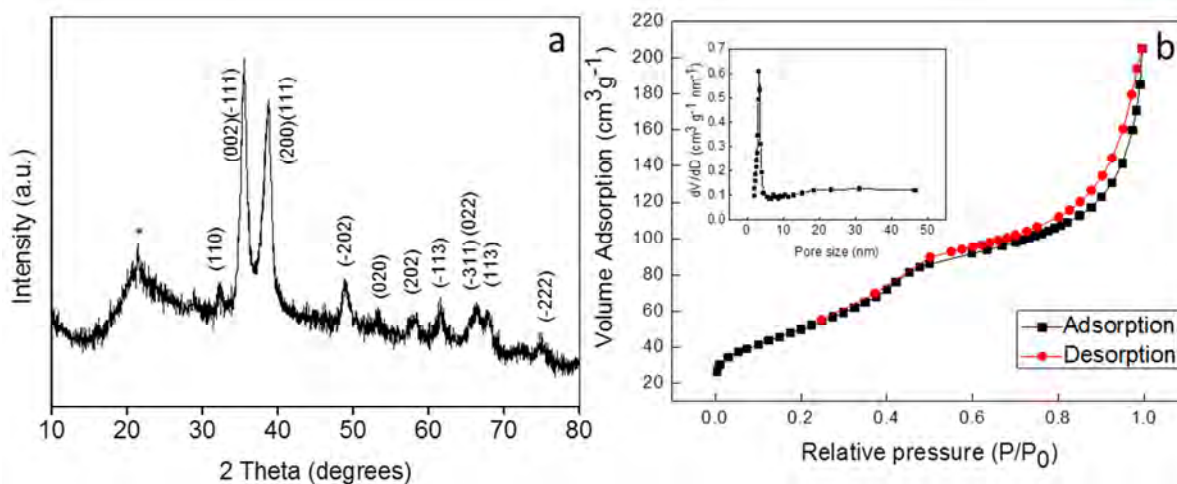


Fig. 4.9 XRD pattern (a) and N_2 adsorption/desorption isotherm (Inset – pore size distribution from adsorption branch of isotherm) (b) of $CuO@SiO_2$ HHSs. (* cristobalite)

The SEM (Fig. 4.10), and TEM (Fig. 4.11 a, b) images clearly show that the morphology of $CuO@SiO_2$ is almost similar to that of the $CuSiO_3$ HHSs precursor. The high magnification TEM image of $CuO@SiO_2$ (Fig. 4.11 c) revealed that CuO nanoparticles, which are marked by arrows, are bestrewed on the hierarchical hollow silica shells. The corresponding SAED pattern, as shown in Fig. 4.11 d, further suggested the formation of CuO particles. The diffraction rings on SAED image clearly represent the (-111), (111), (200), (022) and (-311) planes of monoclinic CuO . The investigation of composition of nanotubular structures in $CuO@SiO_2$ HHSs by electron microscopy was not successful as the nanotubes were easily deformed by the electron beam during the analysis.

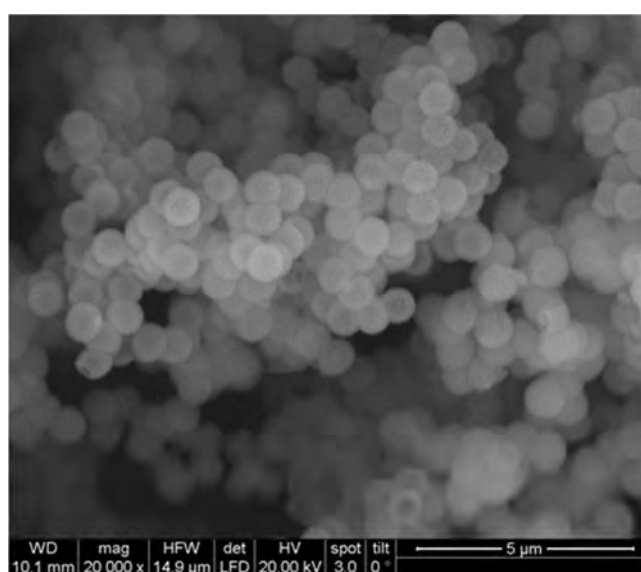


Fig. 4.10 SEM image of $CuO@SiO_2$

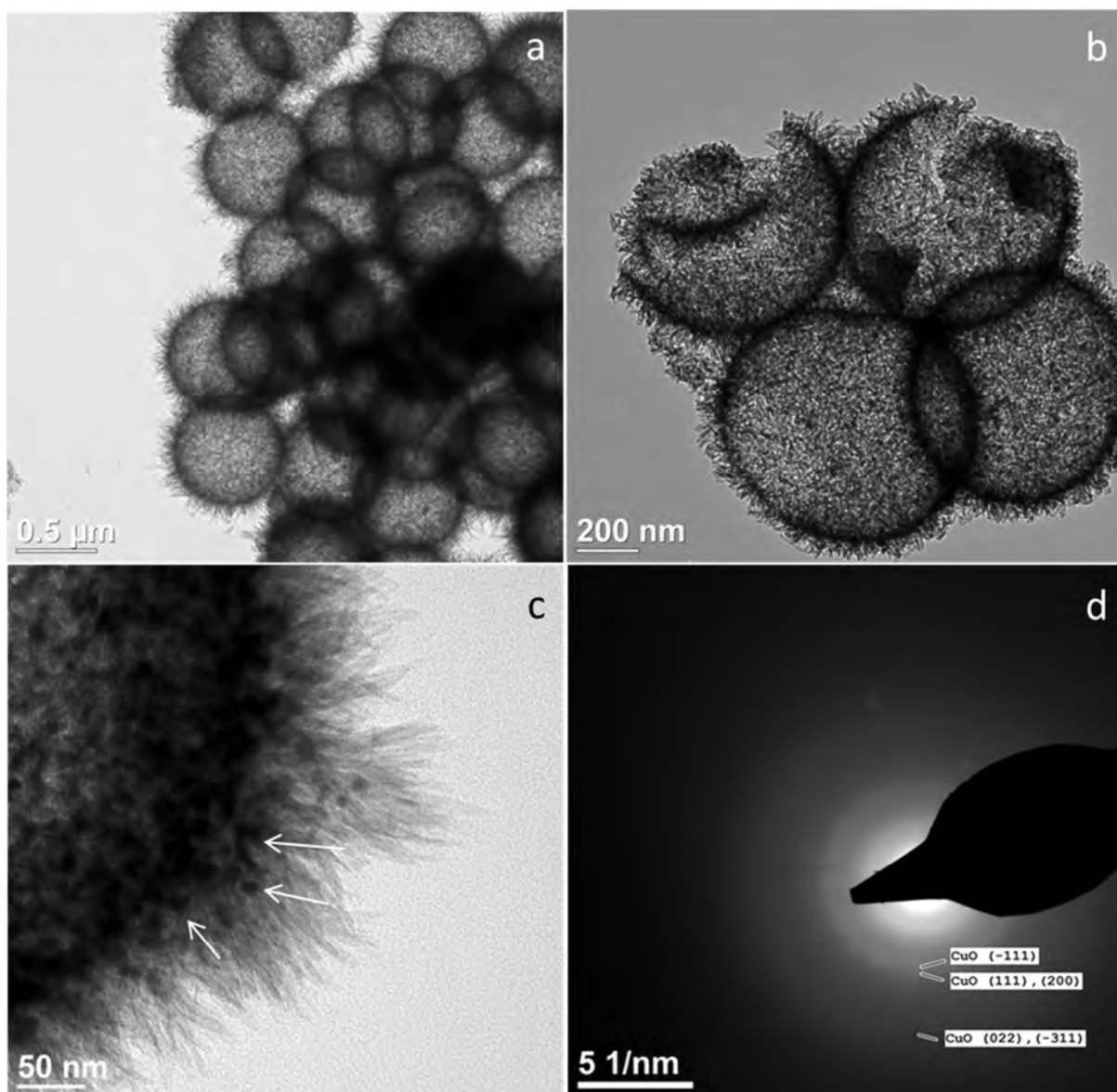


Fig. 4.11 TEM images of CuO@SiO₂ HHSs (a, b), high magnification TEM image of the CuO@SiO₂ HHS (c) and the corresponding SAED pattern (d).

Nitridation of CuSiO₃ HHSs at 350 °C for 1 h gave a brown powder. XRD analysis of the product (Fig. 4.12a) showed the presence of cubic Cu₃N nanocrystals (JCPDS-86-2283) and amorphous silica. The crystallite size of Cu₃N crystals was 31 nm, as calculated by the Scherrer equation. The XRD clearly indicates complete phase conversion from CuSiO₃ to Cu₃N@SiO₂.

The nitrogen adsorption and desorption isotherm of Cu₃N@SiO₂ HHSs is shown in Fig. 4.12 b. The BET surface area was 159 m²/g. The pore size distribution from the adsorption branch of the isotherm is centred at 3-4 nm (inset of Fig. 4.12 b).

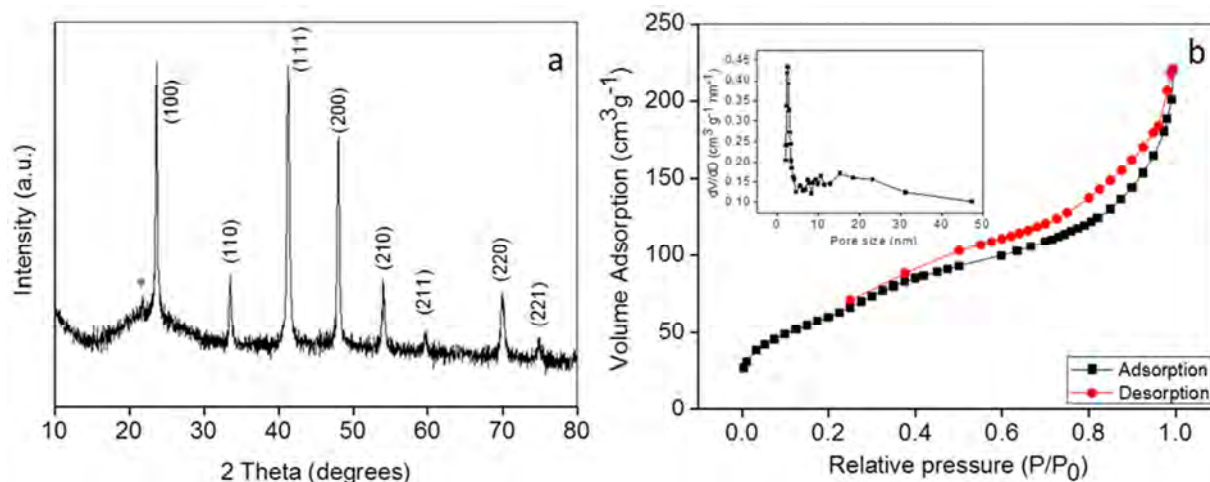


Fig. 4.12 XRD pattern (a) and N₂ adsorption/desorption isotherm (Inset – pore size distribution from adsorption branch of isotherm) (b) of Cu₃N@SiO₂ HHSs. (* cristobalite)

SEM analysis (Fig. 4.13) of the Cu₃N@SiO₂ HHSs showed bright spots on the surface of HHSs. Further investigation by TEM clearly showed Cu₃N nanoparticles on the surface of the hierarchical hollow silica shells (Fig. 4.14). This is clear evidence that during the nitridation reaction copper species migrated on the surface creating large agglomerated Cu₃N nanoparticles on the hollow silica shell. The CuSiO₃ HHSs were converted directly to Cu₃N nanoparticles through the nitridation reaction.

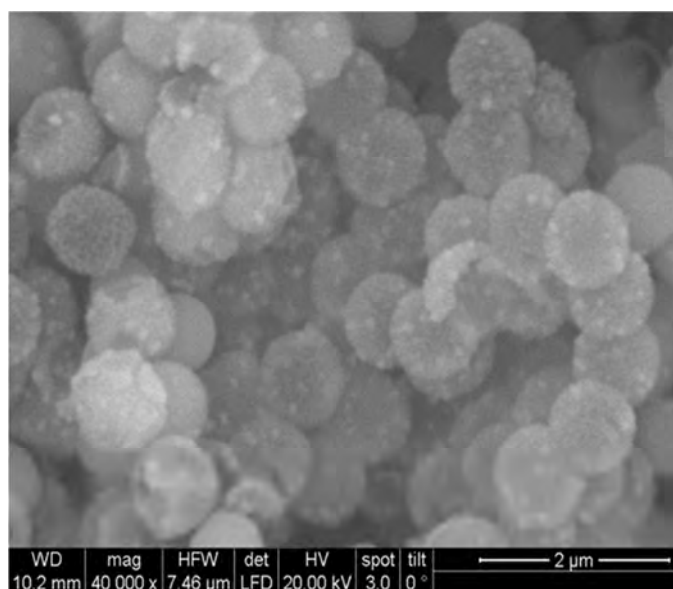


Fig. 4.13 SEM image of Cu₃N@SiO₂ HHSs.

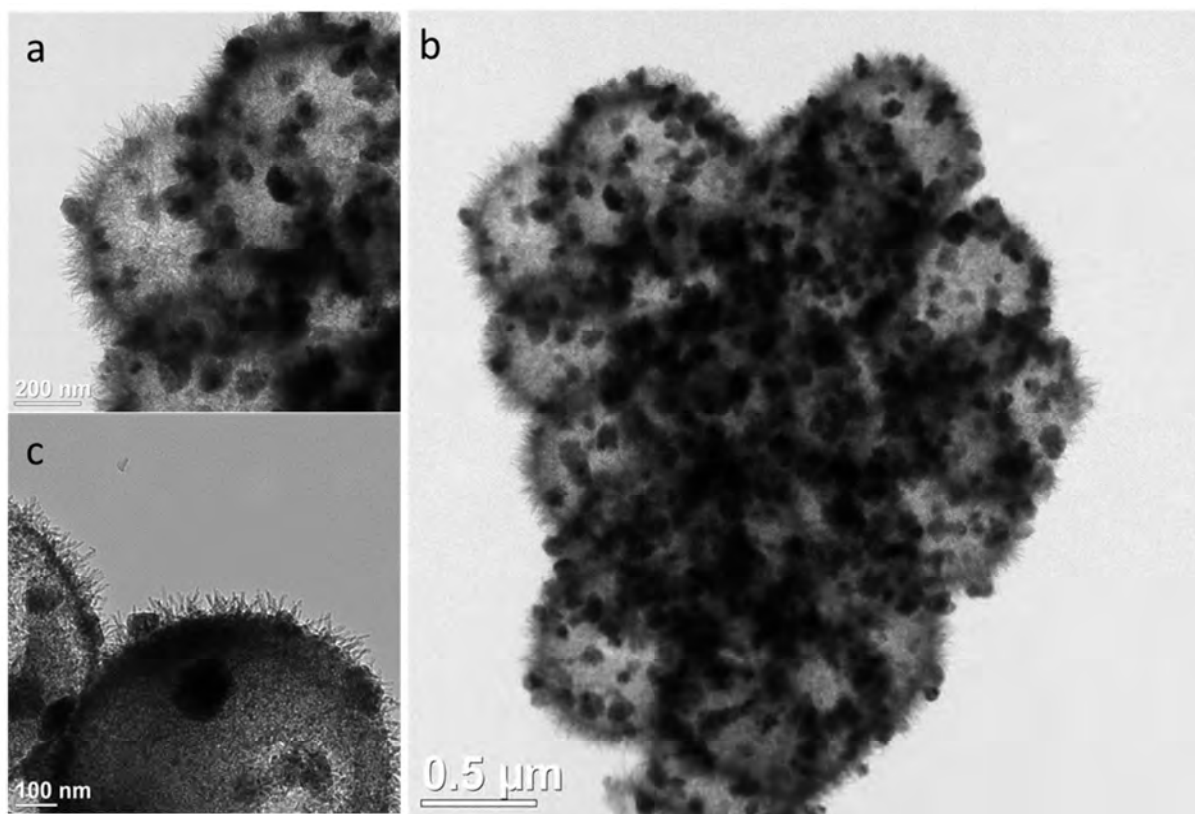


Fig. 4.14 TEM image of $\text{Cu}_3\text{N}@\text{SiO}_2$ HHSs.

4.2 Conclusion

In conclusion, $\text{CuO}@\text{SiO}_2$ and $\text{Cu}_3\text{N}@\text{SiO}_2$ HHSs were synthesized from a CuSiO_3 HHSs precursor. CuSiO_3 HHSs were disintegrated into CuO nanoparticles dispersed on SiO_2 HHSs by heat treatment at 700 °C. Moreover, CuSiO_3 HHSs were converted into Cu_3N nanoparticles embedded on SiO_2 HHSs by direct ammonia nitridation reaction at 350 °C. The conversion of CuSiO_3 HHSs to $\text{CuO}@\text{SiO}_2$ and $\text{Cu}_3\text{N}@\text{SiO}_2$ HHSs is a new observation. The present results show that direct ammonia nitridation and thermal disintegration of CuSiO_3 HHSs is a feasible reaction and could also be applied to synthesize other metal oxide@silica and metal nitride@silica composite materials.

4.3 References

1. Zhao, Y.; Jiang, L. *Advanced Materials* **2009**, 21, (36), 3621-3638.
2. Zeng, H. C. *Journal of Materials Chemistry* **2011**, 21, (21), 7511-7526.
3. Lou, X. W.; Archer, L. A.; Yang, Z. C. *Advanced Materials* **2008**, 20, (21), 3987-4019.
4. Hu, J.; Chen, M.; Fang, X. S.; Wu, L. W. *Chemical Society Reviews* **2011**, 40, (11), 5472-5491.
5. Lai, X. Y.; Halpert, J. E.; Wang, D. *Energy & Environmental Science* **2012**, 5, (2), 5604-5618.
6. Liu, Z.; Li, M.; Yang, X.; Yin, M.; Ren, J.; Qu, X. *Biomaterials* **2011**, 32, (21), 4683-90.
7. Xiao, F. S.; Han, Y.; Yu, Y.; Meng, X. J.; Yang, M.; Wu, S. *Journal of the American Chemical Society* **2002**, 124, (6), 888-889.
8. Wang, X.; Zhuang, J.; Chen, J.; Zhou, K. B.; Li, Y. D. *Angewandte Chemie-International Edition* **2004**, 43, (15), 2017-2020.
9. Zhuang, Y.; Yang, Y.; Xiang, G. L.; Wang, X. *Journal of Physical Chemistry C* **2009**, 113, (24), 10441-10445.
10. Chen, H. M.; Lu, X. H.; Deng, C. H.; Yan, X. M. *Journal of Physical Chemistry C* **2009**, 113, (50), 21068-21073.
11. Fan, F. L.; Ding, H. J.; Bai, J.; Wu, X. L.; Lei, F.; Tian, W.; Wang, Y.; Qin, Z. *Journal of Radioanalytical and Nuclear Chemistry* **2011**, 289, (2), 367-374.
12. Wang, Y. Q.; Wang, G. Z.; Wang, H. Q.; Liang, C. H.; Cai, W. P.; Zhang, L. D. *Chemistry-a European Journal* **2010**, 16, (11), 3497-3503.
13. Zheng, J.; Wu, B. H.; Jiang, Z. Y.; Kuang, Q.; Fang, X. L.; Xie, Z. X.; Huang, R. B.; Zheng, L. S. *Chemistry-an Asian Journal* **2010**, 5, (6), 1439-1444.
14. Guo, Z. Y.; Du, F. L.; Li, G. C.; Cui, Z. L. *Chemical Communications* **2008**, (25), 2911-2913.
15. Zhu, T.; Wang, Z. Y.; Ding, S. J.; Chen, J. S.; Lou, X. W. *Rsc Advances* **2011**, 1, (3), 397-400.
16. Jin, P.; Chen, Q. W.; Hao, L. Q.; Tian, R. F.; Zhang, L. X.; Wang, L. *Journal of Physical Chemistry B* **2004**, 108, (20), 6311-6314.
17. Park, J. C.; Lee, H. J.; Bang, J. U.; Park, K. H.; Song, H. *Chemical Communications* **2009**, (47), 7345-7347.

18. Zhu, T.; Xia, B. Y.; Zhou, L.; Lou, X. W. *Journal of Materials Chemistry* **2012**, *22*, (16), 7851-7855.
19. Yao, K. X.; Zeng, H. C. *Chemistry of Materials* **2012**, *24*, (1), 140-148.
20. Tan, M. Q.; Munusarny, P.; Mahalingam, V.; van Veggel, F. C. J. M. *Journal of the American Chemical Society* **2007**, *129*, (46), 14122-14123.
21. Du, X.; He, J. H. *Nanoscale* **2011**, *3*, (10), 3984-4002.
22. Jansat, S.; Pelzer, K.; Garcia-Anton, J.; Raucoules, R.; Philippot, K.; Maisonnat, A.; Chaudret, B.; Guari, Y.; Mehdi, A.; Reye, C.; Corriu, R. J. R. *Advanced Functional Materials* **2007**, *17*, (16), 3339-3347.
23. Chen, Z.; Cui, Z. M.; Niu, F.; Jiang, L.; Song, W. G. *Chemical Communications* **2010**, *46*, (35), 6524-6526.
24. Shin, J. M.; Kim, H.; Lee, I. S. *Chemical Communications* **2008**, (43), 5553-5555.
25. Liu, J.; Qiao, S. Z.; Hu, Q. H.; Lu, G. Q. *Small* **2011**, *7*, (4), 425-443.
26. Joo, S. H.; Park, J. Y.; Tsung, C. K.; Yamada, Y.; Yang, P. D.; Somorjai, G. A. *Nature materials* **2009**, *8*, (2), 126-131.
27. Liu, S. H.; Han, M. Y. *Advanced Functional Materials* **2005**, *15*, (6), 961-967.
28. Ding, S. J.; Chen, J. S.; Qi, G. G.; Duan, X. N.; Wang, Z. Y.; Giannelis, E. P.; Archer, L. A.; Lou, X. W. *Journal of the American Chemical Society* **2011**, *133*, (1), 21-23.
29. Shen, G.; Chen, P. C.; Ryu, K.; Zhou, C. *Journal of Materials Chemistry* **2009**, *19*, (7), 828-839.
30. Polshettiwar, V.; Baruwati, B.; Varma, R. S. *Acs Nano* **2009**, *3*, (3), 728-736.
31. Feng, X. J.; LaTempa, T. J.; Basham, J. I.; Mor, G. K.; Varghese, O. K.; Grimes, C. A. *Nano Letters* **2010**, *10*, (3), 948-952.
32. Wu, H. B.; Chen, W. *Journal of the American Chemical Society* **2011**, *133*, (39), 15236-15239.
33. Rout, L.; Sen, T. K.; Punniyamurthy, T. *Angewandte Chemie-International Edition* **2007**, *46*, (29), 5583-5586.
34. Kim, J. Y.; Park, J. C.; Kang, H.; Song, H.; Park, K. H. *Chemical Communications* **2010**, *46*, (3), 439-441.
35. Gou, X. L.; Wang, G. X.; Yang, J. S.; Park, J.; Wexler, D. *Journal of Materials Chemistry* **2008**, *18*, (9), 965-969.
36. Zhang, Z. H.; Wang, P. *Journal of Materials Chemistry* **2012**, *22*, (6), 2456-2464.

37. Lee, B. S.; Yi, M.; Chu, S. Y.; Lee, J. Y.; Kwon, H. R.; Lee, K. R.; Kang, D.; Kim, W. S.; Bin Lim, H.; Lee, J.; Youn, H. J.; Chi, D. Y.; Hur, N. H. *Chemical Communications* **2010**, 46, (22), 3935-3937.
38. Wang, Y. Q.; Wang, G. Z.; Wang, H. Q.; Cai, W. P.; Zhang, L. D. *Chemical Communications* **2008**, (48), 6555-6557.
39. Stober, W.; Fink, A.; Bohn, E. *Journal of Colloid and Interface Science* **1968**, 26, (1), 62-69.

Chapter 5

Synthesis and Physical Properties of Strontium Titanate and Strontium Titanate/Strontium Carbonate Composites

Today, most of the energy we use is discharged as waste heat into the environment. Home heating, automotive exhaust, and industrial processes all generate an enormous amount of unused waste heat. Thermoelectric generators have potential to transform a heat flow into electricity^{1,2}. Thermoelectric phenomena, which involve the conversion between thermal and electrical energy, and provide a method for heating and cooling materials, are expected to play an increasingly important role in meeting the energy challenge of the future³.

The efficiency of the thermoelectric material is expressed as a “thermoelectric figure of merit,” ZT , which is a dimensionless figure derived from several factors including the electrical conductivity and thermal conductivity.

$$ZT = S^2 \cdot \sigma \cdot T \cdot \kappa^{-1},$$

Where,

Z is a figure of merit

T is the absolute temperature

S Seebeck coefficient

σ electrical conductivity

κ thermal conductivity

The figure of merit needs to be greater than 1.5 for the material to be capable of generating useful amounts of electricity in commercial applications^{2, 4}. In order to optimize the figure of merit, phonons, which are responsible for thermal conductivity, must experience the material as a glass (high degree of phonon scattering, lowering thermal conductivity) while electrons must experience the material as a crystal (very little scattering, maintaining electrical conductivity)⁵. The figure of merit can be improved through the independent adjustment of these properties.

For efficient thermoelectric materials, three physical properties are required:

1. Low thermal conductivity (κ), which is required to create a large temperature difference between the ends of the material;
2. High electrical conductivity (σ), which is required to reduce the internal resistance of the material; and
3. A large thermo-electromotive force (Seebeck coefficient S), which is required to obtain high voltage.

Thermal conductivity (κ) in thermoelectrics has two origins:

- (1) Electrons and holes transporting heat (κ_{electron}) and
- (2) Phonons travelling through the lattice (κ_{phonon}).

$$\kappa = \kappa_{\text{electron}} + \kappa_{\text{phonon}}$$

According to the Wiedemann-Franz law, the higher electrical conductivity, the higher κ_{electron} becomes⁶. Therefore, it is necessary to minimize κ_{phonon} . Good thermoelectrics are crystalline materials that scatter phonons without significantly disrupting the electrical conductivity.

There are different strategies to reduce lattice thermal conductivity by clever tuning of the scattering mechanisms of the heat carrying phonons⁷⁻⁹.

1. The first is to scatter phonons within the unit cell by creating point defects, rattling structures or vacancies.
e.g. clathrates or filled skutterudites
2. The second strategy is to use complex crystals to separate the electron-crystal from the phonon-glass. The region responsible for electron transport would be an electron-crystal of a high-mobility semiconductor, while the phonon-glass would ideally consist of disordered structures and dopants without disrupting the electron-crystal.
e.g. complex “hybrid” oxides
3. Multiphase nanocomposites: A third strategy is to scatter phonons at the interfaces of nanostructured materials, leading to multiphase composites mixed on the nanometre

scale. These nanostructured materials can be formed as thin-film superlattices or as intimately mixed composite structures.

There are several materials under consideration for thermoelectric device applications. At temperatures below 500 K, the best commercially available inorganic semiconductors are bismuth telluride (Bi_2Te_3)-based alloys, which possess a figure of merit ZT close to one^{10, 11}. For mid-temperature power generation (500-900 K), materials based on group-IV tellurides are typically used, such as PbTe , GeTe or SnTe ^{12, 13}. However, these materials are not attractive for applications, particularly at high temperatures ($T \sim 1000$ K), because decomposition, vaporization, or melting of the constituents can easily occur. Further, the use of these heavy metals should be limited to specific environments such as space, because they are mostly toxic, low in natural abundance, and thus not environmentally benign¹⁴.

Metal oxide-based thermoelectric materials are of great importance for thermoelectric power generation at high temperatures because of their greater chemical and thermal robustness, as compared to conventional high- ZT bismuth compounds¹⁵⁻¹⁸. In addition to thermal stability, other advantages of oxides are their nontoxicity and high oxidation resistance. However, the figure of merit in oxides is relatively low¹⁹. Among metal oxides, crystalline SrTiO_3 is a promising thermoelectric material, particularly at high temperatures¹⁸. SrTiO_3 is a well-known oxide with a cubic perovskite structure (lattice parameter $a = 3.905$ Å). The melting point of SrTiO_3 is 2080 °C, making it applicable at high temperatures. All the constituents of SrTiO_3 are naturally abundant. The electrical conductivity in SrTiO_3 can be easily tuned from insulating to metallic by substitutional doping with La^{3+} or Nb^{5+} ¹⁴.

In this study $(\text{SrTiO}_3)_{1-x}(\text{SrCO}_3)_x$ ($x = 0, 0.22, 0.31, 0.45$) composites and $\text{SrTi}_{0.8}\text{Nb}_{0.2}\text{O}_3$ were synthesized and characterised, and further investigated for physical properties. It was believed that SrCO_3 in $\text{SrTiO}_3/\text{SrCO}_3$ composites would help to scatter phonons hence reduce thermal diffusivity. All physical measurements were performed by Matthias Ekedá, doctoral student working under supervision of Prof. Silke Bühler-Paschen at TU Wien.

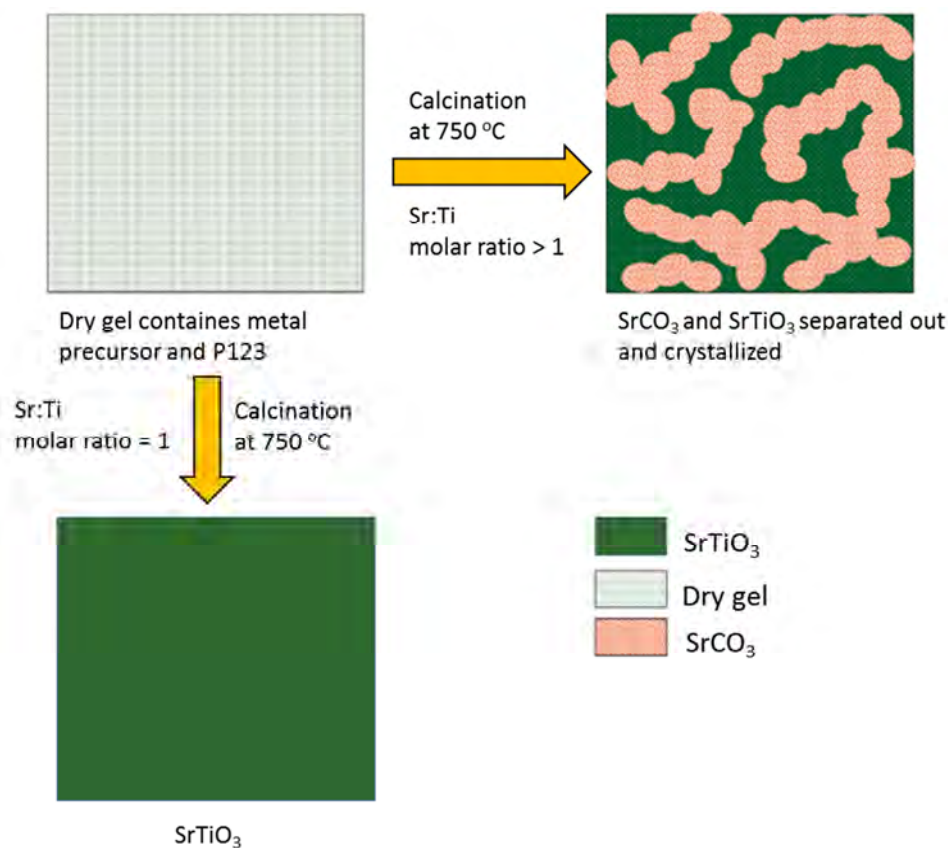
5.1 Results and Discussion

The main aim of this study was to investigate porous SrTiO₃-based materials for thermoelectric application. The reason behind creating porosity in the SrTiO₃ material was to achieve lower thermal conductivity by scattering phonons by the void spaces of the pores and simultaneously maintaining the electron transport through the pore walls. The electrical conductivity in SrTiO₃ can be easily tuned from insulating to metallic by substitutional doping with La³⁺ or Nb⁵⁺. Thus by employing porous SrTiO₃-based materials lower thermal conductivity along with higher electrical transport was expected. However, powder samples were not suitable for physical property measurements and powders must be compressed in pellets, which would collapse the porosity in the materials. Hence the original idea of employing porous SrTiO₃ based materials was changed to SrTiO₃/SrCO₃ composites. It was believed that SrCO₃ in SrTiO₃/SrCO₃ composites would help to scatter phonons and hence reduce the thermal conductivity.

5.1.1 SrTiO₃ and SrTiO₃/SrCO₃ Composites

A method described by Fan et al. was used to synthesize SrTiO₃ and SrTiO₃/SrCO₃ composites with slight modifications²⁰. For SrTiO₃ synthesis the molar ratio of strontium: titanium was 1:1, whereas for SrTiO₃/SrCO₃ composites synthesis, the strontium metal precursor was taken in excess compared to the titanium precursor (molar ratio of Sr: Ti was 1.3:1, 1.6:1, and 2:1). The excess strontium precursor partly reacts with the titanium precursor to form SrTiO₃ and partly converts into nanoscale SrCO₃ grains dispersed in the sample after the calcination step.

The strategy for the synthesis of SrTiO₃ and SrTiO₃/SrCO₃ composites is represented in scheme 1.



Scheme 1. Synthesis of SrTiO₃ and SrCO₃/SrTiO₃ composites.

The molar ratio of Sr:Ti was 1:1, 1.3:1, 1.6:1 and 2:1 for the synthesis of (SrTiO₃)_{1-x}(SrCO₃)_x ($x = 0, 0.22, 0.31, 0.45$). The compositions of (SrTiO₃)_{1-x}(SrCO₃)_x composites, where $x = 0, 0.22, 0.31, 0.45$, were calculated using quantitative XRD analysis using Rietveld refinement method.

The detailed synthesis procedure is given in section 6.3.6.1. Dissolution of SrCO₃ in acetic acid/H₂O mixture forms in situ Sr(CH₃COO)₂, that undergoes sol-gel reaction with titanium tetrabutoxide in the presence of the P123 surfactant. P123 is a triblock copolymer, HO(CH₂CH₂O)₂₀(CH₂CH(CH₃)O)₇₀(CH₂CH₂O)₂₀H, and was added to get a particulate gel (stabilisation of nanoparticles in the dry gel) and to protect the dry gel from phase separation. A multicomponent oxide nanoparticles precursor is formed in which Sr and Ti is interconnected via oxo/acetate bridges. Dry gels were obtained after solvent evaporation. The formation of SrCO₃/SrTiO₃ composites during calcination of the dry gels can be explained in

a way that SrCO_3 re-formed during the oxidative degradation of the organic compounds reacts with TiO_2 leading to formation of SrTiO_3 , and excess SrCO_3 remains dispersed in the sample.

TGA of the dry gels for $(\text{SrTiO}_3)_{1-x}(\text{SrCO}_3)_x$ ($x = 0, 0.22, 0.31, 0.45$) composites are shown in Fig. 5.1. The weight loss below 150°C is due to the loss of volatile species like H_2O , ethanol, butanol etc. At temperatures between 150°C to 550°C a major weight loss is due to decomposition of organic matter. Following TGA analysis, the dry gels were calcined in air at 750°C to remove organic moieties.

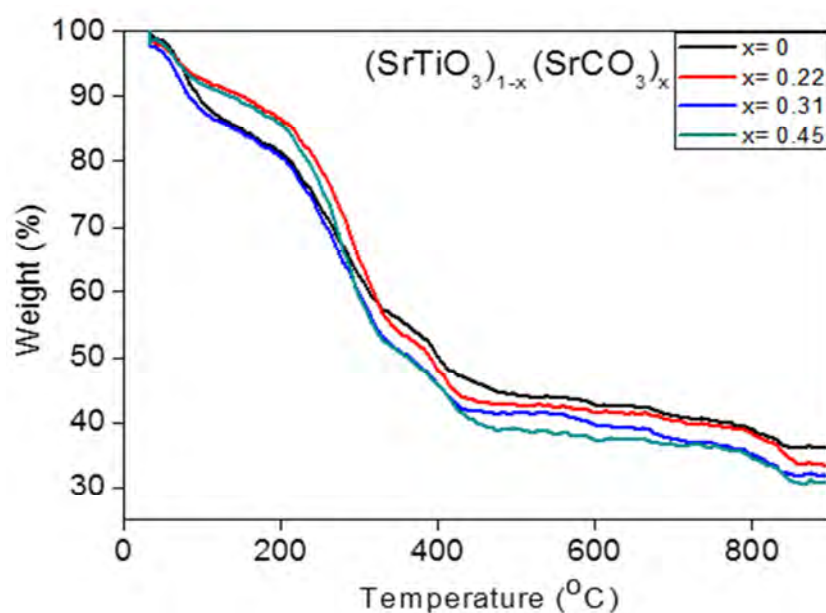


Fig. 5.1 Thermogravimetric analysis of precursor dry gel for $(\text{SrTiO}_3)_{1-x}(\text{SrCO}_3)_x$ ($x = 0, 0.22, 0.31, 0.45$) composites.

The powders obtained after calcination were analysed by XRD (Fig. 5.2) and further processed to obtain pellets for physical property measurements. Pellets obtained by using cold pressing of the $(\text{SrTiO}_3)_{1-x}(\text{SrCO}_3)_x$ composites were too brittle, and hence all samples were hot pressed at a pressure of 56 MPa and a temperature of 800°C for 2 hours. The density of $(\text{SrTiO}_3)_{1-x}(\text{SrCO}_3)_x$ composites was determined to be 48%, 52%, 54% and 60% of the theoretical density for $x = 0, 0.22, 0.31, 0.45$ respectively, which clearly shows that compaction worked out better with increasing SrCO_3 proportion.

The hot pressed samples were analysed by using XRD as shown in Fig. 5.2. The XRD analysis for the $x = 0$ sample showed phase pure SrTiO_3 in the cubic crystal system (JCPDS - 84-0444). The $(\text{SrTiO}_3)_{1-x}(\text{SrCO}_3)_x$ ($x = 0.22, 0.31, 0.45$) composites consisted of two phases, one corresponding to SrTiO_3 (♦) and other corresponding to SrCO_3 (●) with an orthorhombic

crystal system (JCPDS - 05-0418). The composites did not show any impurity phases after hot pressing.

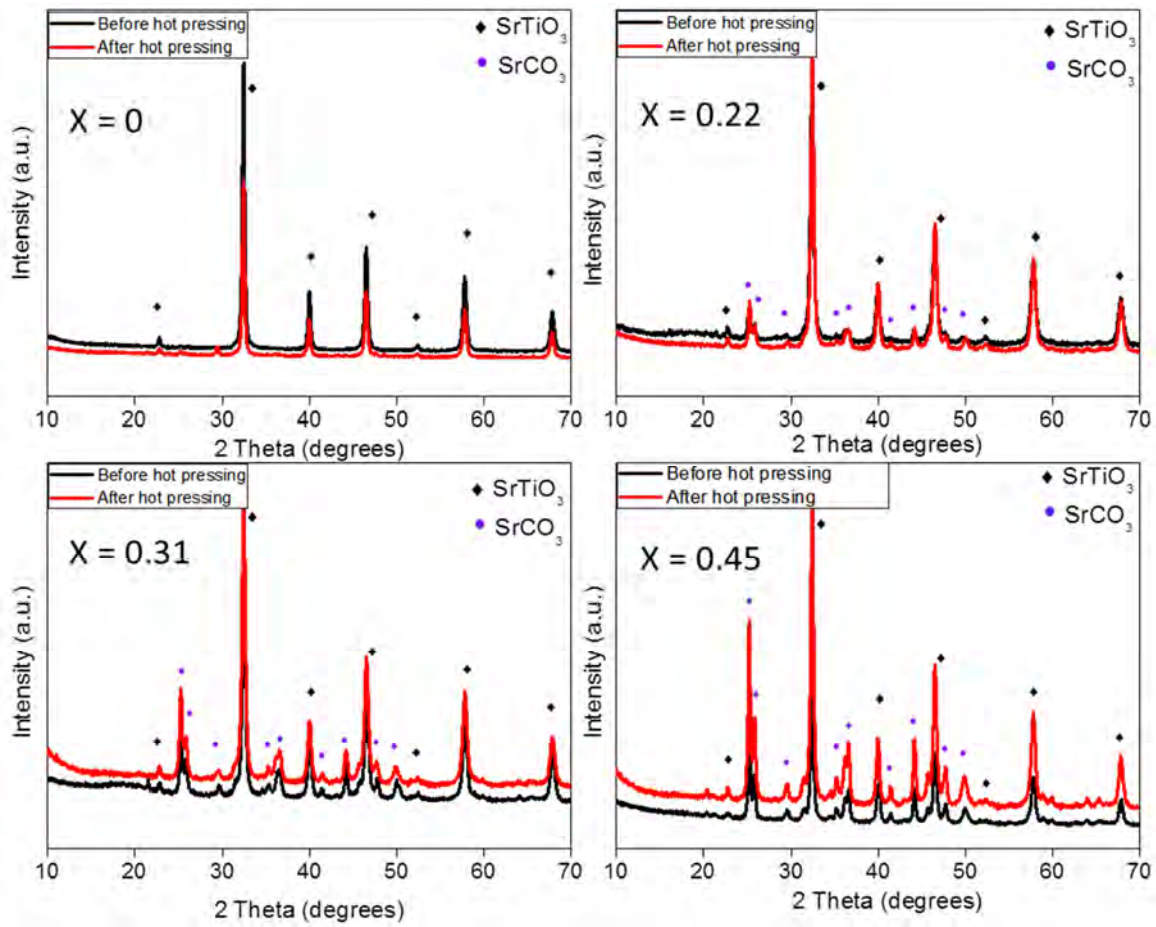


Fig. 5.2 XRD of $(\text{SrTiO}_3)_{1-x}(\text{SrCO}_3)_x$ ($x = 0, 0.22, 0.31, 0.45$) composites.

The hot pressed samples were powdered and placed on carbon grids for TEM analysis. Agglomerated particles were found for the $x = 0$ sample (Fig. 5.3).

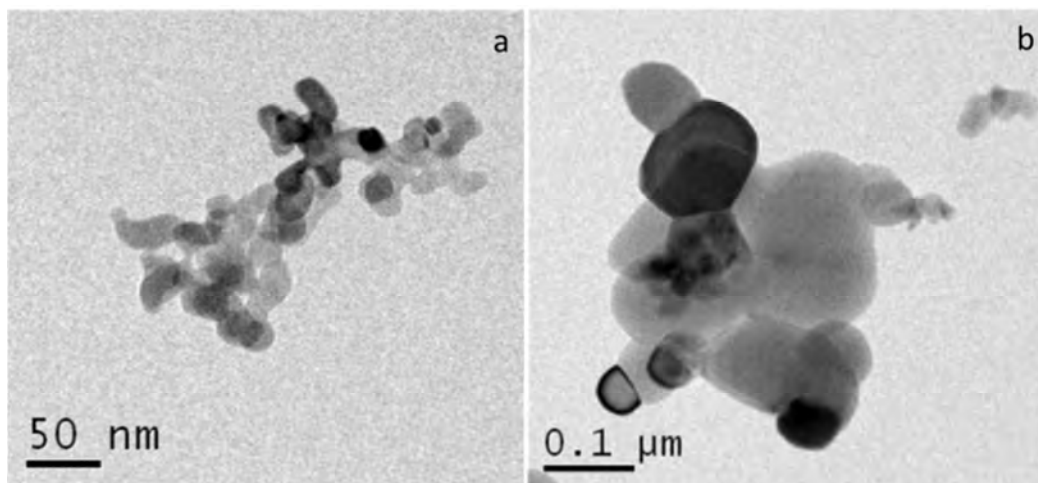


Fig. 5.3 TEM images of $(\text{SrTiO}_3)_{1-x}(\text{SrCO}_3)_x$ ($x = 0$).

The "amorphous rings" visible in the diffraction pattern (Fig. 5.4) belong to the graphite sample holder. The selected area electron diffraction (SAED) pattern revealed a lattice constant $a = 3.888 \text{ \AA}$ for SrTiO_3 .

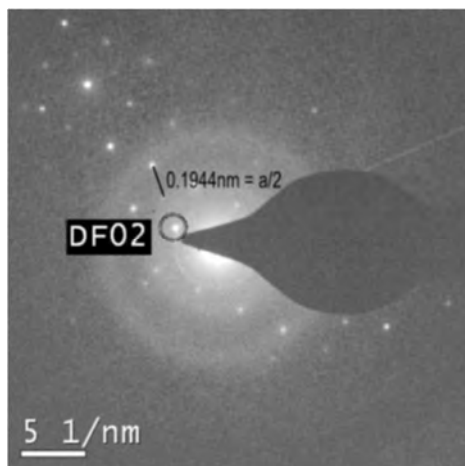


Fig. 5.4 SAED pattern of SrTiO_3 .

Agglomerated particles with diameters of around 50 nm were found for $(\text{SrTiO}_3)_{1-x}(\text{SrCO}_3)_x$ ($x = 0.22$) as shown in Fig. 5.5.

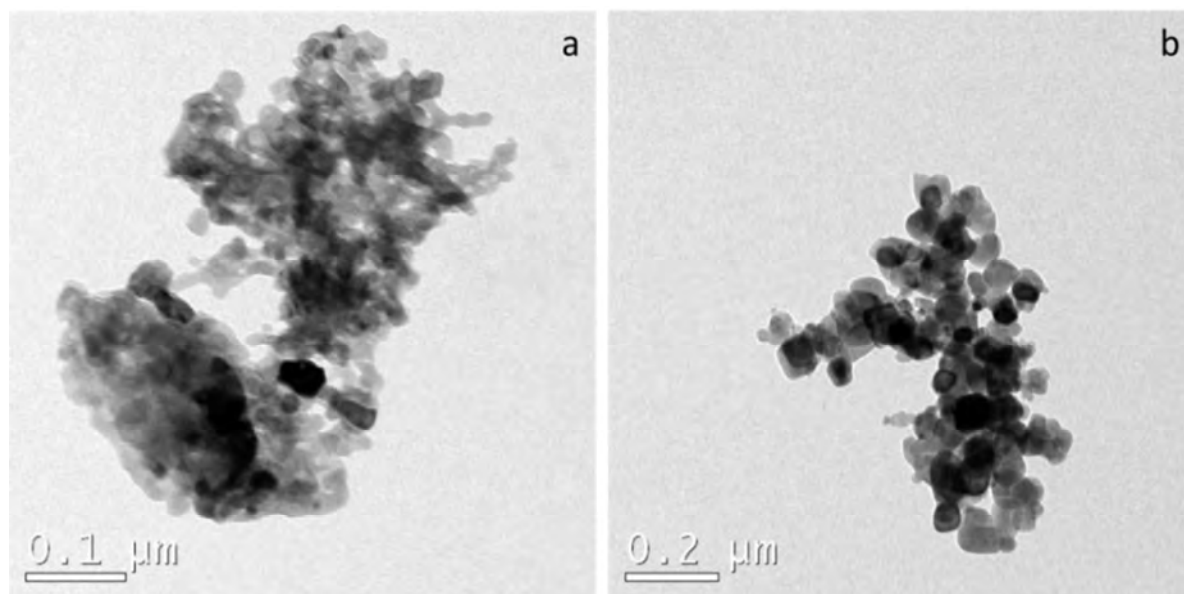


Fig. 5.5 TEM images of $(\text{SrTiO}_3)_{1-x}(\text{SrCO}_3)_x$ ($x = 0.22$).

5.1.2 SrTi_{0.8}Nb_{0.2}O₃

SrTiO₃ doped with Nb⁵⁺ was synthesized by following a very similar procedure as described for the SrTiO₃/SrCO₃ composites (section 5.1.1). The detailed experimental procedure is given in section 6.3.6.2. The XRD pattern of SrTi_{0.8}Nb_{0.2}O₃ showed characteristic peaks of the cubic perovskite structure of SrTiO₃ without any impurities from niobium oxide (Fig. 5.6).

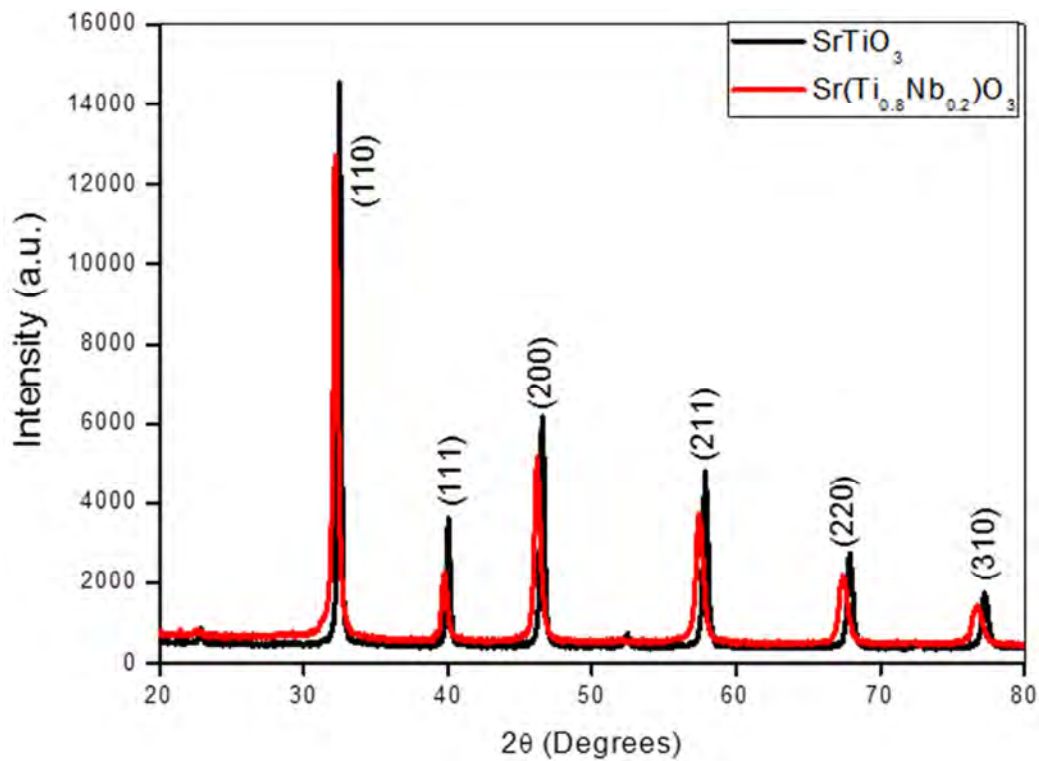


Fig. 5.6 XRD patterns of SrTiO₃ and SrTi_{0.8}Nb_{0.2}O₃.

The lattice parameters (*a*) calculated from the XRD patterns of SrTiO₃ and SrTi_{0.8}Nb_{0.2}O₃ were 3.905 and 3.923 Å respectively. SrTiO₃ has a similar lattice parameter compared with the literature value (3.905 Å)¹⁴. The lattice parameter of SrTi_{0.8}Nb_{0.2}O₃ is 0.46% larger than for SrTiO₃, possibly because the ionic radius of Nb⁵⁺ is (64.0 pm) larger than that of Ti⁴⁺ (60.5 pm)²¹. The position (2θ) of the reflections in SrTi_{0.8}Nb_{0.2}O₃ was shifted to smaller value compared to SrTiO₃. This is clear evidence for Nb doping (Fig. 5.7).

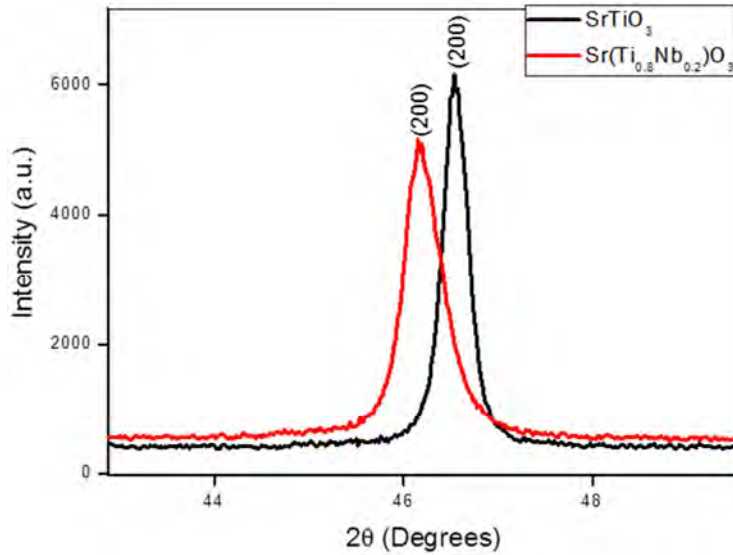


Fig. 5.7 The (200) reflection of SrTiO_3 and $\text{SrTi}_{0.8}\text{Nb}_{0.2}\text{O}_3$ (enlarged view)

5.1.3 Thermal Conductivity (κ) Measurements

The thermal diffusivity (α) was determined using a flash experiment (Anter, Flashline3000). Thermal diffusivity (α) was reduced for all $(\text{SrTiO}_3)_{1-x}(\text{SrCO}_3)_x$ composites by roughly a factor of 4 in comparison with literature data for single-crystalline SrTiO_3 ²⁴ (Fig. 5.8). A systematic dependence of the thermal diffusivity on the SrCO_3 proportion could not be observed.

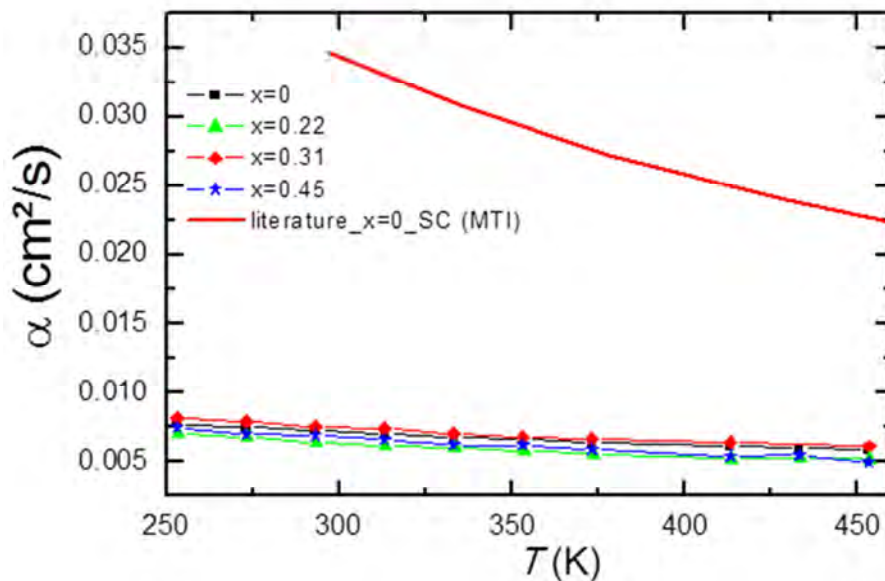


Fig. 5.8 Temperature dependence of thermal diffusivity for $(\text{SrTiO}_3)_{1-x}(\text{SrCO}_3)_x$; $x = 0, 0.22, 0.31, 0.45$ composites and literature data for single-crystalline (SC) SrTiO_3 .

The thermal conductivity (κ) below room temperature was measured using a standard steady-state heat-flow experiment. The thermal conductivity above room temperature was calculated according to the following equation

$$\kappa = C_p \cdot \alpha \cdot \rho$$

Where, ρ is the sample density.

C_p is specific heat capacity

α is thermal diffusivity

The thermal conductivities of all $(\text{SrTiO}_3)_{1-x}(\text{SrCO}_3)_x$ composites are found to be reduced by a factor of 10 compared with single crystal SrTiO_3 (Fig. 5.9).

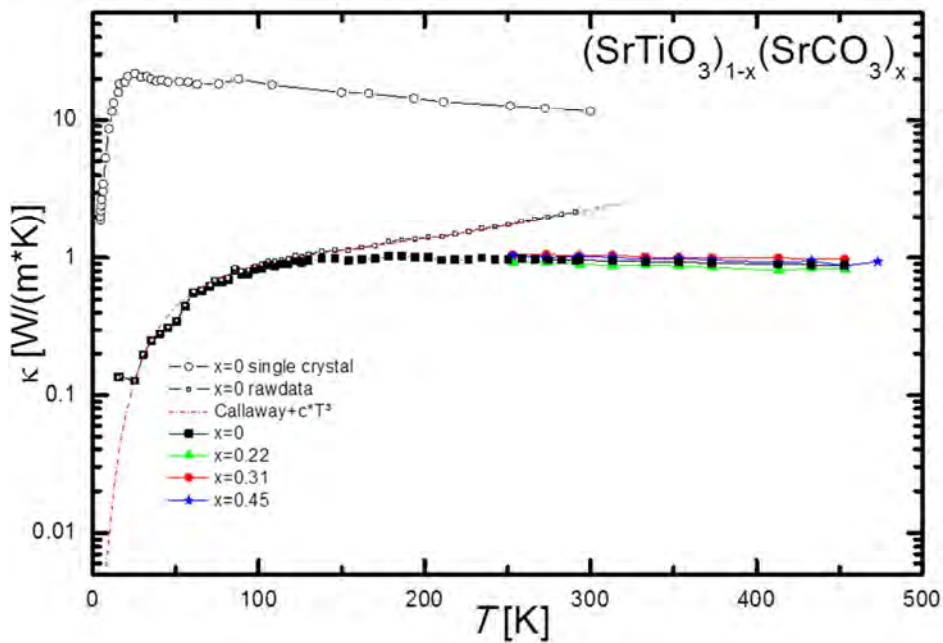


Fig. 5.9 Thermal conductivities of $(\text{SrTiO}_3)_{1-x}(\text{SrCO}_3)_x$ ($x = 0, 0.22, 0.31, 0.45$) composites compared with literature data for single-crystalline (SC) SrTiO_3 .

5.2 Conclusion

$(\text{SrTiO}_3)_{1-x}(\text{SrCO}_3)_x$ ($x = 0, 0.22, 0.31, 0.45$) composites were synthesized and investigated by thermal diffusivity and thermal conductivity measurements. The thermal diffusivities and thermal conductivities were significantly reduced for all composites in comparison with

literature data for single crystalline SrTiO_3 . The reason behind the reduction in thermal conductivity might be due to poor compaction of the composites after hot pressing, since no systematic dependence on the SrCO_3 content was observed. More insights are needed to understand the structure-property relationship in these composite materials.

5.3 References

1. Bell, L. E. *Science* **2008**, 321, (5895), 1457-1461.
2. Pei, Y. Z.; Shi, X. Y.; LaLonde, A.; Wang, H.; Chen, L. D.; Snyder, G. J. *Nature* **2011**, 473, (7345), 66-69.
3. Hochbaum, A. I.; Chen, R. K.; Delgado, R. D.; Liang, W. J.; Garnett, E. C.; Najarian, M.; Majumdar, A.; Yang, P. D. *Nature* **2008**, 451, (7175), 163-167.
4. Vining, C. B. *Nature materials* **2009**, 8, (2), 83-85.
5. Nolas, G. S.; Morelli, D. T.; Tritt, T. M. *Annual Review of Materials Science* **1999**, 29, 89-116.
6. Hashimoto, H.; Kusunose, T.; Sekino, T. *Journal of Ceramic Processing Research* **2011**, 12, (3), 223-227.
7. Snyder, G. J.; Toberer, E. S. *Nature materials* **2008**, 7, (2), 105-114.
8. Nielsch, K.; Bachmann, J.; Kimling, J.; Bottner, H. *Advanced Energy Materials* **2011**, 1, (5), 713-731.
9. Sootsman, J. R.; Chung, D. Y.; Kanatzidis, M. G. *Angewandte Chemie-International Edition* **2009**, 48, (46), 8616-8639.
10. Wright, D. A. *Nature* **1958**, 181, (4612), 834-834.
11. Goldsmid, H. J.; Douglas, R. W. *British Journal of Applied Physics* **1954**, 5, (11), 386-390.
12. Wood, C. *Reports on Progress in Physics* **1988**, 51, (4), 459-539.
13. Gelbstein, Y.; Dashevsky, Z.; Dariel, M. P. *Physica B: Condensed Matter* **2005**, 363, (1-4), 196-205.
14. Ohta, H. *Materials Today* **2007**, 10, (10), 44-49.
15. Terasaki, I.; Sasago, Y.; Uchinokura, K. *Physical Review B* **1997**, 56, (20), 12685-12687.
16. Shikano, M.; Funahashi, R. *Applied Physics Letters* **2003**, 82, (12), 1851-1853.
17. Okuda, T.; Nakanishi, K.; Miyasaka, S.; Tokura, Y. *Physical Review B* **2001**, 63, (11), 113104.
18. Ohta, S.; Nomura, T.; Ohta, H.; Koumoto, K. *Journal of Applied Physics* **2005**, 97, (3), 034106.
19. Wunderlich, W.; Ohta, S.; Ohta, H.; Koumoto, K. *ICT: 2005 24th International Conference on Thermoelectrics* **2005**, 237-240.

20. Fan, X. X.; Wang, Y.; Chen, X. Y.; Gao, L.; Luo, W. J.; Yuan, Y. P.; Li, Z. S.; Yu, T.; Zhu, J. H.; Zou, Z. G. *Chemistry of Materials* **2010**, 22, (4), 1276-1278.
21. Ohta, S.; Nomura, T.; Ohta, H.; Hirano, M.; Hosono, H.; Koumoto, K. *Applied Physics Letters* **2005**, 87, (9), 092108.
22. Ahrens, M.; Merkle, R.; Rahmati, B.; Maier, J. *Physica B: Condensed Matter* **2007**, 393, (1-2), 239-248.
23. Durán, A.; Morales, F.; Fuentes, L.; Siqueiros, J. M. *Journal of Physics: Condensed Matter* **2008**, 20, (8), 085219.
24. Hofmeister, A. M. *Journal of Applied Physics* **2010**, 107, (10), 103532.

Chapter 6

Experimental Part

6.1 Materials

Ammonium sulphide solution (20 %), aqueous ammonia (25 wt%), copper(II) acetate monohydrate, copper(II) nitrate trihydrate 99.5%, ethanol, strontium carbonate, niobium(V) chloride, and vanadium(III)-chloride was purchased from Merck, cetyl trimethylammonium bromide, gallium(III) nitrate hydrate, glucose, titanium(IV) tetrabutoxide (97 %), N-[3-trimethoxysilylpropyl]ethylenediamine, poly(ethylene glycol)-block-poly(propylene glycol)-block-poly(ethylene glycol) (P123), acetic acid ($\geq 99\%$), cobalt(II) chloride hexahydrate from Aldrich, tetraethyl orthosilicate, chromium(III) nitrate nonahydrate from Fluka, aqueous ammonia (28-30 wt%) was purchased from Baker, anhydrous ammonia gas (99.98 %) used for the nitridation was purchased from Messer Austria GmbH.

6.2 Instrumentation

Energy dispersive X-ray (EDX) spectroscopy was performed on a JEOL 5410 connected to an EDX detector RÖNTEC. The spectra were analysed with the Edax Genesis software. Before measurement the samples were coated with gold.

Nitrogen sorption measurements at 77K were carried out on a Micromeritics ASAP 2020 and an ASAP 2010 instrument. The samples were degassed under vacuum at 50 °C for at least 5 h prior to measurements. The surface area was calculated according to Brunauer, Emmett and Teller (BET) and t-plot method, and the pore size distribution according to Barrett, Joyner and Halenda (BJH) applied on adsorption and desorption branches of the isotherm.

Scanning electron microscopy (SEM) was performed on a JEOL-6400 instrument using a tungsten filament.

Transmission electron microscopy (TEM), scanning transmission electron microscopy (STEM) and energy dispersive absorption X-ray (EDAX) images were obtained using a

TECNAI F20-S-TWIN apparatus with field emission source operating at 200 kV (USTEM, Vienna University of Technology). The powders were deposited on a carbon grid for TEM analysis.

Thermogravimetric analysis (TGA) was performed on a Netzsch Iris TG 209 C in an alumina crucible with a heating rate of 10 °C/min under synthetic air.

Ultraviolet-visible (UV-Vis) spectroscopy measurements were carried out on a PerkinElmer Lambda 35 UV-Vis spectrophotometer.

X-ray diffraction (XRD) measurements were performed on a Philipps XPert diffractometer using the Cu-K α radiation ($\lambda = 1.542 \text{ \AA}$), equipped with an XCelerator multi-channel detector, Bragg Brentano geometry, silicon single crystal sample holder.

6.3 Experimental

6.3.1 Preparation of metal nitride@SiO₂ and CuS@SiO₂ nanocomposites by sol-gel processing starting from tethered metal complexes

6.3.1.1 Preparation of Cu₃N@SiO₂

To a solution of Cu(OAc)₂·H₂O in ethanol (10 mL of ethanol per 0.1 mmol of Cu precursor), two equivalents of AEAPTS were added. This resulted in immediate colour change from green to violet blue. The mixture was stirred at room temperature for about 15 min. Twelve equivalents of TEOS were then added to this solution, followed by addition of an amount of 0.2 N aqueous ammonia that corresponded to a 7.5-fold excess of water relative to all alkoxy groups from TEOS and AEAPTS. The resulting homogeneous mixture was heated to 70 °C for 72 h in a closed vessel. Removal of the solvent from the obtained gels under reduced pressure gave a blue-coloured gel.

The dry gel was calcined in air at 800 °C for 1 h, with a heating rate of 5 °C/min. This resulted in a black solid (CuO@SiO₂). Nitridation of CuO@SiO₂ at 300 °C for 8 h in a horizontal quartz tube furnace under ammonia atmosphere gave brown Cu₃N@SiO₂. The ammonia flow was maintained at 5 l/h. The sample was taken from the furnace after cooling to room temperature under ammonia atmosphere.

6.3.1.2 Preparation of GaN@SiO₂

A molar ratio of Ga(NO₃)₃·H₂O / AEAPTS / TEOS of 1:3:10 was employed. The procedure for the preparation of the dry gel was similar as described for Cu₃N@SiO₂. The white coloured dry gel was calcined in air at 800 °C for 2 h, with a heating rate of 5 °C/min. This resulted in a white solid (Ga/O@SiO₂). Nitridation was performed on Ga/O@SiO₂ at 900 °C for 3 h using ammonia gas with a flow rate of 5 l/h. A yellowish white material was obtained after nitridation (GaN@SiO₂).

6.3.1.3 Preparation of CrN@SiO₂

A molar ratio of Cr(NO₃)₃·9H₂O / AEAPTS / TEOS of 1:3:5 was employed. The addition of AEAPTS to an ethanolic solution of Cr(NO₃)₃·9H₂O resulted in the immediate colour change from dark turquoise to cadet blue. The procedure for the preparation of the dry gel was similar

as described for $\text{Cu}_3\text{N@SiO}_2$. The light grey coloured dry gel was calcined in air at 400 and 500 °C for 2 h respectively, with a heating rate of 5 °C/min. This resulted in a yellowish green solid ($\text{Cr}_2\text{O}_3\text{@SiO}_2$). Nitridation was performed at 800 °C for 3 h using ammonia gas with a flow rate of 5 l/h. A black material was obtained after nitridation (CrN@SiO_2).

6.3.1.4 Preparation of VN@SiO_2

A molar ratio of VCl_3 / AEAPTS / TEOS of 1:3:2 was employed. Addition of AEAPTS to an ethanolic solution of VCl_3 resulted in immediate colour change from light green to dark brown. The procedure for the preparation of the dry gel was similar as described for $\text{Cu}_3\text{N@SiO}_2$. The off white coloured dry gel was calcined in air at 700 °C for 3 h, with a heating rate of 5 °C/min. This resulted in a yellow solid ($\text{V}_2\text{O}_3\text{@SiO}_2$). Nitridation was performed at 900 °C for 6 h using ammonia gas with a flow rate of 5 l/h. A black material was obtained after nitridation (VN@SiO_2).

6.3.1.5 Preparation of $\text{Co}_2\text{N@SiO}_2$

A molar ratio of $\text{CoCl}_2 \cdot 6\text{H}_2\text{O}$ / AEAPTS / TEOS of 1:3:2 was employed. Addition of AEAPTS to an ethanolic solution of $\text{CoCl}_2 \cdot 6\text{H}_2\text{O}$ resulted in immediate colour change from blue to dark red. The procedure for the preparation of the dry gel was similar as described for $\text{Cu}_3\text{N@SiO}_2$. The dark sea coloured dry gel was calcined in air at 700 °C for 3 h, with a heating rate of 5 °C/min. This resulted in a blue solid ($\text{Co}_3\text{O}_4\text{@SiO}_2$). Nitridation was performed at 325 °C for 15 h using ammonia gas with a flow rate of 5 l/h. A bluish black material was obtained after nitridation ($\text{Co}_2\text{N@SiO}_2$).

6.3.1.6 Preparation of CuS@SiO_2

The preparation of CuO@SiO_2 is described in section 6.3.1.1. 50 mg of CuO@SiO_2 was dispersed in 5 mL of H_2O with stirring. 0.2 mL of aqueous $(\text{NH}_4)_2\text{S}$ was added drop wise to the above dispersion giving green colour to the solution. The suspension was stirred for 6 h. The green coloured compound was obtained by centrifugation and washing with deionised water three times. Drying the obtained compound at 60 °C in an oven gave CuS@SiO_2 as a green powder.

6.3.2 Synthesis of functional nanoparticles (CuO and Cu₃N) within hollow mesoporous silica capsules – Route 1

6.3.2.1 Preparation of carbon spheres

Carbon spheres were synthesized according to the procedure reported by Sun et. al¹. Glucose (8 g) was dissolved in 70 mL of distilled water with stirring until it forms a clear solution. The solution was then placed in an 80 mL Teflon-sealed autoclave and maintained at 180 °C in a preheated electric oven for 10 h. The obtained product was isolated by centrifugation followed by washing several times, using water and ethanol, and finally dried at 80°C for 8 h.

6.3.2.2 Preparation of Cu²⁺ ion-adsorbed carbon spheres (Cu²⁺/carbon sphere)

The 200 mg of carbon spheres were dispersed into a Cu(NO₃)₂ · 3H₂O solution (0.5 M, 50 mL) with ultra-sonication for 60 min to allow adsorption of the copper ions on the surface of the carbon spheres. The resulting suspension was stirred gently for 15 h before being subjected to washing and centrifugation with distilled water several times. The sample was dried at 80°C for 6 h.

6.3.2.3 Preparation of CuO@H-mSiO₂ sphere

175 mg of the Cu²⁺/carbon spheres were dispersed in 25 mL of water with ultrasonication for 30 min. 0.28 g of CTAB was dissolved in a mixer of 29 mL of water and 22.2 mL of ethanol. Both solutions were mixed with stirring, followed by addition of 0.9 mL of aq. ammonia (25%). The mixture was stirred for 30 min, and finally 0.5 mL of TEOS was added dropwise. The reaction mixture was stirred for 60 h at room temperature. The weight ratio of Cu²⁺/carbon spheres to TEOS was kept at 2.7. The molar ratio of TEOS/CTAB/NH₃/EtOH/H₂O was 1/0.34/5.3/168/1320. Cu²⁺/carbon sphere/silica was obtained by centrifugation followed by washing and dispersion in water three times, and finally dried at 80°C. The Cu²⁺/carbon sphere/silica was heated at 550 °C for 6 h with a heating rate of 3 °C/min to give CuO@H-mSiO₂ spheres.

6.3.2.4 Preparation of Cu₃N@H-mSiO₂ spheres

The CuO@H-mSiO₂ spheres were nitrated at 300 °C for 10 h in a horizontal tube furnace, with a heating rate of 5°C/min under ammonia atmosphere with the flow rate of 10 l/h. The furnace was allowed to cool under ammonia atmosphere. The brown product obtained was denoted as Cu₃N@H-mSiO₂ sphere.

6.3.3 Synthesis of functional nanoparticles (CuO and Cu₃N) within hollow mesoporous silica capsules – Route 2

6.3.3.1 Synthesis of colloidal carbon spheres

see section 6.3.2.1

6.3.3.2 Synthesis of hollow mesoporous silica spheres (H-mSiO₂ spheres)

240 mg of the carbon spheres were dispersed in 40 mL of water with ultrasonication for 30 min. 0.43 g of CTAB was dissolved in a mixer of 42 mL of water and 34 mL of ethanol. Both solutions were mixed with stirring followed by addition of 1.4 mL of aq. ammonia (25%). The mixture was stirred for 30 min, and finally 0.76 mL of TEOS was added dropwise. The reaction stirred at 60 h at room temperature. The weight ratio of carbon spheres to TEOS was kept at 3. The molar ratio of TEOS/CTAB/NH₃/EtOH/H₂O was 1/0.34/5.3/168/1320. The carbon-silica hybrid spheres were obtained by centrifugation followed by washing and dispersion in water three times, and finally dried at 80°C. The oven-dried sample was heated at 650 °C for 3 h at the rate of 2°C/min to obtain H-mSiO₂ spheres.

6.3.3.3 Synthesis of CuO@H-mSiO₂-NC

100 mg of H-mSiO₂ spheres were added to 1M copper nitrate solution in ethanol. The suspension was placed under vacuum with ultrasonication. After 15 min the vacuum pump was turned off and air was allowed to fill in to the system to reach atmospheric conditions. The ultrasonic treatment was continued for 10 min. The copper nitrate solution was removed by centrifugation and the solid obtained was dried at 40 °C in air. The dry solid was washed with absolute ethanol three times thoroughly and dried at 50 °C in air. Finally the powder was

calcined at 400 °C for 1 h at the rate of 2 °C/min. The black solid obtained was denoted as CuO@H-mSiO₂-NC.

6.3.3.4 Synthesis of Cu₃N@H-mSiO₂-NC

The CuO@H-mSiO₂-NC was nitrated at 300 °C for 10 h at a heating rate of 5°C/min under ammonia atmosphere with the flow rate of 15 l/h. The furnace was allowed to cool under ammonia atmosphere. The obtained brown product was denoted as Cu₃N@H-mSiO₂-NC.

6.3.4 Synthesis of functional nanoparticles (CuO and Cu₃N) within hollow mesoporous silica capsules – Route 3

6.3.4.1 Preparation of carbon spheres

see section 6.3.2.1

6.3.4.2 Preparation of Cu²⁺ adsorbed carbon spheres (Cu²⁺/carbon sphere)

An aqueous ammonia solution was slowly added to 10 mL of a 0.5 M copper nitrate solution until the initially formed precipitate disappeared again. A dark blue complex [Cu(NH₃)₄(H₂O)₂]²⁺ was formed. 100 mg of carbon spheres were dispersed into this solution with ultra-sonication for 30 min. The resulting suspension was stirred gently for 15 h before being subjected to washing and centrifugation with distilled water several times. The sample was dried at 80 °C for 6 h.

6.3.4.3 Preparation of CuO@H-mSiO₂ sphere

100 mg of Cu²⁺/carbon sphere were dispersed in 10 mL of water with ultrasonication for 30 min. 0.12 g of CTAB was dissolved in a mixture of 13 mL of water and 10 mL of ethanol. Both solutions were mixed with stirring followed by addition of 0.38 mL of aq. ammonia (25%). The mixture was stirred for 30 min, and finally 0.21 mL TEOS was added drop wise. The reaction was stirred for 60 h at room temperature. The weight ratio of Cu²⁺/carbon sphere to TEOS was kept at 2. The molar ratio of TEOS/CTAB/NH₃/EtOH/H₂O was 1/0.34/5.3/168/1320. Cu²⁺/carbon sphere-silica hybrid spheres were obtained by

centrifugation followed by washing and dispersion in water three times and finally drying at 80°C. The oven-dried sample was heated at 500 °C for 2 h with a heating rate of 2°C/min to yield a black product, denoted as CuO@H-mSiO₂ sphere.

6.3.4.4 Synthesis of Cu₃N@H-mSiO₂ sphere

The CuO@H-mSiO₂ spheres were nitridated at 350 °C for 2 h with a heating rate of 5°C/min under ammonia atmosphere with the flow rate of 15 l/h. The furnace was allowed to cool under ammonia atmosphere. The obtained brown product was denoted as Cu₃N@H-mSiO₂ sphere.

6.3.5 Synthesis of CuO@SiO₂ and Cu₃N@SiO₂ hierarchical hollow spheres (HHSs) via CuSiO₃ HHSs

6.3.5.1 Synthesis of SiO₂ spheres

SiO₂ spheres were synthesized according to the literature method². A solution of 81 mL of ethanol and 24.5 mL of NH₃ (28-30%) was stirred with 750 rpm at 30 °C in a 500 mL round bottom flask sealed with a septum. To this solution 4.2 mL of TEOS was injected rapidly, and the reaction was stirred for 60 min. A colloidal suspension of monodisperse silica spheres was obtained, which was centrifuged and washed with ethanol and water several times. Finally the white solid was dried at 60 °C for 6 h.

6.3.5.2 Synthesis of CuSiO₃ HHSs

CuSiO₃ HHSs were synthesized according to the literature method³. In a typical experiment, 0.130 g of SiO₂ spheres were dispersed in 30 mL of distilled water using ultrasonication. Separately, Cu(NO₃)₂·3H₂O (0.7 mmol) was dissolved in 30 mL of distilled water followed by addition of 3 mL of aq. ammonia (30%). The homogeneous solution obtained after mixing the two solutions was transferred into 80 mL Teflon lined stainless steel autoclave. The autoclave was kept at 140 °C for 24 h in a preheated electric oven. The autoclave was removed from the oven and allowed to cool to room temperature. A blue product was isolated by centrifugation and washing with water several times, followed by drying at 70 °C for 6 h.

6.3.5.3 Synthesis of CuO@SiO₂ HHSs

A portion of CuSiO₃ HHSs was placed in a ceramic boat. The boat was kept in a horizontal tube furnace at 700 °C for 30 min in air with a heating rate of 3 °C/min. Black coloured CuO@SiO₂ HHSs was obtained.

6.3.5.4 Synthesis of Cu₃N@SiO₂ HHSs

A portion of CuSiO₃ HHSs was placed in a ceramic boat. The boat was kept in a horizontal tube furnace at 350 °C for 1 h in ammonia atmosphere with a heating rate of 3 °C/min. The flow rate of ammonia gas was maintained at 10 l/h. Brown coloured Cu₃N@SiO₂ HHSs was obtained.

6.3.6 Synthesis of SrTiO₃, SrTiO₃/SrCO₃ composites and SrTi_{0.8}Nb_{0.2}O₃

6.3.6.1 Synthesis of SrTiO₃ and SrTiO₃/SrCO₃ composites

All composites were synthesized by modification of reported procedure⁴. In a set of four experiments, titanium tetrabutoxide (0.02, 0.016, 0.013, 0.01 mol) was dissolved in 15 ml of ethanol. SrCO₃ (0.02 mol) was dissolved in a mixture of 50 ml acetic acid and 25 ml of H₂O, the ratio of Sr/Ti being 1, 1.6, 1.3, 2 respectively. The two solutions were mixed, and then P123 (3 g) was added with stirring. After stirring for an hour, the obtained sol was deposited on a large glass sheet (25 x 25 cm) and dried at room temperature. The films were scraped off by using a razor blade and calcined at 750 °C for 6 h in air with a heating rate of 5 °C/min. The products obtained were denoted as (SrTiO₃)_{1-x}(SrCO₃)_x (x = 0, 0.20, 0.32, 0.44).

6.3.6.2 Synthesis of SrTi_{0.8}Nb_{0.2}O₃

Titanium tetrabutoxide (0.016 mol) and NbCl₅ (0.004 mol) was dissolved in 20 ml of ethanol. SrCO₃ (0.02 mol) was dissolved in a mixture of 50 ml acetic acid and 25 ml of H₂O. The two solutions were mixed, and then P123 (3 g) was added with stirring. After stirring for an hour, the obtained sol was deposited on a large glass sheet (25 x 25 cm) and dried at room temperature. The films were scraped off by using a razor blade and calcined at 750 °C for 6 h in air with the heating rate of 5 °C/min. The product obtained was denoted as SrTi_{0.8}Nb_{0.2}O₃.

6.4 References

1. Sun, X. M.; Li, Y. D. *Angewandte Chemie-International Edition* **2004**, 43, (29), 3827-3831.
2. Stober, W.; Fink, A.; Bohn, E. *Journal of Colloid and Interface Science* **1968**, 26, (1), 62-69.
3. Wang, Y. Q.; Wang, G. Z.; Wang, H. Q.; Cai, W. P.; Zhang, L. D. *Chemical Communications* **2008**, (48), 6555-6557.
4. Fan, X. X.; Wang, Y.; Chen, X. Y.; Gao, L.; Luo, W. J.; Yuan, Y. P.; Li, Z. S.; Yu, T.; Zhu, J. H.; Zou, Z. G. *Chemistry of Materials* **2010**, 22, (4), 1276-1278.

Chapter 7

Summary and Outlook

During the last several years, interest in the study of nanostructured materials has been increasing at an accelerating rate. Nanomaterials exhibit many unique and interesting physical and chemical properties compared to bulk materials leading to a number of potential technological applications.

There are several ways to synthesize nanocomposites, where nanoparticles are embedded in an inert matrix. The primary goal of this work was to synthesize various metal nitride nanoparticles in/on silica composites.

In the first part of the work, the focus was on the synthesis of metal nitride nanoparticles, well-dispersed in a silica matrix by sol-gel processing of tethered metal complexes (Fig. 7.1).

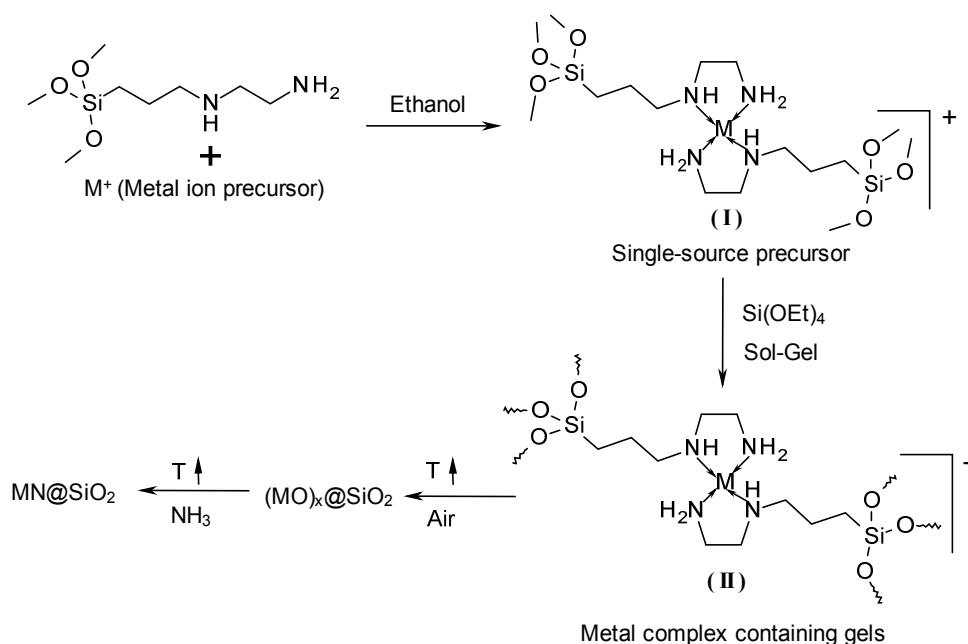


Fig. 7.1 Synthesis of the MN@SiO₂ nanocomposites.

The use of single-source precursors of the type (RO)₃Si(CH₂)₃-X-M, where M is a metal ion and X = -NH-CH₂-CH₂-NH₂ is a coordinating group, tethering the Si(RO)₃ group and M a metal ion, offers distinct advantages for the preparation of metal nitride@SiO₂ nanocomposites with a controllable dispersion of the metal nitride nanoparticles. This approach is based on the molecular dispersion of metal ions during sol-gel processing by

means of an organic tether. Controlled heat treatment of the gels containing tethered metal complexes results in the degradation of the organic moieties and simultaneous formation of metal oxide nanoparticles in a silica matrix. Subsequent reaction of the metal oxide@SiO₂ nanocomposite with gaseous ammonia at elevated temperature allowed formation of highly dispersed metal nitride nanoparticles in a SiO₂ matrix. Finely distributed nanoparticles of copper nitride in a silica matrix (Cu₃N@SiO₂ nanocomposite) were synthesized by this method (Fig. 7.2). Additionally, nanocomposites of GaN@SiO₂, CrN@SiO₂, Co₂N@SiO₂ and VN@SiO₂ were also synthesized by this method. Furthermore, a CuS@SiO₂ nanocomposite was synthesized by reaction of a CuO@SiO₂ nanocomposite with aqueous ammonium sulphide at room temperature. Thus, the sol-gel processing of tethered metal complexes has been successfully extended for the synthesis of highly dispersed nanoparticles of metal nitrides in silica matrices and copper sulphide nanoparticles in a silica matrix.

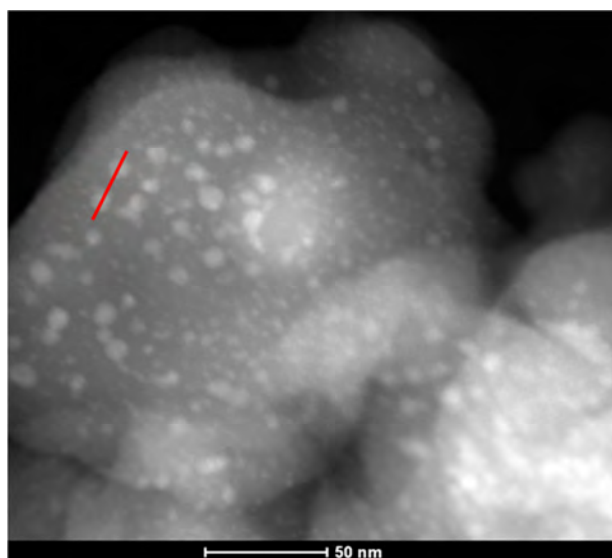


Fig. 7.2 STEM image from Cu₃N@SiO₂ nanocomposite.

In the second part, three different routes based on a carbon template strategy were employed for the fabrication of copper nitride nanoparticles inside a hollow mesoporous silica sphere.

In first route, Cu₃N nanoparticles in hollow mesoporous silica spheres were prepared by using copper ion-adsorbed carbon spheres as template. The carbon spheres synthesized by hydrothermal carbonisation of glucose contain surface functional groups such as -OH, -CHO, -COOH which are able to bind to metal ions. The dispersion of the carbon spheres in solutions of copper nitrate led the adsorption of the copper ions onto the surface layer.

Copper ion-adsorbed carbon spheres were coated with silica by sol-gel processing using TEOS and cetyl trimethylammonium bromide (CTAB). Subsequent calcination removed carbon and CTAB, giving copper oxide nanoparticles within the hollow mesoporous silica

spheres. Subsequent nitridation converted the CuO particles in Cu₃N nanoparticles (Fig. 7.3). However, the loading of Cu₃N nanoparticles per silica sphere is limited by this route.

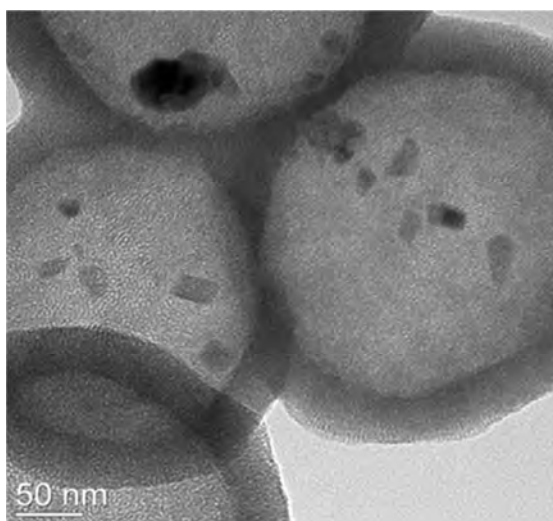


Fig. 7.3 TEM image of Cu₃N nanoparticles in hollow mesoporous silica spheres.

In the second route, a pre-shell and post-core strategy was applied for the synthesis of the Cu₃N nanoparticles. First, hollow mesoporous silica spheres (H-mSiO₂) were synthesized via the carbon sphere templating method. The copper ions were loaded into the hollow silica spheres by the vacuum nanocasting route followed by calcination and nitridation. The Cu₃N nanoparticles were found inside as well as outside of the pre-formed H-mSiO₂ spheres and some H-mSiO₂ spheres did not contain any Cu₃N particles (Fig. 7.4). Thus the vacuum nanocasting route was only partially successful to obtain Cu₃N nanoparticles exclusively inside the hollow mesoporous silica spheres.

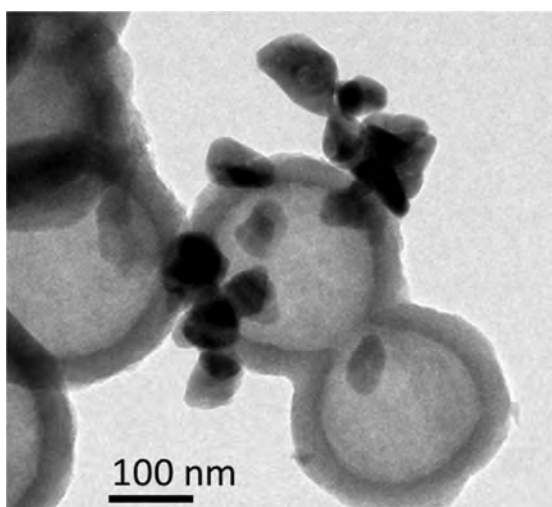


Fig. 7.4 STEM image of Cu₃N@H-mSiO₂ nanocomposite.

In route 3, CuO nanoparticles in hollow mesoporous silica spheres were prepared by using $[\text{Cu}(\text{NH}_3)_4(\text{H}_2\text{O})_2]^{2+}$ ion-adsorbed carbon spheres as template. The $[\text{Cu}(\text{NH}_3)_4(\text{H}_2\text{O})_2]^{2+}$ ions adsorbed carbon spheres were coated with silica by sol-gel processing using TEOS and CTAB. A subsequent calcination step gave copper oxide nanoparticles exclusively within the hollow mesoporous silica spheres (Fig. 7.5 a). The CuO nanoparticles were transformed into Cu_3N nanoparticles by nitridation without affecting the silica shell structure (Fig. 7.5 b). Compared to route 1, the loading of Cu_3N nanoparticles inside the hollow mesoporous silica spheres is higher. This might be due to stronger electrostatic and coordination interactions between $[\text{Cu}(\text{NH}_3)_4(\text{H}_2\text{O})_2]^{2+}$ ions with surface functional groups on the carbon spheres.

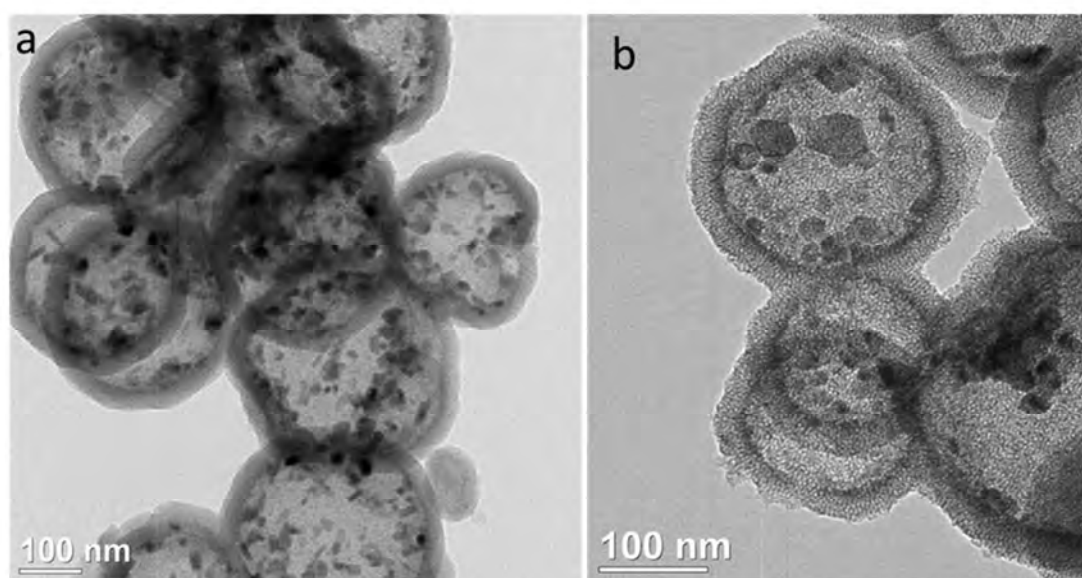


Fig. 7.5 TEM image of (a) CuO and (b) Cu_3N nanoparticles in hollow mesoporous silica spheres.

In the third part of this work, $\text{CuO}@/\text{SiO}_2$ and $\text{Cu}_3\text{N}@/\text{SiO}_2$ HHSs were synthesized from a CuSiO_3 HHSs precursor. CuO nanoparticles distributed on SiO_2 HHSs were obtained by heat treatment of CuSiO_3 HHSs at 700 °C in air (Fig. 7.6 a). Moreover, CuSiO_3 HHSs were converted into Cu_3N nanoparticles embedded on SiO_2 HHSs by direct nitridation reaction at 350 °C (Fig. 7.6 b). During the nitridation reaction copper species migrated on the surface creating large agglomerated Cu_3N nanoparticles on the hollow silica shell. The conversion of CuSiO_3 HHSs to $\text{CuO}@/\text{SiO}_2$ and $\text{Cu}_3\text{N}@/\text{SiO}_2$ HHSs is a new observation. The results indicates that direct ammonia nitridation and thermal disintegration of CuSiO_3 HHSs is a feasible reaction and could also be applied to synthesize other metal oxide@silica and metal nitride@silica composite materials.

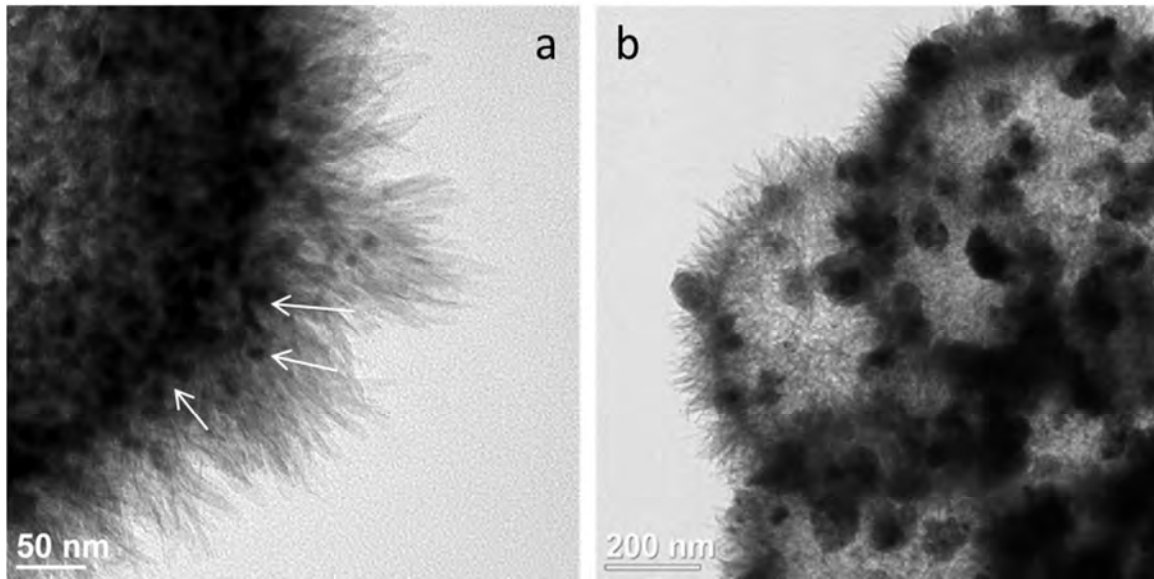


Fig. 7.6 TEM image of (a) CuO@SiO₂ HHHs and (b) Cu₃N@SiO₂ HHSs.

In the last part of this work, (SrTiO₃)_{1-x}(SrCO₃)_x ($x = 0, 0.22, 0.31, 0.45$) composites were synthesized and investigated by thermal diffusivity and thermal conductivity measurements. Crystalline SrTiO₃ is a promising thermoelectric material at higher temperatures. In order to improve the thermoelectric efficiency of SrTiO₃, reduction of thermal conductivity without affecting the electrical conductivity is a crucial factor. The substitution with SrCO₃ was done to lower the thermal diffusivity. The thermal conductivities are significantly reduced for all composites in comparison to single crystalline SrTiO₃ (Fig. 7.8).

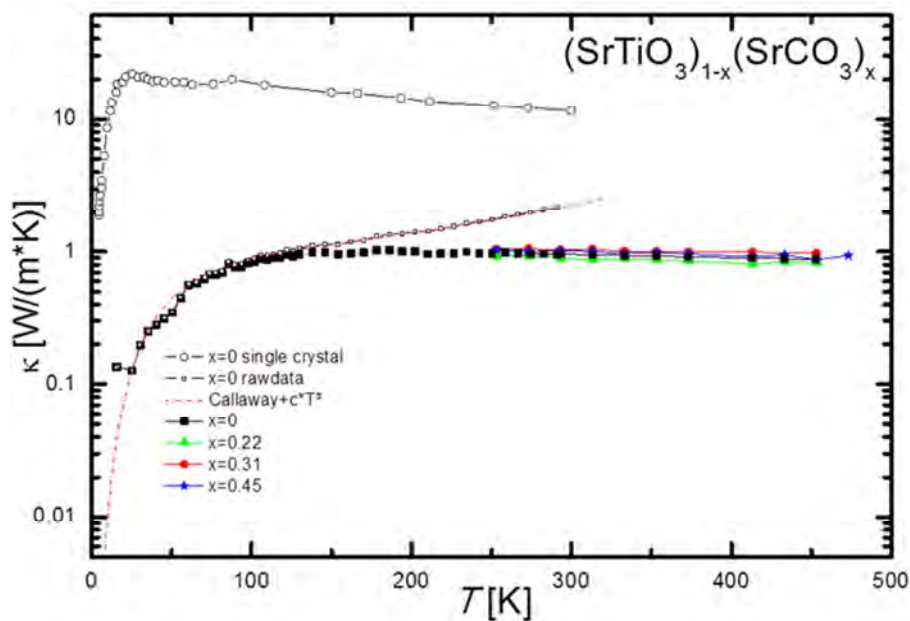


Fig. 7.8 Thermal conductivities of (SrTiO₃)_{1-x}(SrCO₃)_x ($x = 0, 0.22, 0.31, 0.45$) composites compared with literature data for single-crystalline SrTiO₃.

The reason behind reduction in thermal conductivity might be due to poor compaction of the composites after hot pressing, since no systematic dependence on the SrCO₃ content was observed. More insights are needed to understand structure property relationship in these composite materials.

Curriculum Vitae

Name Ms. Rupali Ganpat Deshmukh
Address Dirmhirngasse 27/614, 1230 Wien
Date of Birth 12th December 1983
Nationality Indian

Education

03/2009-present PhD studies in Materials Chemistry at Vienna University of Technology, Vienna, Austria
Topic: “Metal Nitride and Metal Oxide Nanocomposite Materials”
Supervisor: Prof. Dr. Ulrich Schubert

06/2004-04/2006 Master of Science in Inorganic Chemistry at University of Pune, Pune, India
Topic: “Aromatization of Hantzsch 1, 4-Dihydropyridines by Co (II) based Catalysts”
Supervisor: Prof. Dr. Satish Pardeshi

06/2001-05/2004 Bachelor of Science in Chemistry at University of Pune, India

Work Experience

03/2009-present Project assistant at Institute of Materials Chemistry, Vienna University of Technology, Vienna

01/2007-11/2008 Project assistant at National Chemical Laboratory, Pune, India

Publications

1. Metal nitride@SiO₂ nanocomposites by sol-gel processing starting from tethered metal complexes, R. Deshmukh and U. Schubert, Journal of Materials Chemistry, **2011**, 21(46), 18534-18536.
2. Microwave-assisted synthesis and humidity sensing of nanostructured α -Fe₂O₃, R. G. Deshmukh, S. S. Badadhe and I. S. Mulla, Materials Research Bulletin, **2009**, 44(5), 1179-1182.

3. Gas sensing properties of nanosized zinc-ferrite synthesized by Molten- Salt method, S. L. Darshane, R. G. Deshmukh, S. S. Suryavanshi and I. S. Mulla, J. Am. Ceram. Soc., **2008**, 91(8), 2724-2726.
4. Facile synthesis and gas sensing properties of nanotriangular tin oxide, R. G. Deshmukh, S. S. Badadhe, M. V. Vaishampayan and I. S. Mulla, Materials Letters, **2008**, 62(28), 4328-4331.
5. Fe-doped SnO₂ nanomaterial: A low temperature hydrogen sulfide gas sensor, M. V. Vaishampayan, R. G. Deshmukh, P. S. Walke and I. S. Mulla, Materials Chemistry and Physics, **2008**, 109(2-3), 230-234.
6. Preparation of ferroelectric CaBi₄Ti₄O₁₅ powders from novel hydroxide precursors, Rupali G. Deshmukh, Mukta V. Vaishampayan, Darshane S. L., I. S. Mulla, A. B. Gaikwad, N. K. Rao and V. Ravi, Materials Letters, **2008**, 62(12-13), 1751-1753.
7. Influence of Pd doping on morphology and LPG response of SnO₂, M. V. Vaishampayan, R. G. Deshmukh and I. S. Mulla, Sensors and Actuators B: Chemical, **2008**, 131(2), 665-672.